Siam Photon

SYNCHROTRON
THAILAND
CENTRAL LAB

SLRI
Annual Review
2016 - 2017

Message from chairman

Synchrotron Light Research Institute (Public Organization) or SLRI was established in 2008 as Thailand's central laboratory for delivering 3 main missions

- to develop a country large scale facility as a scientific infrastructure, a synchrotron light source,
- to provide service researchers from academic and industrial sectors not only for supporting frontier research, but also for developing new and high quality products and
- to bring knowledge and advanced technology to community.

SLRI continuosly plays an important role in capacity building of the region through ASEAN workshops and trainings. As a result of over 2,500 experiments conducted at SLRI, more than 600 scientific journals were published within the last decade of operation. In becoming the regional hub of research for the next decade, SLRI sets the new strategic position to achive the new generation of synchrotron light source. With cutting-edge technology, the new light source will be a driving tool to expand research of academic and industrial sectors.

Assoc. Prof. Dr.Soranit Siltharm, M.D.

Chairman of the SLRI Executive Board

Message from director

Synchrotron facility in Thailand has been in full service for 10 years, and the institute was established as a public organization in 2008. Our institute operates a 2nd-generation synchrotron @1.2 GeV for 24 hours daily with 3 shifts, and 9 months a year. We offer services to universities, research institutes and industries. So far, annual reports have been published (in thai) for the government. The materials inside are mainly outputs, outcomes and economic impacts made by the institute. Materials concerning technical details of machine, beamlines, and research activities are not much covered due to limited space.

It is the very first time that our institute launches an annual review (in english) covering research activities, machine and beamlines development. The publication is aimed for keeping the international community informed about our facility, and activities performed by users. Also as an invitation to international users to consider collaborating with us. We welcomed more than 400 users in 2016; several were from Europe, the US, and Asean nations. This issue contains 14 articles reporting our facility status, and 10 selective research articles. I wish that our users, the prospective ones, and scientists at large would enjoy reading these articles.

Finally, I am grateful to our contributors of all those articles, and our users who have critical roles on supporting us. Special thanks are due to the members of our Executive Board, and the International Advisory Committee for their great supports of all dimensions. I also wish to thank my colleagues who have taken a good care of our users and facility and to the editorial team who made the review issue possible.

Sarawut Sujitjorn

SLRI director

Message from editor

On the special occasion of the 10th Anniversary of SLRI in 2018, we proudly debut the SLRI Annual Review 2016-17. This is our first journal written in English with provident selection of articles to gain international recognition and engage with user community. The selected articles allocate into two sections. The first section, Facilities: Current Status, presents the progress and status of the beamlines and accelerator and their performances including development projects such as, prototype of a combined function magnet and linear accelerator for medical applications. The second section, Research Activities, is dedicated to research activities performed by SLRI users.

From 2018 onwards, the SLRI Annual Review will be published on annual basis. The editorial board would like to take this opportunity to thank the authors for their contribution in finalizing the output of this issue.

Happy Anniversary.

Editor
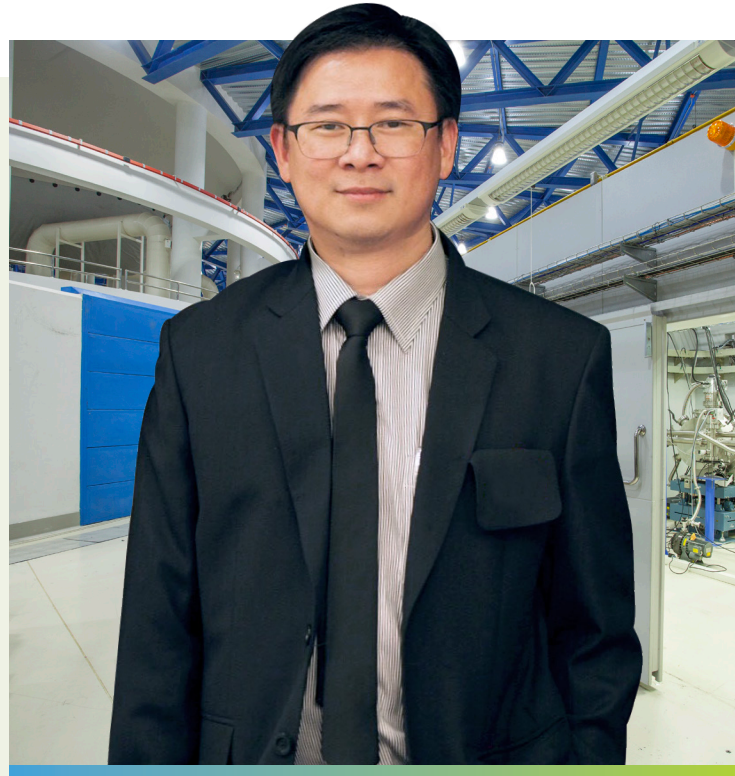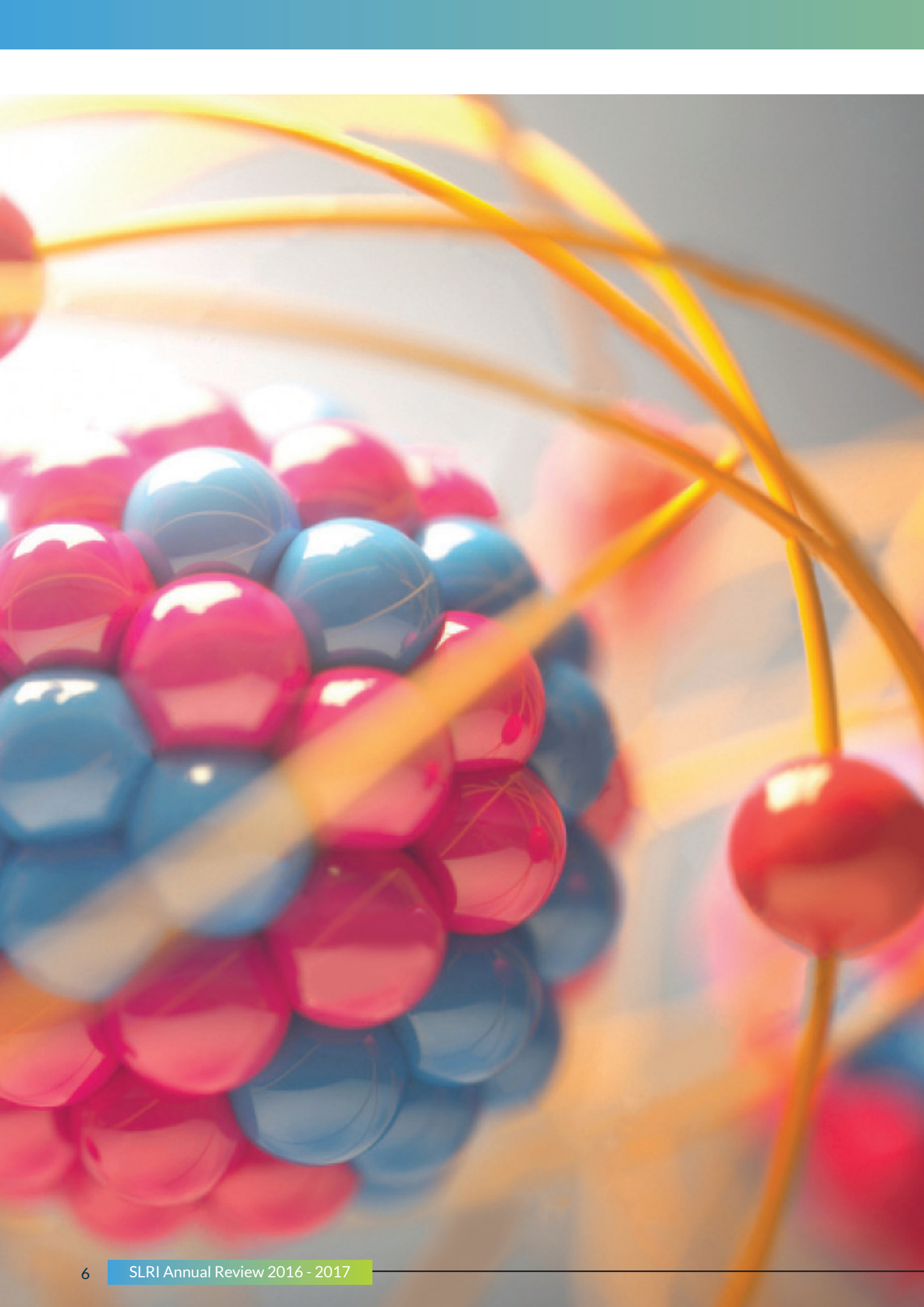
CONTENT

FACILITIES:
CURRENT STATUS

The Siam Photon Laboratory, a high brilliant light source in South-East Asia

S. Tancharakorn*

Synchrotron Light Research Institute (Public Organization), 111 University Avenue, Muang District,Nakhon Ratchasima 30000, Thailand

Abstract

Synchrotron radiation facility at the Siam Photon Laboratory (SPL), Thailand operated by the Synchrotron Light Research Institute (Public Organization) or SLRI has served science community since 2003 with one beamline available. In 2016, with 3 insertion devices installed, 10 beamlines and 12 end-stations are available to serve research community. These beamlines cover photon energy from 0.0124 eV to 20 keV with photon flux above 1012 photons/sec depending on energy. Details of beamlines are presented here.

Introduction

Synchrotron light source is known as the most intense light source for research community. It was discovered in 1947 at the General Electric, USA. Not until 1960s, the first generation of synchrotron radiation source was then constructed followed by the 2nd generation in 1980s, the 3rd generation in 1990s and the 4th generation in 2000s [1]. At present, there are more than 50 synchrotron radiation sources around the world. The difference between generation is an electron beam emittance corresponding to the brilliant of synchrotron radiation. The lower emittance, the higher brilliant radiation emitted from electron.

In South East Asia, there are two synchrotron facilities in operation, the Siam Photon Source (SPS) in Thailand and the Singaporean Synchrotron Light Source (SSLS). The SSLS is operated by the National University of Singapore while the SPS is a user facility opened for researchers in this region and around the world.

The SPS is a 1.2 GeV electron storage ring running in injection mode. It was modified from the 1 GeV storage ring donated from SORTEC corporation, Japan. It was successfully installed and commissioned in 2001. The first beamline was opened to public in 2003.

Siam Photon Source

The Siam Photon Source (SPS) at Nakhon Ratchasima, Thailand, consists of three main parts: a 40 MeV linear accelerator, a 1 GeV booster synchrotron and a 1.2 GeV electron storage ring. The electron storage ring utilizes a double bend achromat lattice (DBA) consisting of four periods with four straight sections for insertion devices. Each period has two bending magnets, four focusing quadrupole magnets and four defocusing quadrupole magnets. Therefore, at least eight beamlines can be accommodated. So far, an undulator with 60 periods (U60) of magnetic poles, a 2.2T multipole wiggler (MPW) with 5 periods of magnetic poles and a 6.5T superconducting wavelength shifter (WLS) have been installed in the storage ring. The spectrum of synchrotron radiation from bending magnet (BM) and 3 insertion devices is shown in Fig. 1 [2].
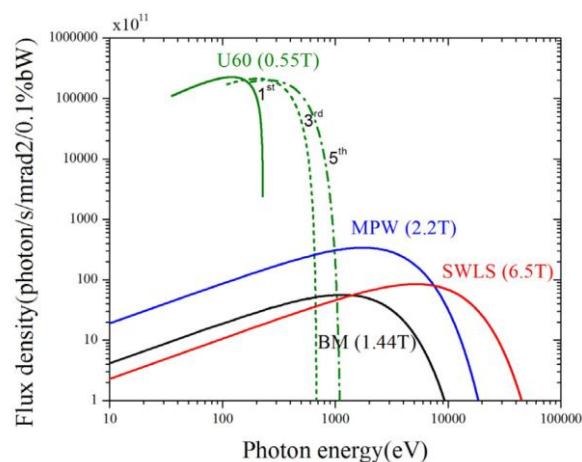
Figure 1: Spectrum of synchrotron radiation from various sources at SPS [2]

SLRI beamline facility

Synchrotron radiation from bending magnet at SPS as shown in Fig. 1 covers energy range from infrared to low energy X-rays (energy up to 12 keV). However, with three insertion devices; U60, MPW and WLS installed, the flux density at VUV range is increased by 10^4 with U60, while the MPW and WLS can increase synchrotron energy to 15 keV and 20 keV, respectively, with usable intensity.

In 2003, BL4: Photoemission Spectroscopy was opened for surface science community which later relocated to BL3.2Ua/b to utilise synchrotron radiation from an undulator. In 2006, BL8:X-ray Absorption Spectroscopy was opened. As the number of users increased as well as more demand from user community, the number of beamlines has been also increased, accordingly. In 2016, 10 beamlines with 12 end-stations are available to serve more than 300 projects annually from academia and industries.

Figure 2: Beamlines at Siam Photon Laboratory

Table 1: List of beamlines at SPL

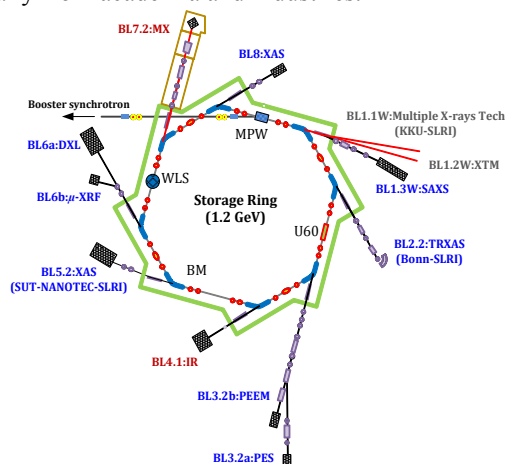| BL	Source	Energy range	Beamsize (HxV)	Available techniques
1.1W	MPW (2.2T)	4 – 18 keV	5 x 2.5 mm^2	• XAS/XRF (19 element HPGe detector) • WAXS • XRD (planning)
1.2W	MPW (2.2T)	White beam	10 x 4 mm^2	• X-ray imaging/tomography (resolution 1 μm)
1.3W	MPW (2.2T)	6 – 9 keV	2 x 1 mm^2	• SAXS/WAXS with tensile machine (max 500N), Temp control unit (15 – 200 °C) • Sample-detector distance (140 – 4500 mm)
2.2	BM	4 – 12 keV	1 x 2 mm^2	• Time Resolved-XAS
3.2Ua PES	Planar U60	40 – 1040 eV	0.1 x 0.1 mm^2 (XPS) 0.3 x 0.1mm^2 (ARPES)	• XPS/XAS • ARPES
3.2Ub PEEM	Planar U60	40 – 1040 eV	0.8 x 0.1 mm^2	• PEEM(FOV 2-75 μm up to 15 nm) • LEEM(FOV 25-100 μm up to 50 nm)
4.1	BM	0.496 – 0.0124 eV 2.5 – 100 μm	10 x 10 μm^2	• FT-IR spectroscopy & imaging with Transmission & reflection modes
5.2	BM	1.25 – 12.1 keV	10 x 1 mm^2	• XAS
6a DXL	BM	White beam	80 x 15 mm^2	• DXL
6b μ-XRF	BM	White beam (2 – 12 keV)	⌀30 μm	• Micro beam-XRF
7.2W	WLS (4T)*	8 – 20 keV	-	• MX with MarCCD 165 mm (*WLS will be operated at 6.5T)
8	BM	1.25 – 11 keV	13 x 2.5 mm^2	• XAS (13 element HPGe detector) • Electron-yield mode XAS

Fig. 2 shows the beamlines layout at SPL in 2016. There are 5 beamlines utilizing radiation from bending magnet, while 5 beamlines utilizing radiation from insertion devices [3].

Techniques available at SPL can be classified into 3 groups in term of energy range; infrared, VUV and X-rays as follows (see table 1):

• Infrared range: 0.496 – 0.0124 eV or 2.5 – 100 mm
• Beamline: BL4.1:IR microspectroscopy

• VUV range: 40 – 1040 eV
• Beamlines: BL3.2Ua/b: PES and PEEM

• X-ray range: 2 – 12 keV (white beam)
• Beamlines: BL1.2W:X-ray Tomography, BL6a/b: DXL/micro-XRF

*BL5.3:XPS is under construction
**BL1.1W:MXT consisting 2 end-stations: XAS (completed) and XRD (planned)

• X-ray range: 1.25 – 20 keV (monochromatic)
• Beamlines: BL1.1W: Multiple X-ray Techniques (MXT), BL1.3W:SAXS/WAXS, BL2.2:TRXAS, BL5.2:XAS (SUT-Nanotec-SLRI), BL5.3:XPS (SUT-Nanotec-SLRI)*, BL7.2W:MX and BL8:XAS

Current beamlines can also be divided into 5 different techniques; photoemission, absorption, scattering, imaging and fabrication as follows:

• **Photoemission**: BL3.2Ua/b: PES/PEEM, BL5.3:XPS (SUT-Nanotec-SLRI)
• **Absorption**: BL1.1W:MXT, BL2.2:TRXAS, BL4.1:IR microspectroscopy, BL5.2:XAS, BL6a/b:micro-XRF, BL8:XAS
• **Scattering**: BL1.1W:MXT**, BL1.3W:SAXS/WAXS, BL7.2W:MX
• **Imaging**: BL1.2W: X-ray Tomography
• **Fabrication**: BL6a/b:DXL

Beamtime application

Available user beamtime at SPS is about 400 shifts/year or 4,400 hours/year which can be divided into 2 periods of beamtime allocation; period I(January – May) and period II(September – December). Beamtime proposal can be submitted online at http://www.slri.or.th 2 months in advance. All proposals will then be reviewed by committee.

There are two types of proposals can be submitted to utilize SLRI facility; non-propritary and propritary proposals. The prior can be submitted principal investigator (PI) or project leader through the beamtime applications decribed above. The latter can be submitted via the Business Development Division throughout the year at http://www.slri.or.th/bds/. (Beamtime fee and/or service can be charged.) Users are recommended to contact beamline manager or user office for technical advice.

References

[1]   Anonymous Synchrotron [online] Available: https://www.iop.org/publications/iop/2011/file_47 457.pdf, [17 August 2016], *Institute of Physics*.

[2]   P.Sudmuang *et al.*, Commissioning of the 2.4T multipole wiggler and the 6.5T superconducting wavelength shifter at Siam Photon Source, *Proceeding of IPAC2014*, Dresden, Germany, 2014.

[3]   List of beamlines: http://www.slri.or.th

Contact

S. Tancharakorn; tel: +66-44-217040 ext. 1477; somchai@slri.or.th

Operation and machine improvements of Siam Photon Source

P. Klysubun, P. Sudmuang, A. Kwankasem, S. Boonsuya, N. Suradet, S. Krainara,
T. Pulampong, S. Kongtawong and N. Juntong
Synchrotron Light Research Institute (Public Organization), 111 University Avenue, Muang District, Nakhon Ratchasima 30000, Thailand

Abstract

The accelerator system of Siam Photon Source has received several upgrades during the past year. Most notable of which was the installation of a 2nd RF system, which comprises of a 300 kV cavity and a 80 kW solid-state RF amplifier equipped with a digital low-level RF (DLLRF) controller. The injection system was optimized using Robust Conjugate Direction Search (RCDS) to deliver the record injection rate of more than 100 mA/min. The nonlinear effects from the two high-field insertion devices were carefully investigated. In addition, the booster synchrotron energy was upgraded to 1.2 GeV. Regarding operation, the Machine Group was able to provide more than 4,300 hours of user beamtime in the 2016 fiscal year with the machine availability of 97%.

Machine operation

In fiscal year 2016, which began from October 1, 2015 and ended on September 30, 2016, the Machine Group had operated the storage ring in user mode of operation. The monthly operation had been such that the first 5 days of each month were reserved for maintenance, installation, repair, and machine study. The rest of the month were user beam time. During these user beam periods the beam were provided to users 24/7. The beam was injected twice a day from 8:30 AM to 9:00 AM and from 8:30 PM to 9:00 PM. The maximum beam current was 150 mA. Thus, the number of user beamtime per day was 23 hours. A typical daily operation is shown in Fig. 1.
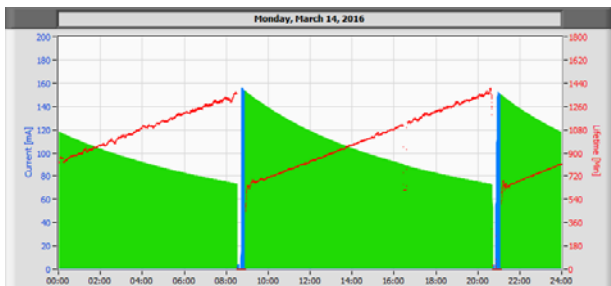
Figure 1: Example of daily SPS operation.

The total number of user beam time that was scheduled was 4,475 hours. The Machine Group was able to deliver 4,343 hours, corresponding to Machine Availability of 97.1%. (Fig. 2) The 11-year statistics for user beam time is also included in Fig. 2. Mean Time Between Failures (MTBF) and Mean Time To Recover (MTTR) of FY 2016 are shown in Fig. 3.

This template is an example for the submission of a manuscript. Applying guidelines as described in this paper

Figure 2: (top) User beam time and machine availability of FY 2016. (bottom) Operation statistics from FY 2006 to FY 2016.
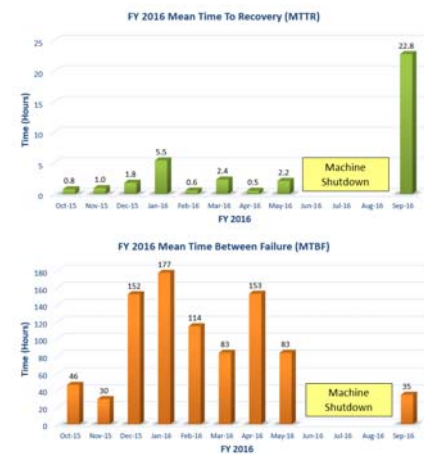
Figure 3: FY 2016 monthly MTBF and MTTR.

In Fig. 3, the MTTR of September 2016 is significantly higher than that of the other months. The reason is that the failure was the vacuum leakage at the front-end of BL1 beamline, which took considerable amount of time to recover.

In FY 2016 there were 60 instances of beam trip (Fig. 4). The most frequent cause came from magnet power supplies (14 times), followed by electrical system (8 times). The RF system, which caused considerable downtime the previous year, contributed only 12% this year (7 times). This is a good indication that the problems associated with the solid-state power amplifier had finally been resolved.

Figure 6: The new 80 kW solid-state RF amplifier.
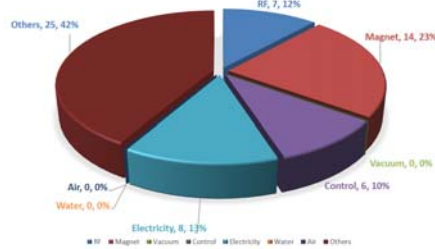
Machine improvements

2nd storage ring RF system

A new RF system was successfully installed in the storage ring during 2016 Machine Shutdown. The new cavity has maximum cavity voltage of 300 kV. (The old one has 125 kV.) The new amplifier has maximum power of 80 kW. (The old one has 30 kW.) The new system will allow the Machine Group to operate the superconducting wavelength shifter (SWLS) at its maximum magnetic field of 6.5 Tesla, which will in turn increase both the flux and the photon energy delivered to BL7 beamlines. However, increasing the SWLS magnetic field is currently pending in order to give the Safety Group the time to properly conduct the investigation of radiation level in the Experimental Hall. In the future, the stored beam current could be increased as well.

Improvement of injection efficiency

The Machine Group was able to improve the injection efficiency significantly by employing an optimization algorithm called Robust Conjugate Direction Search (RCDS), which was developed at SLAC. The algorithm successfully optimized the magnet currents of both LBT and HBT. After optimizing the LBT, the beam current in the booster synchrotron increased to more than 30 mA, and the injection rate to the storage ring increased from 40 mA/min to the record value of more than 100 mA/min. This enables the Machine Group to reduce the injection time by half, from previously 1 hour to merely 30 minutes.

Figure 5: The new 300 kV RF cavity.
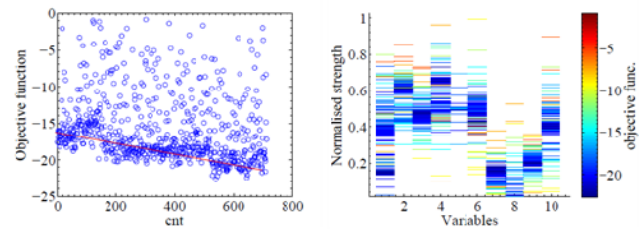
Figure 7: Injection optimization with RCDS.

In addition, the Machine Group had developed a system for monitoring the efficiency of the beam transfer between each step of the injection process, from the electron gun to the storage ring (Fig. 8). This system proved to be extremely useful in assuring efficient injection and investigating causes of low injection rate.

Table 1: Important parameters of the 300 kV cavity.

Parameters	Value
Resonant frequency	118 MHz
Maximum cavity power	30 kW
Maximum coupler power	120 kW
Shunt impedance $(V^2/2P)$	1.56 MΩ
Quality factor Q_0	19000
Operation Temperature	42 °C
Cooling Water Flow	241 l/min

Figure 8: Injection monitoring system.

Reduction of perturbations from IDs

Two high-field insertion devices, a 2.2 T multipole wiggler (MPW) and a 6.5 T superconducting wavelength shifter (SWLS) were installed in the SPS storage ring back in 2013. Installing such high-field magnets in a low-energy ring introduce considerable perturbation to the electron optics. Matching of optical functions as well as corrections of linear effects and closed orbit distortion were performed [1]. However, nonlinear effects had not been thoroughly studied and corrected due to time constraint.

Consequences from the nonlinear effects include reduction of beam lifetime and enlargement of electron beam size. After investigation, the main cause was found to be from the MPW. Its good field region is merely ±5 mm [2]. The most severe consequence is the reduction of dynamic aperture (DA), as shown in Fig. 9. The DA decreases by approximately 75% by the MPW. In the case of SWLS, the DA is reduced by only about 25%. This is the reason the beam cannot be injected to the storage ring when the MPW gap is fully closed.
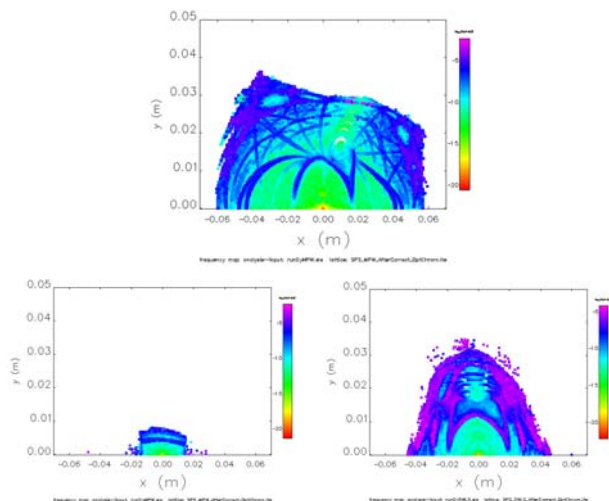
Figure 9: Dynamic apertures: (top) bare ring, (bottom left) with MPW, (bottom right) with SWLS.

Another factor affected by the nonlinear effect from the MPW is the momentum acceptance (MA), which in turn affects the beam lifetime. MA is typically linearly proportional to the RF acceptance, which is determined by the RF voltage. However, it can be limited by the nonlinear effects, as shown in Fig. 10.
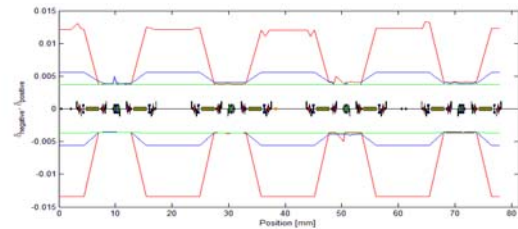
Figure 10: Momentum acceptance of the SPS storage ring with MPW when RF cavity voltage was 115 kV (green), 125 kV (blue), and 300 kV (red).

Acknowledgements

References

[1] P. Sudmuang *et al.*, Commissioning of the 2.4 T Multipole Wiggler and 6.5 T Superconducting Wavelength Shifter at Siam Photon Source, in *Proc. IPAC '14*, 2014, 1192-1194.

[2] T S. Krainara *et al.*, Analysis of Nonlinear Effects for IDs at the SPS Storage Ring, in *Proc. IPAC '16*, 2016, 3515-3517.

Contact

*P. Klysubun, tel: +66-44-217040 ext 1512; pklysubun@slri.or.th

Design of local shielding for SWLS at Siam Photon Laboratory

S. Vanitparinyakul, M. Sophon and *S. Ruengpoonwittaya*
Synchrotron Light Research Institute (Public Organization), 111 University Avenue, Muang District, Nakhon Ratchasima 30000, Thailand

Abstract

A 6.5T Superconducting Wavelength Shifter (SWLS) donated by NSRRC, was installed and commissioned at the 1.2 GeV electron storage ring of the Siam Photon Source. This report presents the calculation of radiation shielding of local shielding design for the hot spot of radiation along the vacuum components at downstream of the SWLS.

Introduction

The SWLS is the second insertion device of Siam Photon Laboratory which installed at the middle of long straight section of the 1.2 GeV storage ring between Bending Magnet No.6 (BM6) and No.7 (BM7) in 2013. Because of the power from the old RF system is insufficient to compensate the power loss of electron beam then the SWLS needs to be operated at 4.5T instead of 6.5T.

The new RF system was constructed, installed and commissioned with electron beam in 2016. The RF power from new system is sufficient to deal with the operation of SWLS at 6.5T. The radiation dose monitoring along the downstream components of SWLS is a way to look for the hot spot of radiation while SWLS is operating.

Radiation dose surveying
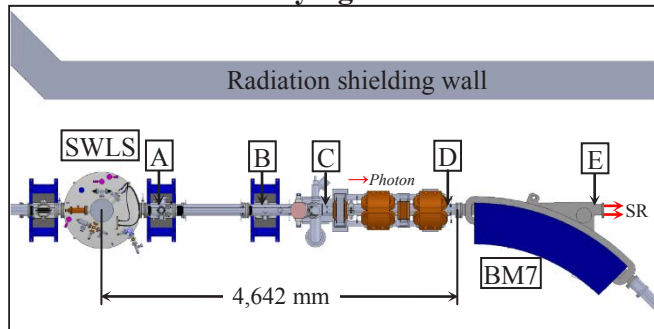
Figure 1: The radiation dose surveying of SWLS

DoseRAE2, an electronic dosimeteris a compact device for radiation measurement, can be used for radiation dose monitoring at the various points along the downstream of vacuum components of SWLS. It consists of a diode and a scintillation crystal to detect X-ray and gamma radiation, and provide real-time monitoring of 0.01uSv/hr to 10 Sv/h for radiation dose and 0 uSv/ 10 Sv for accumulated dose.

Radiation dose was recorded using 2 electronic dosimeters at each positions (see Fig. 1) from A to E. The first dosimeter was necessary to be wrapped with a 1.5 mm-thick of lead (Pb) sheet while the second one was placed without any shielding material.

The Table 1 shows all of the data from radiation dose surveying. The result after 1 hour and 5 hours shows the highest radiation dose at the position "D". The increasing of radiation dose is obviously seen in the operation of SWLS at 6.5 T instead of 4.5 T while the RF voltage will not much effect to the increasing of radiation dose.

Table 1: The experimental result of radiation monitoring

SWLS	4 T	6.5 T			
RF (Oper. volt)	185 kV	185 kV		200 kV	
Time	1 hr	1 hr		5 hr	
Position	*Radiation Dose (mSv)*				
	No Lead	No Lead	Lead	No Lead	Lead
	Lead				
A	0.0136	0.0061	0.0272	0.0050	0.1013	0.0149
B	0.0030	0.0020	0.0287	0.0025	0.0939	0.0071
C	0.1652	0.0016	20.5008	0.0083	707.3961	0.0241
D	0.3648	0.0023	84.3938	0.0042	1,069.8751	0.0180
E	0.0041	0.0031	0.3190	0.0022	1.9161	0.0073

The radiation dose from the dosimeter wrapped with a 1.5 mm-thick of lead sheet is significantly less than the another dosimeter, the effect of synchrotron radiation contribution is more dominant than Bremsstrahlung radiation which could be produced by high energy particles.

Tenth value layer calculation

The concept of Tenth value layer (TVL) is widely used in radiation shielding design. The TVL calculation can define the siutable thickness of a shield or an absorber that reduces the radiation level by a factor of one tenth from the initial level. The TVL calculation equation can be adopted from the Beer–Lambert'slaw [2].

$$I = I_o e^{-\mu_m t_d} = I_o e^{-(\frac{\mu}{\rho})t_d} = I_0 e^{-\mu t} \qquad (1)$$

I is the unattenuated gamma ray beam intensity
I_0 is the attenuated gamma ray beam intensity
μ_m (cm^2/g) is the mass attenuation coefficient, function of photon energy
t_d (g/cm^2) is the density thickness of the absorber
μ (cm^{-1}) is the linear attenuation coefficient
ρ (g/cm^3) is the density of material
t (cm) is the thickness

Then the TVL calculation can be simplified from the equation (1) as:

$$TVL = \frac{\ln 10}{\mu} = \frac{2.3026}{\mu} \qquad (2)$$

The TVL calculation from equation (1), (2) and take the mass attenuation coefficient [1] for various materials can be shown the result on the Fig. 2.
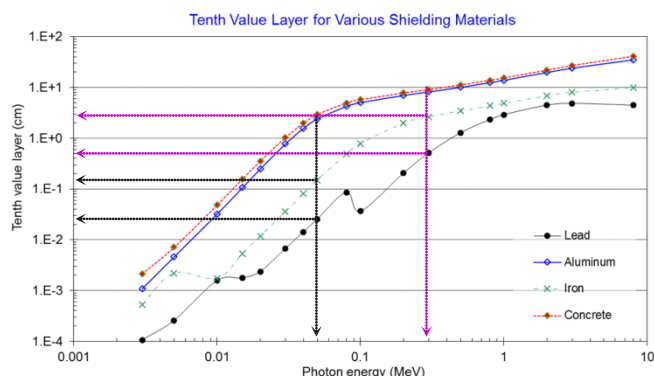

Figure 2: Tenth Value Layer for various materials.

Because of the effect from synchrotron radiation contribution is more dominant than Bremsstrahlung radiation. The calculation of shielding design at 50 KeV of photon energy instead of 1.2 GeV of electron beam energy is more reasonable for the vacuum component of SWLS. The black dot line on the Fig. 2 shows the TVL for various materials which corresponds to 50 KeV of photon energy. The factor of safety for this calculationis aimed to 20 times of TVL at 50 KeV which corresponds to 0.3 MeV of photon energy then the suitable thickness of various materials can be represented by the pink dot line on the Fig. 2.

Local shielding design for SWLS

Due to the highest radiation dose located at the position "D" where the L4-2 vacuum chamber has been installed at the end of long straight section. The Fig. 3 shows the detailed design of L4-2 vacuum chamber which consists of a pair of lateral photon absorbers. In order to protect the other components after L4-2 vacuum chamber from the heat of incidence photon beam, the lateral photon absorbers have been designed to confine the width of photon beam from SWLS into the smaller horizontal opening angle.
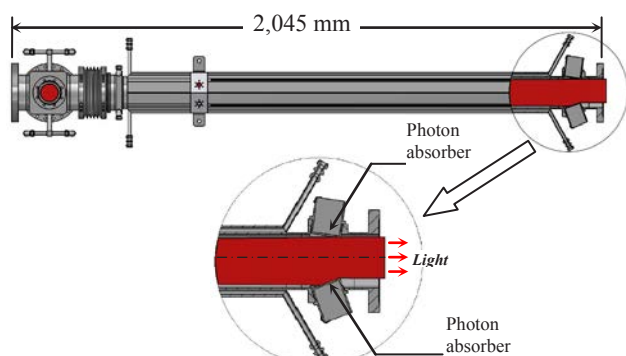
Figure 3: Detailed design of L4-2 vacuum chamber.

Lead and iron were considered for the material of local radiation shielding of SWLS component because of the cost effective comparing to aluminumat the same weight, and more convenient to manufacture than high strength concrete. The TVL of lead and iron at 0.3 MeV is about 0.50 cm. and 3.00 cm, respectively. Density of lead is 11.34 g/cm^3, while iron is 7.874 g/cm^3. Finally, lead is selected to use for the radiation shielding of this design because it is lighter than iron when compared with the same area but difference thickness.
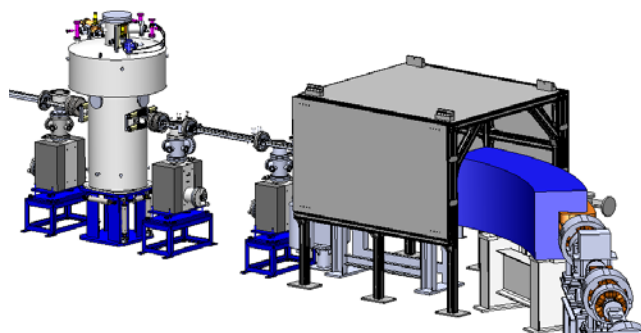
Figure 4: The design of local shielding for L4-2 vacuum chamber.

The main structure of local shielding for L4-2 vacuum chamber of SWLS has been designed by aluminum frame while the roof and side wall were made from 4.5 mm-thick of lead sheet sandwiched with 2 mm-thick of steel sheet. The Fig. 4 shows the computer design of local shielding for L4-2 vacuum chamber of SWLS. The local shielding is going to install in the storage ring in the period of annual shutdown in 2017.

Acknowledgement

References

[1]   Hubbell, J.H. *et al*., Tables of X-Ray Mass Attenuation Coefficients and Mass Energy-Absorption Coefficients (version 1.4). [Online] Available: http://physics.nist.gov/xaamdi [2007, January 17]. National Institute of Standards and Technology, Gaithersburg, MD., 2004.

[2]   Md. Fazlul Huq *et al*., Calculation of gamma-ray attenuation parameters for locally developed shielding material: Polyboron., *Journal of Radiation Research and Applied Sciences*, 2016, 26-34.

Contact

*S. Vanitparinyakul, tel: +66-44-217040 ext 1158; sarinya@slri.or.th

BL1.1W, the new multiple X-ray techniques beamline at Siam Photon Laboratory

P. Chirawatkul[1], C. Saiyasombat, S. Pongampai, K. Kamonsuangkasem*

R. Klondon and P. Pongchalee

Synchrotron Light Research Institute (Public Organization) 111 University Avenue, Muang District, Nakhon Ratchasima 30000, Thailand

Abstract

The multiple X-ray techniques beamline (BL1.1W) was opened for user service in October 2016. The XAS technique was the first available technique followed by the XRF and WAXS. The beamline optical elements have been designed to optimize the use of X-rays in the energy range of 4 to 18 keV from the newly installed 5-period multipole wiggler. The commissioning result shows the full beam size of 5 mm × 2.5 mm at the sample position and X-ray fluxes range from 10^6 to 10^9 ph/sec/0.1%bw with an energy resolution of 10^{-4}. XAS and XRF measurements in the energy range of 4 to 18 keV is now available along with WAXS measurements with the scattering angles up to 40 degree. A plan to add XRD technique to the end-station is underway and the upgrade is expected to finish in 2018.

Introduction

The BL1.1W has been designed and built with the multi-probe approach. The aim of the design is to combine XAS (X-ray absorption spectroscopy) technique with other structural probes. The choice of wiggler as a source has been to allow two X-ray mirrors along the beam path and Si (111) crystals in the monochromator while retaining usable X-ray fluxes. The wiggler also helps extending the X-ray energy range for the XAS measurements up to 18 keV.

Since October 2016, the XAS technique has been opened for proposals. The XRF (X-ray fluorescence) technique has been added in January 2017 and the WAXS (wide angle X-ray scattering) technique in March 2017. XRF elemental analysis could be used together with the XAS to allow both elemental identification and speciation of the samples. The WAXS technique is appropriate to provide additional information regarding the phase and d-spacing of the samples. The use of more than one technique for a single experiment is encouraged. The multiple sample holders and a furnace were also developed for this first phase of the beamline operation to accommodate increasing demands for high throughput and *in-situ* experiments. Moreover, the X-ray powder diffraction (powder XRD) will be installed at the end-station in 2018 to provide a more complete structural picture of the samples.

The BL1.1W has been constructed following the MOU between Khon Kaen University (KKU) and Synchrotron Light Research Institute (Public Organization) or SLRI to promote the use of synchrotron light source to KKU lecturers and researchers. When this first phase of construction is finished, an agreement has been reached between the KKU and SLRI such that, since January 2017, 50 % of user beam time at the BL1.1W is reserved for research projects from the KKU and one post-doc staff funded by the KKU is employed at the beamline. Another 50 % of the beam time is still a public beam time accepting proposals under SLRI policy.

This manuscript is arranged as follows. The conceptual design of the beamline is described in the next part followed by the presentation of the commissioning results. A description of the current end-station setup and its capability are subsequently shown with the summary given in the last part.

Conceptual design

Source

The source for the BL1.1W is a 5-period multipole wiggler (MW) with an effective magnetic field of 2.2 T and an opening port of 7.5 mrad offset from the MW center line. The nominal fluxes of the 7.5 mrad offset port calculated for the MW including those for the MW center line and a typical SLRI bending magnet (BM) are shown in Fig. 1. From the figure, the high flux from the MW is essentially retained despite the port offset. Compared to the BM source, by utilizing the MW, usable X-ray range could be extended to higher energy. The beam divergence however has to be compromised, with the wiggler *K* factor of 45, the horizontal divergence is expected to be around 9 mrad.
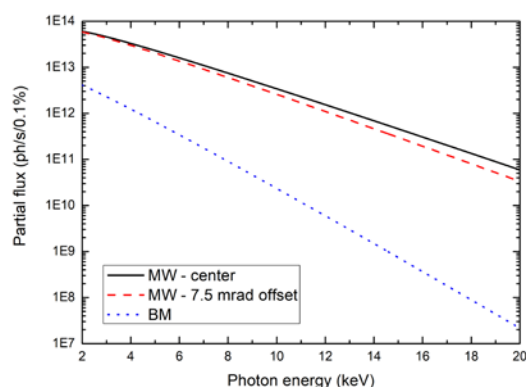
Figure 1: Partial fluxes calculated for the 5-period MW and an SLRI standard BM. The calculation was performed using SPECTRA [1] with the SLRI machine parameters and an opening angle of 3 mrad horizontally and full beam vertically.

Optical components

There are three main optical elements in BL1.1W; a collimating mirror (CM) to collimate the beam vertically, a fixed-exit double crystal monochromator (DCM) and a focusing mirror (FM), which is toroidal and used to focus the beam vertically and horizontally to the sample position. The conceptual layout of the beamline is shown in Fig. 2.
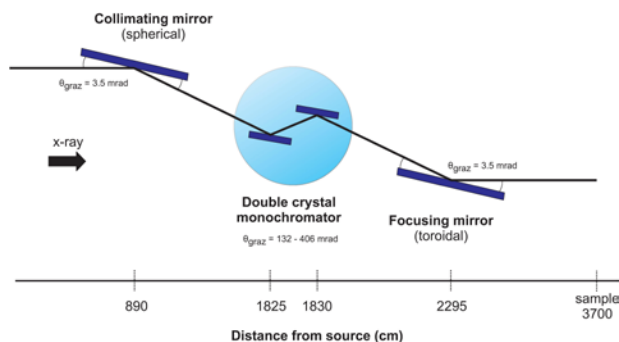
Figure 2: BL1.1W conceptual layout depicting three main optical elements, namely, a collimating mirror (CM), a double crystal monochromator (DCM) and a focusing mirror (FM) at their corresponding distance from the source. The grazing angles for both mirrors with relative to the beam direction are also shown.

Both the CM and FM are coated with a layer of 50 Å thick Rh on top of a 250 Å thick Pt. The reflectivity curve from this bi-layer surface at 3.5 mrad grazing angle along with those of the Rh and Pt are shown in Fig. 3. As seen from the figure, the Rh layer reduces the effect of Pt L absorption edges at around 11.5 keV and the Pt layer helps extending the usable X-ray range to over 20 keV. Therefore, by using this bi-layer coating at the grazing angle of 3.5 mrad, the beamline could be optimized for X-ray with the energy range available from the MW.
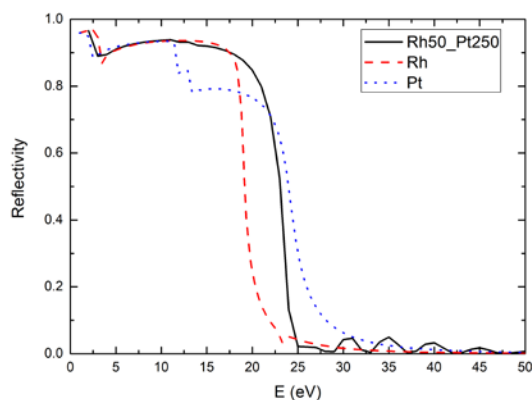
Figure 3: Reflectivity from Rh, Pt and a 50 Å layer of Rh on top of a 250 Å layer of Pt surfaces at grazing angles of 3.5 mrad as a function of photon energies. The calculation was made using the XOP toolkit [2].

The design of the beamline has been made to make it possible to accommodate both spectroscopy and scattering techniques. The crystals used in the DCM are Si (111) which, in combination with a vertically collimated beam, could give the energy resolution of 10^{-4} optimizing the energy resolution for the XAS technique. The energy range of X-rays available from the mechanic of the DCM is between 2 to 20 keV which covers usable energy range from the MW. Due to the large beam divergence of the MW, it is

not possible to have a symmetric beam profile ideal for scattering experiments. Ray tracing [2] was employed to optimize the beam designed value to the beam size of 3 mm × 1.5 mm with a 2:1 ratio between horizontal and vertical dimensions.

Commissioning result
Flux
The actual beam flux was measured using an ionization chamber filled with Ar to the operating pressure. The result is shown in Fig. 4. Compared to the calculated partial flux in Fig. 1, the actual flux is around three orders of magnitude lower than that from the source. This is mostly due the choice of Si (111) as crystals in the monochromator [3]. The photon flux at low energy is also much lower than that from the source which is most likely due to the inclusion of Be windows and an absorption edge of Ar which is used to fill the ionization chamber. Two Be windows are used as vacuum separators along the beamline, however, due to its high-pass filter property, fluxes at the energies lower than 4 keV are significantly decreased.
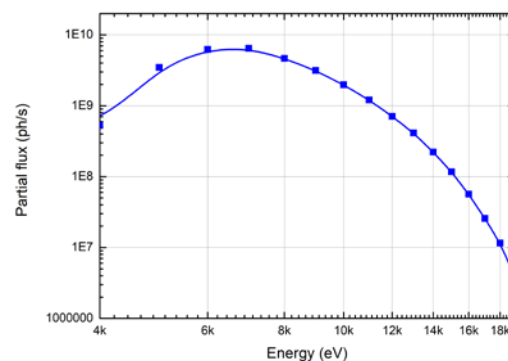
Figure 4: Partial flux measured at the end-station. The available flux from the beamline is in the range of 10^6 to 10^9 with maximum around 6 to 8 keV and usable X-rays in the range of 4 to 18 keV.

Energy resolution
The energy resolution of the beamline was determined by recording the rocking curve of the first DCM crystal, Fig. 5. As seen from the figure, the width of the rocking curve for the 5, 10 and 17 keV X-rays are 18, 10.6 and 7.3 arcsec, respectively, which infers the energy resolution of $2\text{-}3\times10^{-4}$.

The XANES (X-ray absorption near edge structure) spectrum of Cu foil was measured to check the effective energy resolution. Fig. 6 shows the measured spectrum together with the reference spectrum taken from the Hephaestus database [4]. From the figure, the shoulder feature in the BL1.1W XANES spectrum at 8981.5 eV was well separated from the edge position at 8979 eV. This implies an energy resolution of (8981.5-8979)/8979 = 2.8×10^{-4}, which is close to the value determined from the rocking curve.
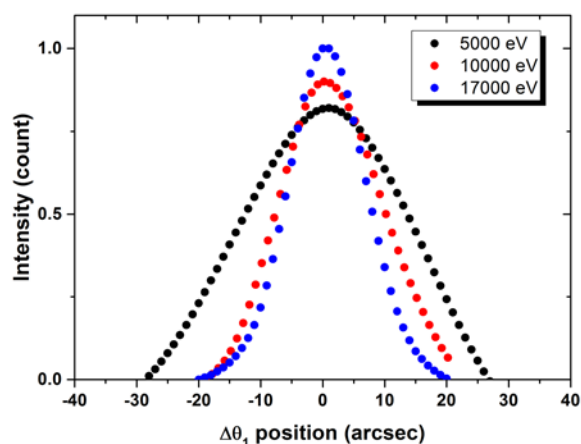
Figure 5: Recorded rocking curves from the first DCM crystal. The data were taken at 5, 10 and 17 keV. The result confirmed the designed energy resolution of 10^{-4}.
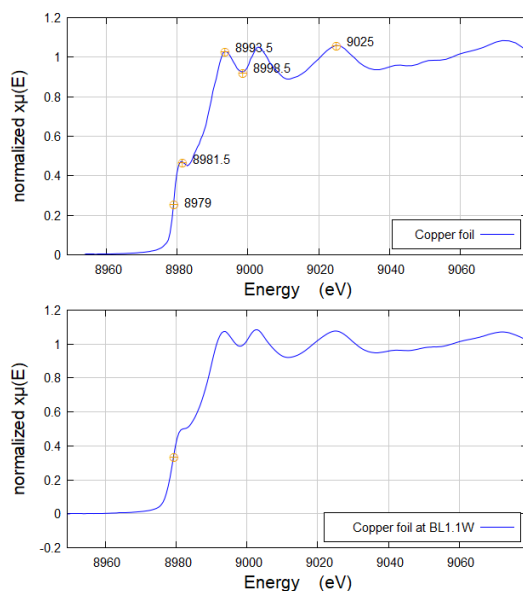
Figure 6: XANES spectra of Cu foil. The top graph shows the spectrum measured at the X11A beamline at the NSLS taken from the Hephaestus database [4] with reference feature positions in energy. The bottom graph shows the spectrum measured at the BL1.1W.

Beam profile

The beam profile along the beamline was monitored using a combination of phosphor screens placed after each optical element and wire scans. Fig. 7 shows a beam profile as seen from the phosphor screen placed at the sample position. The beam is an oval shape with a larger horizontal dimension. The size of the full beam is 5 mm × 2.5 mm which is about 60% larger than the design values. This could be due to alignment or practical factors such as slope error or surface roughness of the mirrors.
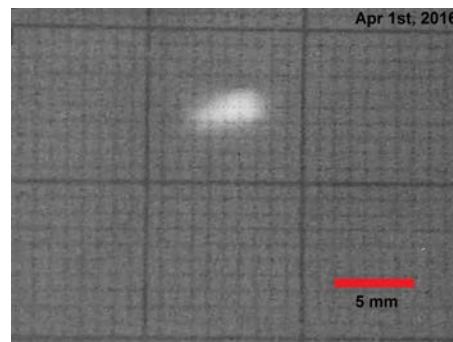
Figure 7: Beam profile at the sample position. The beam profile was captured by using a phosphor screen placed at the sample position. The estimated beam size is 5 mm × 2.5 mm.

End-station

The end-station of BL1.1W during the XAS setup is shown in Fig. 8. The beamline end-station is equipped with three types of detectors, namely, a set of three ionization chambers for XAS measurements in transmission mode, a 19 array Canberra Ultra LEGe detector for XRF measurements as well as XAS measurements in fluorescence mode, and a MAR345 image plate detector for WAXS measurements.
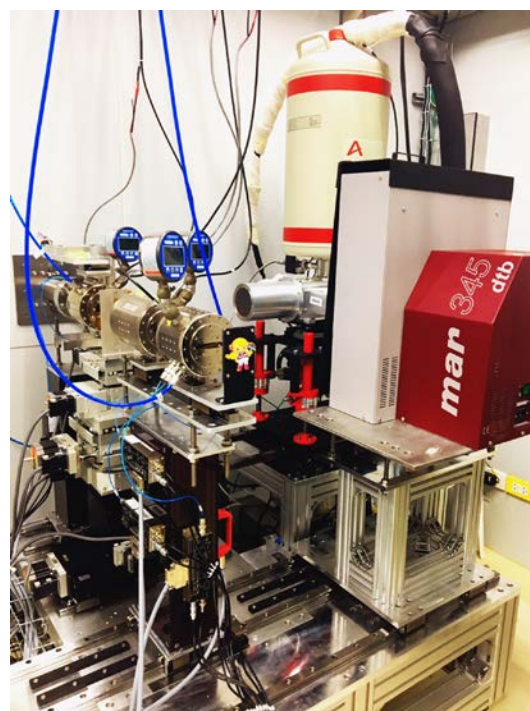
Figure 8: BL1.1W end-station with three detectors installed for XAS, XRF and WAXS measurements. The end-station is installed on a movable support such that simple sliding movements can be used to change from one setup to another.

The usable energy range for XAS experiment is between 4 to 18 keV which covers the K-edge of Ca up to the K-edge of Zr and the L_{III}-edge of Antimony up to the L_{III}-edge of Actinium including the Lanthanides. Fluorescence mode measurements allow lower concentration samples to be measured. Qualitative and quantitative XRF analyses are available. The WAXS detector is installed with the sample-to-detector distance of approximately 280 mm providing WAXS measurements with scattering angles up to 40 degree.

Electronics of the beamline and motorized stages are controlled locally using in-housed LabVIEW based applications including the XAS data collection software, XAS scan macro. The XRF and WAXS data collections are made using third-party software; XIA's Prospect program for the XRF data collection and the MAR345 program for the WAXS data collection. All collected data are stored in the beamline server which could be accessed by users after the experiment upon request.

Sample stage

At BL1.1W, samples are typically measured in air. Multiple sample holders for transmission and fluorescence mode of measurements are available. Moreover, for XAS experiments, an in-housed developed octagon furnace is available upon request. The maximum holding temperature of the furnace is 750 °C with programmable temperature steps. The furnace is equipped with a gas inlet/outlet such that measurements under a constant flow of inert gas or N_2 are possible.

Figure 9: The octagon furnace available at the BL1.1W. The furnace has been developed for XAS experiments both in transmission and fluorescence modes and is capable of raising the temperature up to 750 ^{O}C.

Summary

The BL1.1W installation project has finished in October 2016. The MW source has been employed to extend the usable photon flux up to 18 keV. The optical elements have been designed to provide high energy resolution beam in the energy range from 4 to 18 keV with mm beam size. The commissioning result shows reasonable agreement with the designed values with some rooms for optimization.

The beamline is now accepting proposal for XAS, XRF and WAXS measurements. Extended scattering angles for the WAXS technique and additional sample environments are underway including the installation of powder XRD end-station which is expected to finish in 2018.

References

[1] T. Tanaka *et al*., SPECTRA: a synchrotron radiation calculation code, *J. Synchrotron Rad.*, 2001, 8, 1221-1228.

[2] M. Sánchez del Río *et al*., XOP v2.4: recent developments of the x-ray optics software toolkit, *Proc. SPIE*, 2011, 8141, 814115.

[3] M. Sánchez del Río *et al*., A simple formula to calculate the x-ray flux after a double-crystal monochromator, *Proc. SPIE*, 2004, 5536, 157.

[4] B. Ravel *et al*., ATHENA, ARTEMIS, HEPHAESTUS: data analysis for X-ray absorption spectroscopy using IFEFFIT, *J. Synchrotron Rad.*, 2005, 12,537-541.

Contact

*P. Chirawatkul; tel: +66-44-217040 ext 1471; prae@slri.or.th

BL2.2: time-resolved X-ray absorption spectroscopy (BONN-SUT-SLRI) beamline

Y. Poo-arporn[1], W. Limphirat[1], S. Tonlublao[1], S. Duangmanee[2],
S. Klinkhieo[1], J. Hormes[3] and P. Songsiriritthigul[4]

[1]Synchrotron Light Research Institute (Public Organization), 111 University Avenue, Muang District, Nakhon Ratchasima 30000, Thailand
[2]School of Chemistry, Suranaree University of Technology, 111 University Avenue, Muang District, Nakhon Ratchasima 30000, Thailand
[3]Canadian Light Source, University of Saskatchewan, 101 Perimeter Road, Saskatoon, SK S7N OX4, Canada
[4]School of Physics, Suranaree University of Technology, 111 University Avenue, Muang District, Nakhon Ratchasima 30000, Thailand

Abstract

An energy dispersive X-ray absorption spectroscopy beamline has been constructed at the Synchrotron Light Research Institute (SLRI), Thailand. The beamline was designed to utilize the synchrotron radiation with photon energies between 4000 eV and 12000 eV. The horizontal focusing of the bent crystal in the energy dispersive monochromator offers a small polychromatic focal spot of 1 mm at the sample position. By employing an energy dispersive scheme, the whole X-ray absorption near edge structure (XANES) can be obtained simultaneously using a position sensitive detector with the fastest readout speed of 25 ms. The short data collection time opens a new opportunity for time-resolved X-ray absorption spectroscopy (XAS) experiments such as studies of changes of the electronic structures or the local coordination environments of an atom during a change in thermodynamic conditions.

Introduction

X-ray absorption spectroscopy (XAS) has been widely used to determine valance states or local structures of various materials [1, 2]. In a conventional XAS setup, a XAS spectrum measurement involves a mechanical scanning of a double crystal monochromator (DCM). This limits the data acquisition time to several minutes. Thus, it is not possible to monitor rapid changes of local structures or valence states of some processes such as the change in the valence state of Fe (III) porphyrin during a photo induced electron transfer [3] and the change of Fe neighboring atoms during a dissociation of ferrioxalate [4], processes that take place within 10 ms and 115 ps, respectively. To overcome this problem, two schemes to increase the data collection speed have been proposed. For the first scheme, called the quick scanning EXAFS (QEXAFS), a typical DCM is replaced by a piezo-driven [5] or a cam-driven DCM [6], and an XAS spectrum can be measured in milliseconds. The second scheme uses an energy dispersive setup [7-10] which allows the whole XANES spectrum to be measured simultaneously and the data collection speed is mainly limited by the electronics of the detector, which is typically in the range of a millisecond or microsecond.

Energy dispersive setup

In an energy dispersive XAS (EDXAS) setup, a bent crystal is employed to disperse and focus X-rays with a continuous band of photon energies (Fig. 1). Using the energy dispersive scheme, XAS spectra can be obtained

with less vibration-induced noises compared with the conventional setup as there are no mechanical movements during the measurements. The beam size at the sample position can be small which allows small samples to be measured, and a good output-linearity and a wide dynamic range of a position sensitive detector (PSD) gives a good signal-to-noise ratio data and a fast detection speed [11]. A number of researches have been made using the EDXAS setup. These include the study of $Cu^{2+} \rightarrow Cu^{+}$ transformation in a cathodic reduction of Cu in conductive polymers [12] where Cu K-edge XANES spectra were measured every 7.2 s, the investigation of a thermal dehydration process in a Ni^{2+} ion exchanged zeolite Y [13] using Ni K-edge XANES, and the crystallization of some nanomaterials [14].
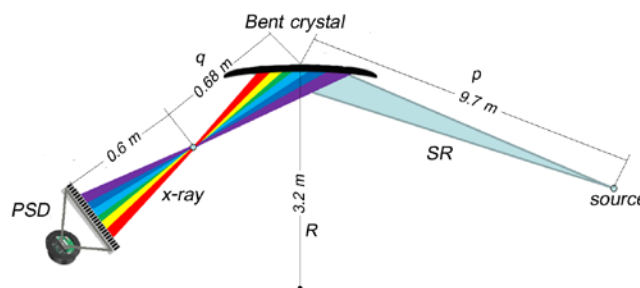
Figure 1: An optical layout for an EDXAS scheme. X-ray with a certain energy bandwidth is selected by a bent crystal. The selected X-rays are focused at the sample position. The position sensitive detector (PSD) is placed downstream to the sample to detect all the transmitted X-rays simultaneously thus allowing the measurement of an XAS spectrum in a short period of time.

TRXAS beamline

The time-resolved XAS (TRXAS) beamline is designed to utilize synchrotron radiation generated from a bending magnet of a 1.2 GeV storage ring of the Siam Photon Source. It employs the energy dispersive monochromator (EDM) and a 2-theta arm with an angular range from 20 to 140 degrees which were donated by the University of Bonn, Germany (Fig. 2). The components belonged to a decommissioned beamline at the Electron Stretcher and Accelerator (ELSA) of the University of Bonn. With a Si (111) crystal, the EDM covers photon energies between 4000-12000 eV, allowing the K-edges of Ca to As to be investigated at this beamline. The rest of the beamline components was designed and fabricated in-house.

Figure 2: Photo of the TRXAS end-station showing, from left to right, an EDM, a three-axis stage, and a 1024 channels NMOS linear image sensor.

The rectangular-shape Si (111) crystal with an area of 25×250 mm^2 and a thickness of 1 mm was used as a bent crystal. The elliptical curvature of the crystal is adjustable using a crystal bender which is mounted on a three-axis goniometer placed inside the monochromator chamber. The goniometer allows the crystal to be rotated around three axes and translated vertically. The axes of rotation are the vertical axis, the axis normal to the crystal surface, and the axis along the length of the crystal. The distance between the center of the crystal and the source point is 9.7 m. This distance was set to be as short as possible for a high photon flux and a large acceptance angle on the bent crystal.

A PSD generally consists of a multi-element photodiode array which converts an incoming electromagnetic radiation into a recordable signal such as a current or a voltage using the photoelectric effect [15]. The PSD at the TRXAS beamline is a commercially available NMOS linear image sensor model S3904-1024N from the Hamamatsu Company. The photodiode array contains 1024 elements each with an N-type diffusion layer formed on a P-type silicon substrate as a P-N junction and an active area of 20 μm × 2.5 mm. This detector uses a charge integration method to collect a signal. The generated electrical charges are temporarily stored in the junction capacitance of each photodiode and subsequently read out through the video line. The fastest readout frequency of the S3904-1024 model is 50 kHz. Thus, with 1024 photodiodes, the minimum time for the signal to be read out is 20 μs × 1024 = 20.48 ms. Hence, the fastest detection speed for this model is set to be 25 ms. The advantage of this data collection procedure is that the intensity of the signal output depends on the integration time which can be increased for low-light-level detection. However, as the charge-storage capacity is limited, the signal output will not increase if the intensity of the light is higher than the saturation level of the detector. The maximum storage charge capacitance for this model is 25 pC.

Commissioning results and performance test
Beamline commissioning

The performance of the TRXAS end-station for time resolved measurements was tested by measuring the Ti K-edge XANES spectra of a 5 μm thick Ti foil (Fig.3). A XANES spectrum had been successfully recorded using the data-acquisition speed of 25 ms. However, the spectrum showed a poor signal-to-noise (S/N) ratio. The S/N ratio could be improved by increasing the integration time. It was found that XAS spectra with a good S/N ratio could be obtained when the integration time is 200 ms or longer.
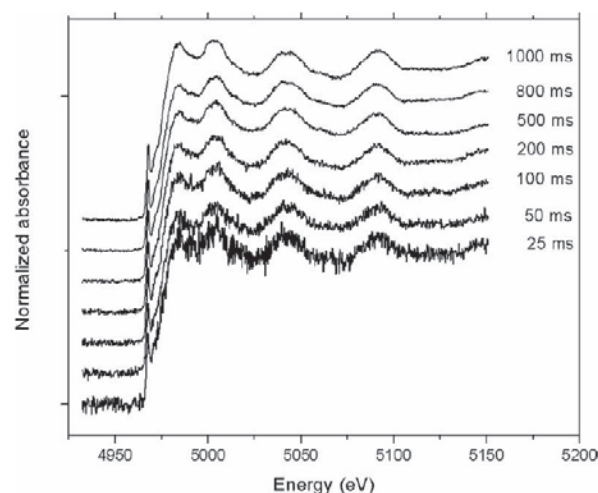
Figure 3: Normalized Ti K-edge XANES spectra for a 5 μm thick Ti foil measured using integration time of 25, 50, 100, 200, 500, 800 and 1000 ms.

In-situ XANES measurement

The amorphous-TiO$_2$ phase transformation under a calcination condition was chosen to test the capability to perform an *in-situ* measurement at the TRXAS beamline. TiO$_2$ (TiSG) was prepared by the sol-gel method. Titanium isopropoxide (TTIP) was added to the mixture of 2-propanol and ethylene glycol under magnetic stirring in a glove box. The suspension was continuously stirred at room temperature for 15 min and kept in an inert atmosphere for 24 hours. The gel was dried at 383 K (D-TiSG) before the *in-situ* XANES measurement. To produce crystalline TiO$_2$ (C-TiSG), the D-TiSG was calcinated in air at 873 K for 1 hour.

The prepared sample was put into the *in-situ* cell and heated using a heating rate of 2 K min^{-1} from room temperature to 723 K in air. Ti K-edge XANES spectra were recorded at room temperature and then every 50 K between 323 K and 573 K. From 573 K to 723 K where the phase transformation was expected, the spectra were recorded in 10 K intervals. The integration time was chosen to be 250 ms and each spectrum was an average of 10 scans which gave a time resolution of 2 s.
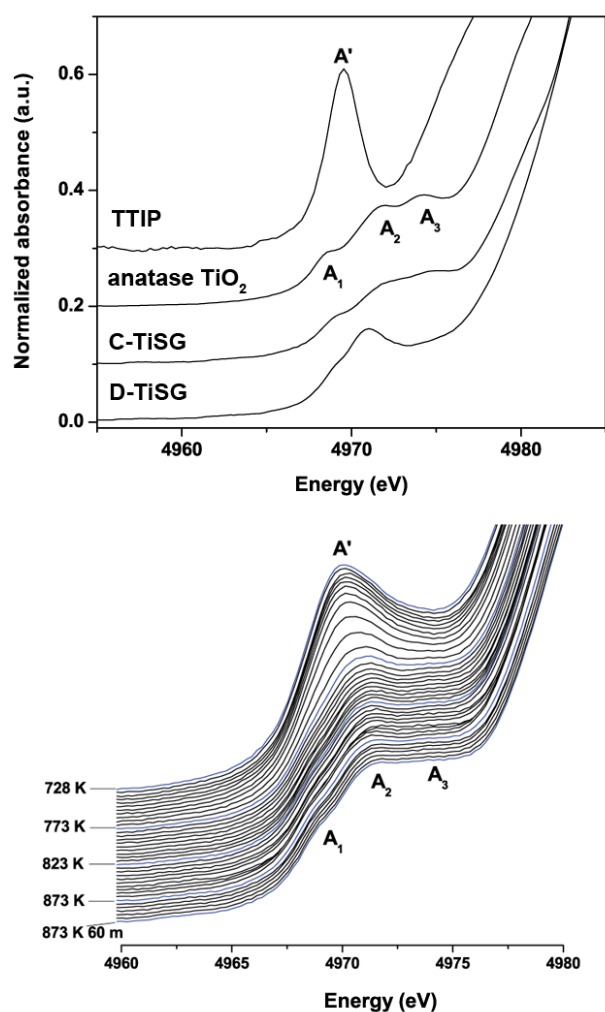
Figure 4: (a) Normalized Ti K-edge XANES of standard anatase, TTIP, D-TiSG and C-TiSG and (b) demonstrating a phase transition of D-TiSG caused by the temperature change.

The normalized Ti K-edge XANES spectra of standard anatase TiO_2, TTIP, D-TiSG and C-TiSG were shown in Fig. 4. Their pre-edge peaks in the energy range from 4960 to 4980 eV were corresponding to the 1s→3d transitions. The tetragonal structure of TTIP reflected the single intense pre-edge peak (A") at 4969.5 eV. For the dried TiSG, the intensity of pre-edge peak A" was significantly dropped with the developing of new peak at 4971 eV. The results suggested formation of Ti-O cluster in gel through the sol-gel process. For cytalline TiO_2, the octahedral structure of anatase produced 3 pre-edge peaks in XANES spectra. The characteristics of these peaks were be reported by Farges et al. [16]. The A_1 is attributed mainly to the quadrupole transitions to the t_{2g} levels in the TiO_6 octahedron while the A_2 and the A_3 peaks are attributed to the 1s to 3d dipole transitions and are designated as 1s → t_{2g} and 1s → e_g transitions, respectively.

After calcination, D-TiSG revealed three pre-edge peaks similar to the anatase. The formation of anatase in D-TiSG under calcination process was further monitored by the *in-situ* XANES measurement. Ti K-edge XANES spectra were recorded in 5 K intervals from 373 K to 823 K. At temperature lower than 728 K, there was no significant change of pre-edge peak. The intensity of A_1 peak began to reduce at 733 K. The drastically change of intensity together with peak shifting were observed at temperature between 743 and 773 K. Three pre-edge peaks corresponding to the anatase were clearly observed at 823 K. Although the calcinations temperature was increased to 873 K with holding for 60 min, there was no indication of the rutile phase of TiO_2. This result indicated the stability of anatase phase at temperature between 823-873 K. However, it should be noted that, the maximum temperature for the current setup of the *in-situ* XANES measurement is 873 K.

Conclusions

The TRXAS beamline has been successfully constructed at the SLRI. By using the energy dispersive scheme, with the 1024 elements photodiode array NMOS linear image sensor, the shortest data acquisition time of 25 ms for Ti K-edge XANES spectra was demonstrated. An in-house *in-situ* cell has been developed and tested at the TRXAS beamline to observe the change in the XANES spectra during a thermal treatment. Thermal treatment in the production of TiO_2 by the sol-gel method was selected as an *in-situ* example experiment. The XANES spectra measured during the heating process showed a clear formation of the anatase structure.

Acknowledgements

References

[1] Hedman, B *et al*., X-ray Absorption Fine Structure XAFS13: 13th International Conference. *AIP Conf. Proc.*, 2007, 882 and references therein.
[2] Bunker, G.. Introduction to XAFS: A Practical Guide to X-ray Absorption Fine Structure Spectroscopy, New York: Cambridge University Press and reference therein., 2010.
[3] Chen, L. X. *et al*., *J. Synchrotron Rad.*, 1999, 6, 403-405.
[4] Chen, J. *et al*., *Chem. Phys. Lett.*, 2007, 437, 50-55.
[5] Lützenkirchen-Hecht, D. *et al*., *J. Synchrotron Rad.*, 2001, 8, 6-9.
[6] Caliebe, W. A. *et al*., *Radiat. Phys. Chem.*, 2006, 75, 1962-1965.
[7] Flank, A. M. *et al*., *Nucl.Instrum. Methods Phys. Res.*,1983, 208, 651-654.
[8] Blank, H. *et al*., *Rev. Sci. Instrum.*, 1992, 63, 1334-1337.

[9] Pascarelli, S. *et al.*, *J. Synchrotron Rad.*, 1999, 6, 146-148.

[10] Cezar, J. C. *et al.*, *J. Synchrotron Rad.*, 2010, 17, 93-102.

[11] Fontaine, A. *et al.*, *Nucl.Instrum. Methods Phys. Res.*, 1987, Sect. A 253, 519-522.

[12] Dartyge, E. *et al.*, *Nucl. Instrum. Methods Phys. Res.*, 1986, Sect. A, 246, 452-460.

[13] Couves, J. W. *et al.*, *J. Phys. Chem.*, 1990, 94, 6517-6519.

[14] Meneses, C. T. *et al.*, *J. Synchrotron Rad.*, 2006, 13, 468-470.

[15] Tassell, C *et al.*, *Microelectron. J.*, 1979, 10, 35-44.

[16] F. Farges *et al.*, Phys, Rev. B, 1997, 56, 1809.

Contact

* Y. Poo-arporn, tel: +66-44-217040 ext 1478; yingyot@slri.or.th

BL3.2Ua/b summary of 2015 operation and development

H. Nakajima

Synchrotron Light Research Institute (Public Organization), 111 University Avenue, Muang District, Nakhon Ratchasima 30000, Thailand

Background

The first undulator beamline 3.2U at the Siam Photon Laboratory (SPL) in the Synchrotron Light Research Institute (SLRI: Public Organization) has been opened for general user service since Oct. 2010. The undulator beamline was designed for soft X-ray photoemission electron spectroscopy (PES: BL3.2Ua) and microscopy (PEEM: BL3.2Ub). A planer Halbach-type undulator (U60) was purchased from the Danfysik A/S (Denmark). The U60 control system was developed and magnetic fields varied with the undulator gap were measured at SPL. U60 was installed in the storage ring in 2009, and the optical beamline system was constructed in Jan, 2010 providing to the preliminary users' experiment as well as beamline commissioning. Two end-stations of PES and PEEM were connected to the two branches of the beamline in Apr, 2010. The major components of beamline 3.2U and PES system were transferred from the dismounted PES beamline 4 that had been utilized for the PES based on the bending magnet (BM) source at SPL. The optical mirrors and gratings were redesignrd for the undulator radiation to accommodate a low emittance and small beam size with higher and wider photon energy range than those in BM.

Specifications

The beamline provides the linearly polarized soft x-ray undulator radiation in the photon energy range between 40 and 1040 eV covered by three varied –line spacing gratings. The spot size is less than 1x1 mm^2 at both stations at XPS and PES, and flux is designed to achieve 1×10^{10} ph./s with a resolving power of 10,000. The end-station is designed to study the surface and interface electronic structures under the ultra-high vacuum condition.

Techniques

PES basically probes the electronic structures of materials in a way that soft X-ray excites electron and its energy and momentum distributions unlock a fundamental theory of materials. Angular distribution of photoelectrons emitted from crystals provides us hints how exotic material properties appear in the various semiconductors and magnetic materials. Electron energy distribution of photoelectrons emitted from the materials identifies what atomic elements and its chemical states trigger the phenomena in the catalysts or devices produced in the factory process.

Soft X-ray also enables us to analyze light atomic elements which cannot be accessed by hard X-ray absorption spectroscopy, and such elements play a crucial role in the organic as well as inorganic devices in the modern technology based on carbon, nitrogen, oxygen and so on. Soft X-ray absorption spectroscopy (XAS) probes the atomic structure and its chemical formation of materials in a way that soft X-ray excites electron and its interaction among the electrons surrounded as a function of photon energy depends on the atomic element and local structures of materials. PES and XAS are complementary, because PES analyzes the electronic structure based on the valence band (occupied state), while XAS based on the conduction band (un-occupied state).

Operation and service

In the fiscal year of 2015, we started the beam service with three beamline scientists, one assistant beamline scientist, one assistant researcher and one research assistant as local contact and operator. We provided the beam time as much as we can to share the experiences, train our staff members and find out the technical difficulties. The number of user projects (Thai, ASEAN and international) and their publications increases from those in the fiscal year of 2014, because the state-of-art instruments for the angle-resolved photoemission spectroscopy (ARPES) and bulk-sensitive total fluorescence yield (TFY) detector are opened for user service at BL3.2Ua.

International collaborations

Several international collaborations were successfully performed on the organic-semiconductor energy-level alignment (University of Malaya, Malaysia), multilayer-defect analysis (ESRF optic lab.), and sp^2/sp^3 ratio analysis on diamond-like carbon films (Nagaoka University of Technology) involved with a research internship student.

Development

In the fiscal years of 2016-2017, we promote the ARPES and XAS activities at BL3.2Ua by developing high-resolution ARPES with low (down to 20 K) and high (up to 1000 K) temperatures and fluorescence-yield XAS system compatible with UHV by the silicon drift detector (SDD) on low-concentration elements in insulating samples. The beam quality also has to be improved by removal of higher order lights and monitoring thermal effect on optical elements to reduce the photon energy drift. These development and improvement boost number of publications in high-impact scientific journals and expand the research capability on chemical and biological samples.
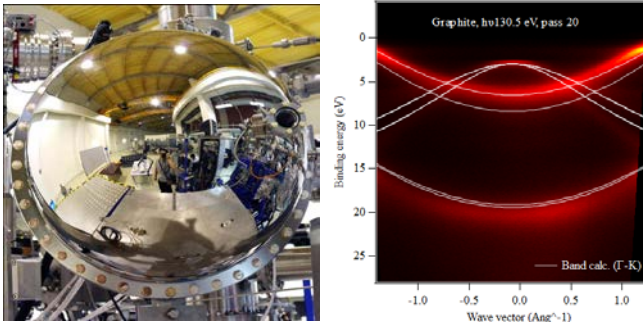
Figure 1: Left: VG Scienta R4000 analyzer for ARPES measurements. Right: Energy band structure on graphite measured at BL3.2Ua with band calculation.

Contact

*H. Nakajima, tel: +66-44-217040 ext 1482; hideki@slri.or.th

Synchrotron infra-red microspectroscopy at Siam Photon Laboratory

K. Thumanu[1]*, D. Srisamut[1], R. Supruangnet[1], P. Taraworakarn[1], M, Phanak[1], Su. Srichan[1],
W. Limphirat[1], Si. Srichan[1], P. Dumas[2], Y. Poo-arporn[1] and S. Tancharakorn[1]

[1]Synchrotron Light Research Institute (Public Organization), 111 University Avenue, Muang District, Nakhon Ratchasima 30000, Thailand
[2] SOLEIL Synchrotron, L' orme des Merisiers, BP48, 91192 Gif sur Yvette Ce´dex, France

Abstract

Fourier Transform Infrared (FTIR) spectroscopy has been widely used for a routine analytical technique. By combining spectroscopy with microscopy, the applicability of Fourier Transform IR Microspectroscopy (FTIRM) can be achieved to obtain molecular information at high spatial resolution. The infrared beamline (BL4.1: IR) was designed to collect both edge and bending magnet radiation (from the BL4.1) of the 1.2 GeV storage ring at the Siam Photon Source. The measurement of absorption spectrum and image can be covered the mid-infrared spectral range (4000-100 cm^{-1}). The coupling between synchrotron-IR, Bruker V70 FTIR spectrometer and a Hyperion 2000 IR microscope can be used to measure the samples with a high spatial resolution of 10x10 μm^2.

Infrared synchrotron radiation and advantages in microspectroscopy

Infrared microspectroscopy is widely used for chemical compound identification. Thanks to the high brightness of synchrotron radiation, synchrotron based infrared microspectroscopy can provide high spatial resolution, good signal to noise ratio (S/N) and short data acquisition time. The infrared beamline (BL4.1: IR) was designed to collect both edge and bending magnet radiation from the BL4 of the 1.2 GeV storage ring at the Siam Photon Source. The measurement of absorption spectrum and image can be covered the mid-infrared spectral range (4000 - 100 cm^{-1}). The coupling between synchrotron-IR, Bruker Vertex70 Fourier transform infrared spectrometer and a Hyperion 2000 IR microscope can be used to measure the samples with a spatial resolution of 10x10 μm^2 (Fig. 1).

Beamline layout
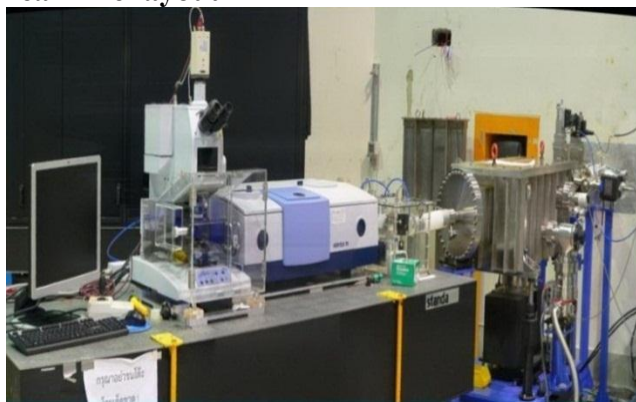
Figure 1: Schematic diagram of IR beamline.

The brightness advantage of synchrotron infrared (SR-IR) source is two to three orders of magnitude compared with conventional globar IR source. The high brightness of the synchrotron source allows small regions to be detected with high acceptable S/N. By using SR-IR source, the improvement in spatial resolution has allowed to apply this technique for many applications in particular to biological and biomedical samples. Typically, an aperture setting of conventional IR source is 20-100 μm. Conversely, because of a small effective source size of the SR, SR-IR can be transmitted > 80 % SR-IR pass through a 10 μm aperture. With conventional globar IR source, there is a tiny detectable signal with an aperture of 10x10 um. This illustrates that a small effective source size of SR-IR can produce high S/N ratio at a samples with a very small aperture. (Fig. 2 and Fig. 3)
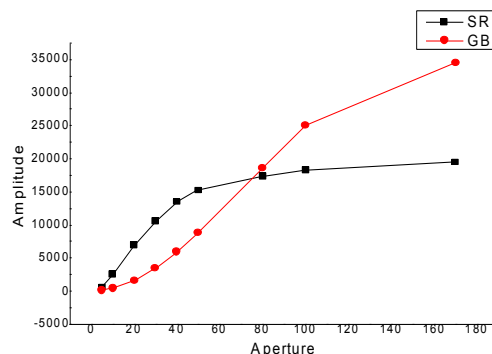
Figure 2: An intensity plot of IR signal as a function of aperture size of SR-IR and conventional Globar source. The measurement was performed using 15x IR Objective lens in transmission mode.
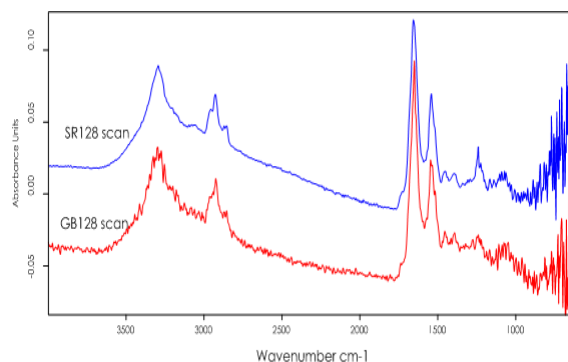
Figure 3: Comparison of IR absorbance spectra of tissue samples collected with a SR-IR (blue line) and Globar IR source (red color) at 5x5 μm aperture size, 4 cm^{-1} resolution, 128 scans.

Synchrotron IR microscopy and applications in biomedical science and agricultural science

Molecular fingerprint in the mid infrared region are derived from individual chemical bond, relating to structure and conformation. Absorbance bands of biochemical-cell fingerprint contain absorbance intensity peaks corresponding to different chemical bonds. The high brightness of the synchrotron source allows small regions to be detected with high acceptable S/N. By using SR-IR source, the improvement in spatial resolution has allowed this technique for many application in particular to biological and biomedical samples (Fig. 4).
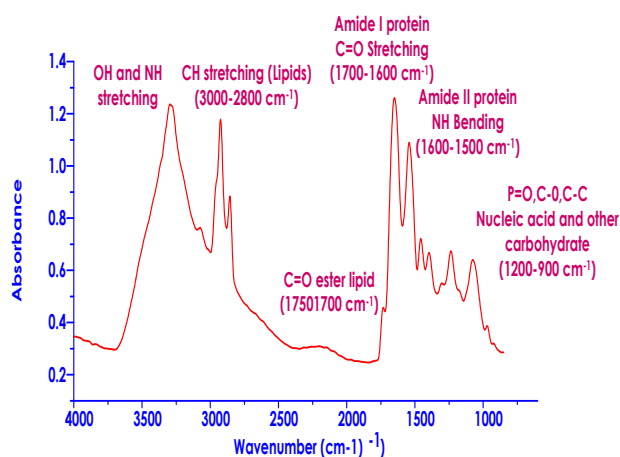
Figure 4: Typical Infrared spectrum of biological sample.
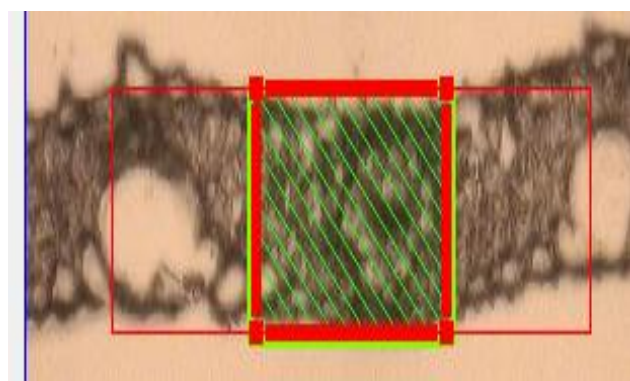
a)
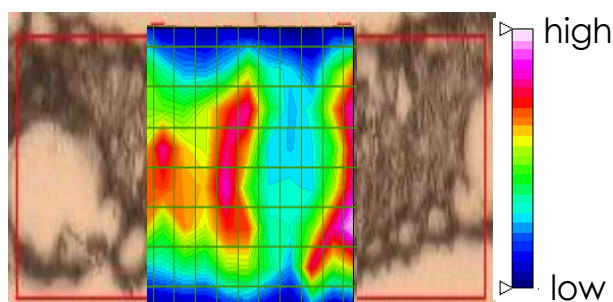
b)
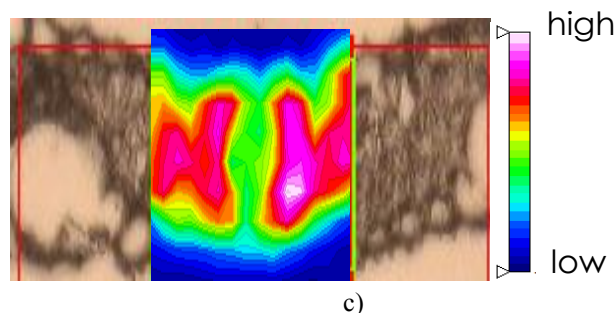
c)

Figure 5: Molecular functional group image of the leaf tissue compared between SR-IR mapping and Focal Plane Array Imaging (64 scans, 4cm^{-1}). (a) Visual image of leaf cross section (b) Chemical image of leaf section measured by SR-IR mapping. (c) Chemical image of leaf section measured by FPA-IR imaging. FTIR microscope coupled with FPA detector (64x64 element array detector) at 64 scan, 4 cm^{-1} resolution. Each of the images used to construct 4x4 binning FTIR image mosaic. Chemical image based on functional groups map obtained from Amide I protein (1700-1600 cm^{-1}). The color coded has been used to indicate absorbance, with the high absorbance (pink color) and the lowest absorbance (blue color)

Because of the brightness of SR-IR source, the image contrast of SR-IR technique gives a better results in terms of higher S/N and improve spatial resolution. Based SR-IR microspectroscopy is much brighter than conventional source, allowing good S/N ratio at very small aperture. Therefore a spectral changes of the leaf tissue can be used to distinguish the biochemical composition of the leaf (the epidermis, the vascular bundle, the mesophyll). However, synchrotron based measurement have a main barrier due to the fact that data can be acquired point by point spectra acquisition. It would require several hours to complete spectral mapping of the leaf cross section, while IR microspectroscopy with FPA could take only a few minutes.(Fig. 5).

Spectra from SR-IR mapping were collected with a square aperture of 10×10 μm in transmission mode.

The high spatial resolution of SR-IR microspectroscopy permits the sub cellular chemical mapping of rice seed cross section giving information absorbance varying concentrations of biochemical composition such as protein (1700-1600 cm^{-1}), carbohydrate (1200-900 cm^{-1}), lignin and pectin (1750-1700 cm^{-1}) in the aleurone layer and endosperm. The basic information on the globar composition (carbohydrate, lipid, lignin, pectin and protein) can be provided, together with the structural information on cell wall composition. (Fig. 6).

Future development

It is obvious that synchrotron radiation provide a high brightness source which is successfully exploited the advantage of synchrotron. The improvement are being

approved to align the infrared beam for using different mode of measurement such as transmission, transflection, attenuated total reflection (ATR) and gracing incidence (GI) modes which will be very useful for many applications e.g. material science, polymer science, environmental science.

a)   b)
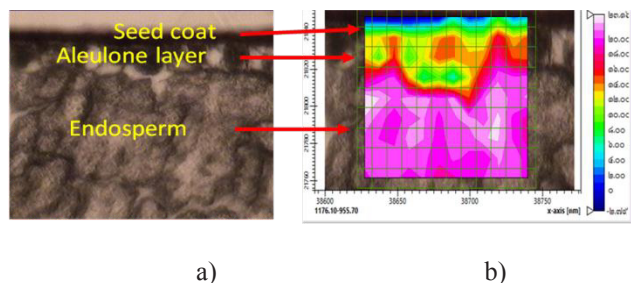
Figure 6: (a) A micrograph of the rice seed tissue (b) Chemical mapping of the rice seed cross section achieved using SR-IR microspectroscopy measured by point by point mapping with aperture setting at 10x10 μm aperture. Chemical image based on functional groups map obtained from carbohydrate region (1200-900 cm^{-1}). The color coded has been used to indicate absorbance, with the high absorbance (pink color) and the lowest absorbance (blue color).

References

[1] E. Levenson *et al*., Spatial resolution limits for synchrotron-based spectromicroscopy in the mid- and near-infrared, *J. Synchrotron Rad*. 2008, 15, 323–328.

[2] G. L. Carr, Resolution limits for infrared micro spectroscopy explored with synchrotron radiation, *Rev. Sci. Instrum*, 2001, 72(3), 1613-1619.

[3] L. M. Miller *et al*., Chemical imaging of biological tissue with synchrotron infrared light, *Biochimica et Biophysica Acta-Biomembranes*, 2006, 1758(7), 846–857.

Contact

*K. Thumanu, tel: +66-44-217040 ext 1487 ; kanjanat@slri.or.th

Current status of BL5.2: SUT-NANOTEC-SLRI XAS beamline

S. Mahakot, S. Rodporn, D. Kaewsuwan and P. Kidkhunthod[*]

Synchrotron Light Research Institute (Public Organization), 111 University Avenue, Muang District, Nakhon Ratchasima 30000, Thailand

Abstract

SUT-NANOTEC-SLRI beamline (beamline 5.2) is a flagship equipment of the *SUT-NANOTEC-SLRI Joint Research Facility for Synchrotron Utilization* - co - established by Suranaree University of Technology (SUT), National Nanotechnology Center (NANOTEC), and Synchrotron Light Research Institute (SLRI). It is an intermediate-energy X-ray Absorption Spectroscopy (XAS) beamline at SLRI. Beamline 5.2 delivers an unfocused, monochromatic X-ray beam of tunable photon energy (1.25 keV to 10 keV). The maximum, normal incident beam size is 13 mm (width) $\times$ 1 mm (height) with photon flux (10^8 to 10^{10} phs/s/100mA) varying across photon energies. The details of the beamline and XAS-supported instrumentation including *in-situ* XAS heating cell are described.

Introduction

Beamline 5.2: X-ray Absorption Spectroscopy (XAS) is a flagship beamline which is constructed under the SUT-NANOTEC-SLRI Joint Research Facility project. This beamline facility is aimed for synchrotron-based XAS research in which the XAS beam time will be equally allocated to each partner for all service beam time.

Typically, X-ray absorption technique is used to study structure of the matter in atomic scale. It can be used to determine chemical speciation and local structure of the absorbing atom (bond length, type of neighboring atom). Moreover, XAS is a non-destructive tool and can be employed to study in various scientific areas, such as materials science, biology, environmental science, and archeology. Additonally, this technique can be carried out on any type of materials, e.g. solid, liquid, and gas.

Beamline information

Figure 1: Current BL5.2 SUT-NANOTEC–SLRI XAS beamline setup.

The technical information of this beamline is shown in Table 1. The edge energy ranges between Mg K-edge and Ga K-edge (depending on Ga concentration in sample) are available to collect the XAS spectra at this beamline. The edge elements which can be measured, examples of XAS spectra and all equipments are shown in Fig. 2. Furthermore, *in-situ* equipments such as XAS heating cells (Fig. 4) for both transmission mode and fluorescence mode with the reduction and oxidation gas systems H_2, O_2, and N_2 (Fig. 5) are also available for the users.

Table 1: The technical information of BL5.2 SUT-NANOTEC–SLRI XAS beamline

Energy range	1240 – 12100 eV
Beam size at the sample	- 13 mm (width) x 1 mm (height) for transmission mode - 20 mm (width) x 1 mm (height) for fluorescence mode
Flux	$10^8 – 10^{10}$ photons/sec/100 mA
Energy resolution	2×10^{-4} / light energy
Experimental setup	- Transmission mode with ion chamber - Fluorescence mode with 4-element silicon detector

Crystal type	KTP (011) : 2d spacing = 10.955
	    : energy range = 1250 – 4780 eV
	InSb (111) : 2d spacing = 7.481
	    : energy range = 1830 – 7000 eV
	Ge (220) : 2d spacing = 7.481
	    : energy range = 3440 –12100 eV

Figure 2: The edge elements which can be measured at BL 5.2.

Example of the XAS spectra collected at BL5.2 for Mg K-edge, S K-edge and Ti K-edge are also shown in Fig. 3 (a) - 3(c), respectively.
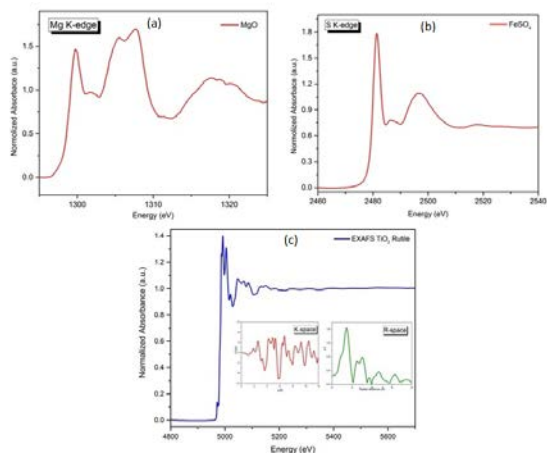

Figure 3: (a) - (c) :
- (a) The Mg K-edge XANES data of MgO sample acquired by KTP (011) crystal
- (b) The S K-edge XANES data of $FeSO_4$ sample acquired by InSb (111) crystal
- (c) The Ti K-edge EXAFS data of TiO_2 rutile sample acquired by Ge (220) crystal. Converted spectral function of the wavenumber (K - space) and flourier transform (R- space) for analyze atomic structure and local structure of the absorbing atom.
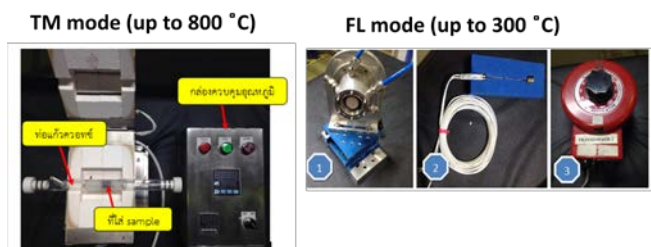
Figure 4: In-situ XAS heating cells for both transmission mode (left) and fluorescence mode (right).

Figure 5: The gas systems for reduction and oxidation XAS experiments.

Acknowledgement

References

[1] W. Klysubun *et. al*., SUT-Nanotec-SLRI Beamline for X-ray absorption fine structure spectroscopy, *J. of Synchrotron Radiation.*, 2017, 24(3), 707-716.

Contact

* P. Kidkhunthod, tel: +66-44-217040 ext 1406, 1662; pinit@slri.or.th

Fabrication of microstructures using X-ray lithography

R. Phatthanakun*, and W. Pummara

Synchrotron Light Research Institute (Public Organization), 111 University Avenue, Muang District, Nakhon Ratchasima 30000, Thailand

Abstract

This paper presents a fabrication process of microstructures using standard X-ray lithography at beamline 6a/b at Synchrotron Light Research Institute (Public Organization). High aspect ratio microstructures made of photoresist can be constructed on a substrate with a direct X-ray lithography which provides vertical sidewall for high precision microparts. These microparts can be applied in mechanisms of watches, high precision micromotors as well as micromolding systems. Moreover, the X-ray lithography offers a reproduction process of X-ray LIGA which has been widely used in batch fabrication of metallic microparts. The key geometric dimensional changes throughout the process were less than 1% which obviously confirmed the reliability of the reproduction using X-ray LIGA technology.

Introduction

Micromachining technology has been growing rapidly based on requirement of human life, especially for electronic instrumentation and technology. The mechanism inside them is microstructures which are assembled together in a unit to provide various multifunctions. The dimension of microstructures has been decreased to correspond with complex mechanical system. They have to be quickly fabricated with high precision in low-cost mass production which can be both plastic and metal. Nowadays, there are 5 methods which have been used to fabricate microstructures or microparts feed into the market. First is mechanical method which is always performed with high speed rotation of a bit and controlled by computer numerical control (CNC) system in multiple axes. This method can be used to support 3D structure based on programming design. Second is laser machining which works with a high-power laser at the material to be cut, resulting in melting, burning, vaporizing away or blowing of material. Third is electro-discharge-machining (EDM) which uses very small electrode applied by high voltage to remove material with sparking between electrodes. Both of them, EDM electrode and material, are electrodes which are separated by dielectric liquid. Fourth is water jet which uses a very high-pressure jet of water or a mixture of water and an abrasive substance to cut a wide variety of materials. Waterjet cutting is often used to fabricate microparts when the materials are sensitive to the high temperatures generated by other methods. Finally is photolithography or optical lithography which uses light to transfer a geometric pattern from a photomask to a photoresist on a substrate. After chemical treatment, the pattern of microparts is developed and can be used to form metallic microparts using electroforming method.

However, most of micromachining methods except photolithography destroy material during fabrication which

encounter with the limitation of material physics, especially for stress and phase changing in material. Therefore, the smallest dimension which can be performed by EDM, the best of SARIX micromachining, is 20 micrometers with a high precision of 2 micrometers. For photolithography, this is different from other methods because it is based on integrated circuit fabrication which the microstructures are grown on a wafer substrate instead of cutting them. Photoresist is a key material which absorbs the light energy pass through the pattern of photomask, resulting in soluble or insoluble in the photoresist developer. At the present time, there are 5 techniques of photolithography generally used to create microstructures as shown in Table 1 [1].

Table 1: Comparison of photolithography techniques [1]

| Technique	Potential sub-100 nm capability	Needs mask	Facility availability	production capability	3D capability
General Photo-lithography	Possibly	Yes	Widespread use in industry	Yes	No
UV lithography	Yes: depend on mask	Yes	Scare	Yes	Yes
X-ray lithography	Yes: depend on mask	Yes	Scare and expensive	Yes	Yes
Electron beam writing	Yes	No	Medium availability	No	No
High energy ion beam	Yes	No	Very scare	No	Yes

Table 1 is a comparison of photolithography techniques which have been used in both of research and industrial sections. Based on the requirement of industrial fabrication of micropart which need high volume production capability with low-cost fabrication, the three first techniques can be used. However, the specification of high-precision micropart considers working with high-aspect-ratio microstructure which is very important in comparing with other micromachining method. Although general photolithography and UV lithography are basic techniques and widely used in industry, vertical sidewall structure is very difficult to achieve from these methods. Therefore, X-ray lithography is the only one technique which can be used to support high precision microstructures. The accuracy of patterns is defined by photomask written at the maximum precision at sub-micrometer. However, X-ray lithography is not appropriate for low cost mass production because it is limited by synchrotron radiation source. To overcome this limitation, a process of rapid replication using metallic micromold fabricated by X-ray lithography combine with electroplating has been proposed in LIGA process [2].

This paper presents microparts fabrication method which based on X-ray lithography process from synchrotron light. High intensity of X-ray beam creates vertical sidewall microstructures based on batch fabrication and applied to

reproduce microparts using LIGA technology. The key geometric dimensional changes throughout the process were less than 1% which obviously confirmed the reliability of the reproduction using X-ray LIGA technology. The proposed method offers the rapid replication of micromolds and microparts in low-cost mass production.

X-ray lithography beamline

Fig. 1(a) shows beamline 6a: Deep X-ray lithography (DXL) for micropart fabrication which comprises of 3 parts. First is electron storage ring which is used to keep the electron bunches inside the ring at 1.2 GeV and bent them with electromagnetic field at bending magnet (BM). The high energy electron bunches were forced to travel in a curve path, resulting in synchrotron radiation emission along the BM. Synchrotron light has a property of broad spectrum which covers from infrared (IR) to X-ray. To bring synchrotron light to the end station or exposure area, a vacuum duct was connected to the BM and beryllium (Be) filter was attached to select X-ray radiation pass to exposure area. The end of vacuum duct was connected to vacuum chamber at the end station as shown in Fig. 1(b). At exposure area, the sample or photoresist was attached on an X-ray scanner and controlled by computer system as shown in Fig. 2.
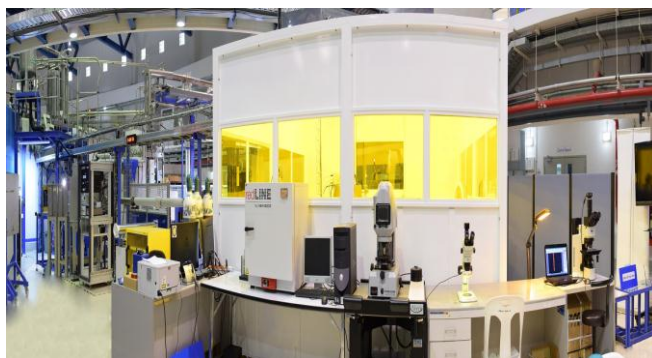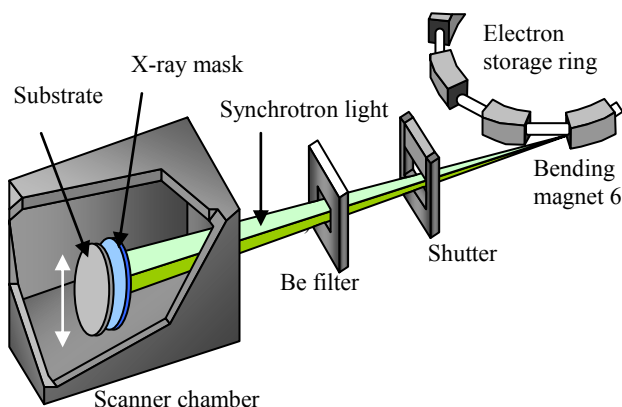

(a)

Figure 1: (a) Schematic of an X-ray beamline attached to an electron ring and (b) BL6a: DXL at SLRI
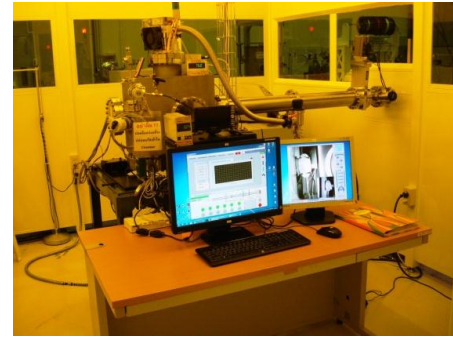
Figure 2: X-ray exposure control system

X-ray lithography and X-ray LIGA

X-ray LIGA is the German acronym for the replication process which consists of X-ray lithography (X-ray lithograpie), electroplating (galvanoformung), and molding (abformung). Fig. 3 demonstrates the basic LIGA process which starts by X-ray exposure onto thick photoresist film as shown in Fig. 3(a). After development to arrive at three-dimensional photoresist structure as shown in Fig. 3(b), the metal is subsequently filled by electroforming as shown in Fig. 3(c). Photoresist is then removed, resulting in freestanding metallic microstructures as shown in Fig. 3(d). Output of this step can be both microparts and micromold insert which are employed as a master mold in rapid replication process of hot embossing, injection molding [3], and polymer casting.

Figure 3: X-ray LIGA fabrication process.

Metallic microparts fabrication using X-ray LIGA

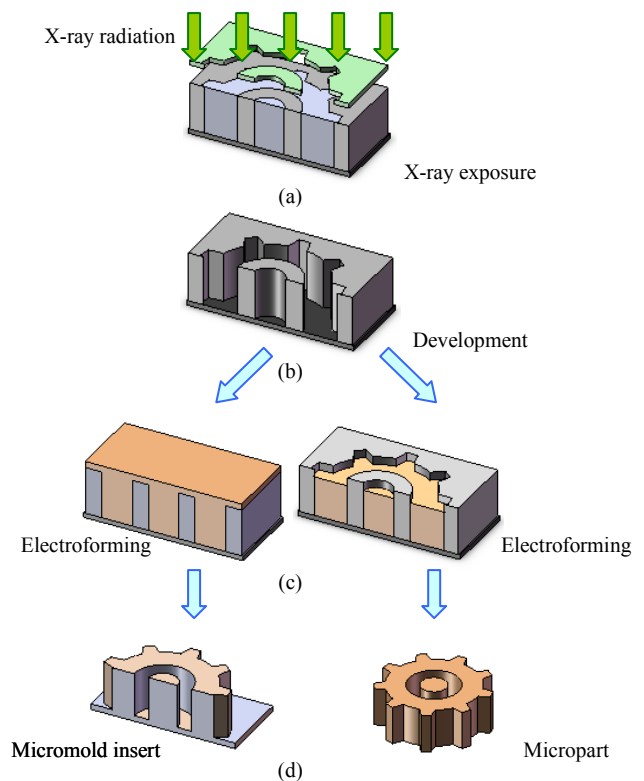The basic process of X-ray lithography is slightly different from other photolithography techniques because X-ray radiation can pass through thin membrane and absorb inside material as shown in Fig. 4. To define exposure patterns into photoresist, X-ray mask which consists of absorber pattern, pattern carrier, and handle ring as shown in Fig. 5 was placed in front of photoresist during X-ray exposure. Material with low atomic number and low densities such as graphite and Mylar (PET) were used to make X-ray mask membrane. For the absorber pattern, the material must efficiently absorb X-ray irradiation to provide image contrast on the photoresist. Materials with high atomic number and high density such as gold (Au) and silver (Ag) were employed in this role [4].
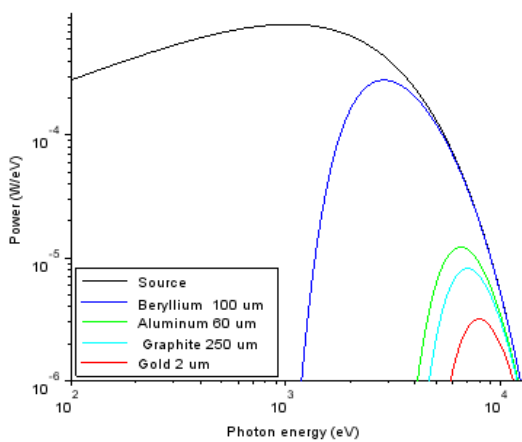

Figure 4: Radiation spectrum at the beam energy of 1.2 GeV.
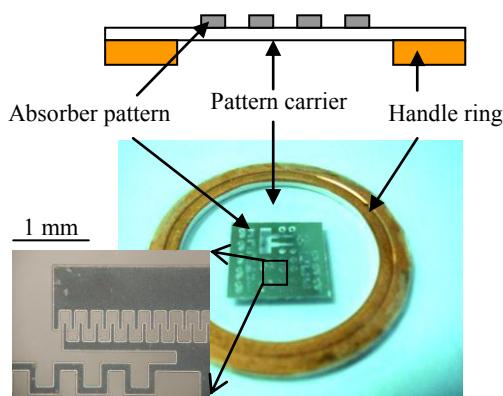

Figure 5: Components of X-ray mask.

After X-ray exposure, a sample coated with photoresist was chemical-treated in development process to remove unexposure area from substrate, leaving exposure area as high aspect ratio microstructures as shown in Fig. 6(a). In case of metallic microparts, photoresist was exposed and developed as micromolds for metal filling using electroforming as shown in Fig. 6(b) Overplated metals were then polished to obtain the final thickness as shown in Fig. 6(c). Photoresist molds were next respectively removed by chemical treatment and plasma

etching, leaving metallic microparts on the substrate as shown in Fig. 6(d). Finally, metallic microparts were released from the substrate as shown in Fig. 6(e).
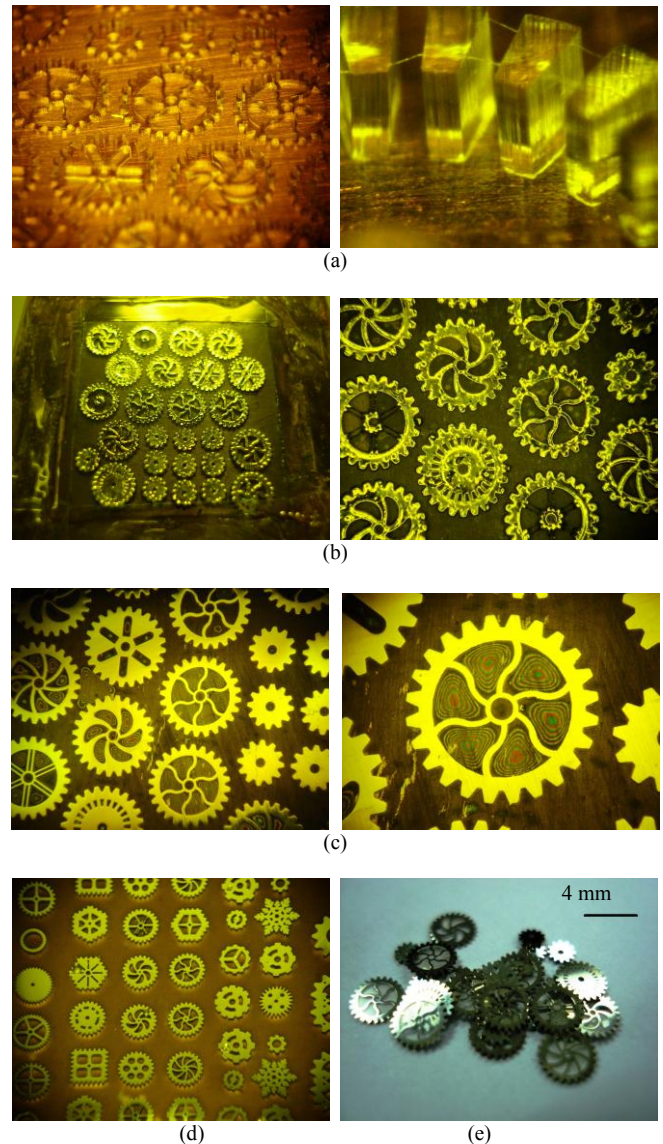
Figure 6: Fabrication sequences of metallic microparts.

The metallic microparts were measured the key geometric dimensions for 5 positions by using the Olympus Stream Digital Image Solutions as shown in Fig. 7. The key geometric dimensional changes throughout the process were less than 1% which obviously confirmed the reliability of X-ray LIGA technology. Furthermore, X-ray LIGA can be applied in creation of other metallic materials such as copper, silver, and gold based on electroforming process as shown in Fig. 8. In case of complicated microstructures such as multilayer microparts, X-ray lithography with multi-coating photoresist can offer 3 layers microstructures by multiple X-ray exposure as shown in Fig. 9. To create these complicated structures, they require 3 X-ray masks for exposure and development.

Figure 7: Photomicrographs of key geometric dimensions of metallic microgear.

(a)   (b)

Figure 8: Metallic microparts (a) copper and (b) silver.

Figure 9: Complicated 3 layers microstructures.

However, X-ray lithography cannot be used to support free form structure because synchrotron light passes directly into photoresist with a very small divergence. To improve this technique as much as possible, multi-axis X-ray exposure could be applied on scanner by controlling of exposure angle and rotation speed during scanning.

Conclusion

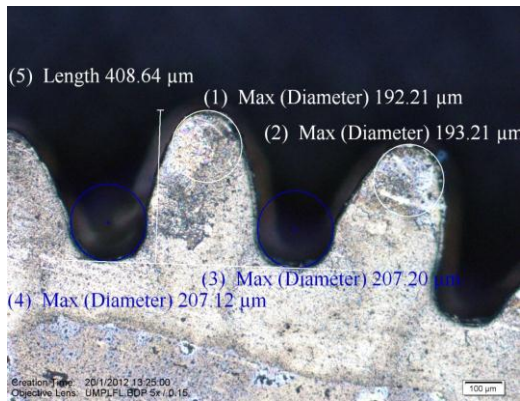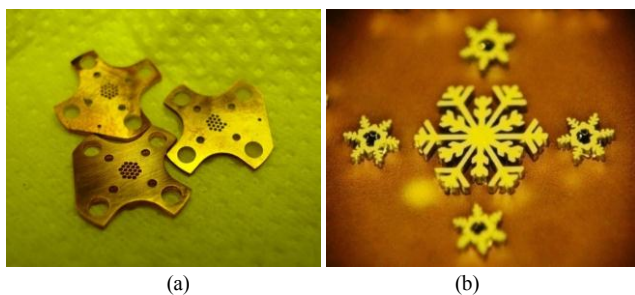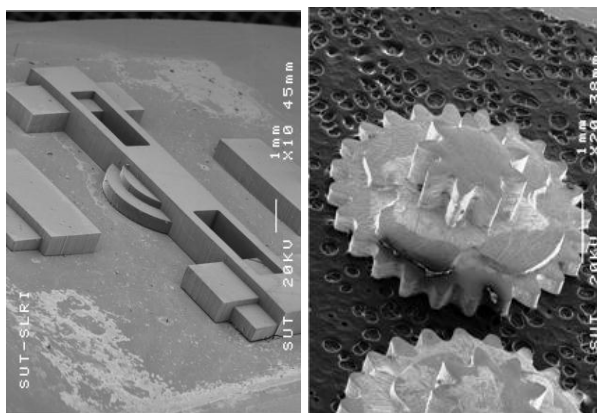X-ray radiation from synchrotron light was applied to create high precision microstructures based on photolithography process. The key material was photoresist which interacted with X-ray radiation and formed itself as structures after chemical treatment. By controlling of exposure energy and thickness, microparts made of photoresist could be easily fabricated using direct X-ray lithography. In case of metallic microparts, photoresist was exposed to form as micromolds and filled with desired metals by electroforming method. Complicated microstructures, moreover, can be constructed by multi-coating and X-ray exposure through X-ray masks. The key geometric dimensional changes throughout the process were less than 1% which obviously confirmed the reliability of the reproduction using X-ray LIGA technology. The proposed method offers the rapid replication of micromolds and microparts in low-cost mass production.

Acknowledgement

References

[1] F. Munnik *et al*., *Microelectronic Engineering*, 2003, 67-68, 96-103.

[2] K. Kim *et al*., Rapid replication of polymeric and metallic high aspect ratio microstructures using PDMS and LIGA technology, *Microsystem technologies*, 2002, 9, 5-10.

[3] M.T. Gale *et al*., Replication technology for optical microsystems, *Optics and Lasers in Engineering*, 2005, 43, 373-386.

[4] Y. Desta *et al*., X-ray Mask for LIGA Micro fabrication" *in Advanced Micro & Nanosystems* Volume 7 LIGA and its applications, ed. V. Saile, U. Wallrabe, O. Tabata and J.G. Korvink, (the Federal Republic of Germany, 2009, 11-50.

Contact

R. Phatthanakun; tel: +66-44-217040 ext. 1410; rungrueang@slri.or.th

Synchrotron micro X-ray Fluorescence (μ-XRF) spectroscopy and imaging beamline (BL6a/b) at Siam Photon Laboratory

J. Chaiprapa, N, Jearanaikoon, A. Chubkhuntod, J. Pradabsri and S. Tancharakorn[1]

Synchrotron Light Research Institute (Public Organization), 111 University Avenue, Muang District, Nakhon Ratchasima 30000, Thailand

Abstract

Synchrotron micro X-ray fluorescence (μ-SXRF) beamline, BL6a/b, is dedicated to the microscopic analysis of elements in microscopic scale of specimens as well as the study of the elemental distributions in tiny specimens. The BL6a/b utilizes synchrotron radiation source produced by a 1.4 T bending magnet of the 1.2 GeV electron storage ring. The microbeam is obtained by using polycapillary half-lens to focus a few-millimeter-sized polychromatic X-ray beam, with the energy range of 2-10 keV. The typical achievable beam-size is approximately 30 μm in the horizontal and vertical directions. Here, an up-to-date μ-SXRF user end-station and corresponding performance on this equipment setup are reported.

Introduction

During the last decade, several microscopic analytical methods such as secondary ion microscopy and imaging (SIMS), X-ray photoelectron spectroscopy (XPS), micro-Auger microscopy, micro-proton induced x-ray emission (μ-PIXE), laser ablation inductively coupled plasma mass spectrometry (LA-ICP-MS) and micro X-ray fluorescence analysis (μ-XRF)] have been developed to study the elemental distributions in small specimens. μ-XRF is probably regarded as a user-friendly analytical technique because most of samples can be examined with little or no pre-treatment and it is also regarded as a non destructive method for the elemental analysis of valuable specimens such as ancient objects. In addition, the interaction of X-rays with matter that causes the emission of fluorescent X-rays is completely understood and supported by high-quality physical data. Energy-dispersive X-ray fluorescence also provides a rapid analysis of multi-element detection in both qualitative and quantitative approaches. The increasing number of the certified or standard reference materials help researchers quantify the amount of elements in studied materials even more conveniently for macroscopic 'bulk' measurements as well as a microscopic analysis. Hence, μ-XRF is commonly used in a wide range of e.g. geology [1], materials science [2,3], environmental science [4,5], plants and agriculture [6,7], medicine [8,9], archaeology [10,11].

With the versatility of X-ray fluorescence technique, the synchrotron micro X-ray fluorescence (μ-SXRF) spectroscopy and imaging beamline, BL6a/b, was established in 2012 and dedicated to the microscopic analysis of elements in microscopic scale of specimens as well as the study of the elemental distributions in small specimens. The availability and accessibility of this analytical tool that SLRI opens for all users allow ones to

extend the scope of the study. In last few years, μ-SXRF user end-station have been developed to improve the capabilities of μ-SXRF as a method for qualitative and non-destructive elemental analysis of micro-heterogeneous materials. Here, the current status and capabilities of μ-SXRF beamline will be briefly reviewed.

μ-SXRF beamline layout

The beamline utilizes a synchrotron radiation source which is produced by a 1.4 T bending magnet of the 1.2 GeV electron storage ring. A beryllium window of thickness 100 μm is installed outside the radiation shielding wall. It is mainly used to separate ultrahigh- vacuum and low-vacuum regions in the beamline. The beryllium window also acts as a low-energy filter, leaving continuous X-rays of energy above 2 keV to reach the endstations. The fixed aperture reduces the beam size to 5 mm x 2 mm (H x V). Then, a polychromatic X-ray beam, so called white-beam X-rays, is delivered to the user end-station of either μ-SXRF or DXL experimental stations [12]. Fig. 1 shows the schematic layout of μ-XRF beamline, BL6a/b, where a μ-SXRF end-station sits upstream of the DXL end-station, and it is designed to be replaced by a 1 m-long vacuum pipe when the DXL end-station is in operation. Three gate valves are employed to maintain vacuum environments during the vacuum duct replacement.
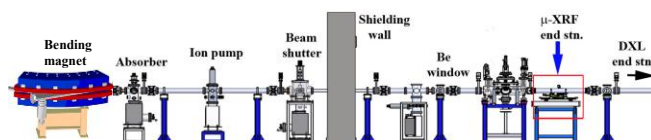
Figure 1: Schematic layout of theBL6a/b μ-SXRF beamline [12].

μ-SXRF user end-station

The μ-SXRF user end-station consists of four main components including an X-ray optical system, a vision system, a motorized sample holder with two degrees of freedom, and an energy-dispersive X-ray detection system, as shown in Fig. 2. To achieve a micro X-ray beam, a polycapillary half-lens manufactured by XOS company is exploited to focus a few millimeter-sized X-ray beam to 30μm in diameter. This polycapillary half-lens is mounted on motorized stages with four degrees of freedom. It is aligned using two translation stages with 6 μm precision and two rotary stages with 0.006° precision from MISUMI, Japan. A CCD camera with a 10x macro lens is also used to

specify and capture the measured area of a sample. In a raster scanof the sample, the high precisionmotorized stages with two degrees of freedom and 0.1 μm of precision are used to move the sample step by step in horizontal and vertical directions. These motorized stages are remotely controlled via computer. Detection of the X-ray fluorescence signal is via an energy-dispersive Vortex Si drift detector from Hitachi High-Technologies Science America, Inc., with the energy resolution of 139 eV at the Mn K emission line. Energy-out signals from the detector are then registered at XIA Digital Signal Processing Systems corresponding to the energy of X-rays.

Figure 2: The BL6a/bμ-SXRF user end-station.

Data acquisition and data analysis programs for μ-SXRF imaging

A data acquisition program using the LabVIEW platform has been developed by a control engineering workgroup at SLRI. It is not only used to acquire XRF data, but also to control the movements of the motorized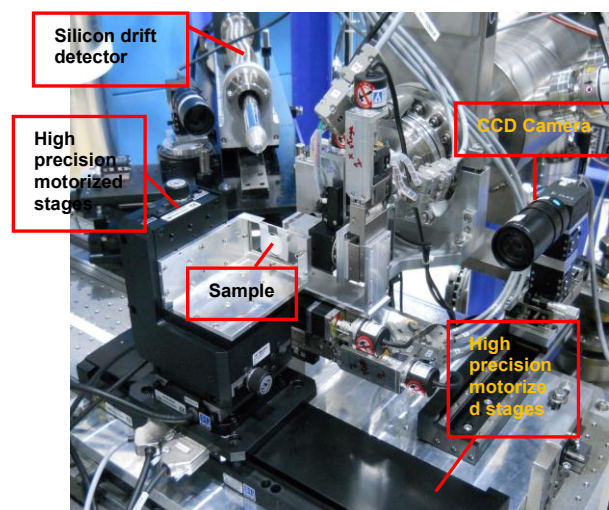 stages for raster scanning the sample during the measurement. When the measurement is completed, a series of one-column XRF data files is generated. These stack files are compatible with most standard XRF analysis programs. However, the ROI image tool program of the pyMCA package [13] is used here. An image showing elemental distribution can therefore be analyzed.

μ-SXRF performance and analysis

To study the uptake of nutrient in plants, beansprout is chosen as a model organism in plant agriculture. Beansprout seeds were soaked in deionized water for a day and then germinated in a wet tissue paper towel in a laboratory at 27 °C. Using appropriate volumes of Zn stock solutions (ZnSO4.6H$_2$O), plant-growth solutions were prepared with a concentration of 50 μM Zn. In experiments, approximately 2-day-old seedlings were grown in a petri dish of deionized water (control, no exposure) and two petri dishes of 50 μM Zn solution for 3 hr and 6 hr. The tip of roots were analyzed

at BL6a/b beamline, using micro X-ray Fluorescence (μ-XRF) spectroscopy and imaging technique. The map was produced in a step-scan mode and covers a 1.25 mm x 0.80 mm area in 50-μm step in horizontal and 30-μm step in vertical. The exposure time per pixel is 15 seconds. The energy-dispersive data were then analyzed using the ROI image tool program in pyMCA. The distribution of Zn in the tip of roots can be imaged, using temperature colour map. The colors red, green and blue represent high, medium and low intensities, respectively.
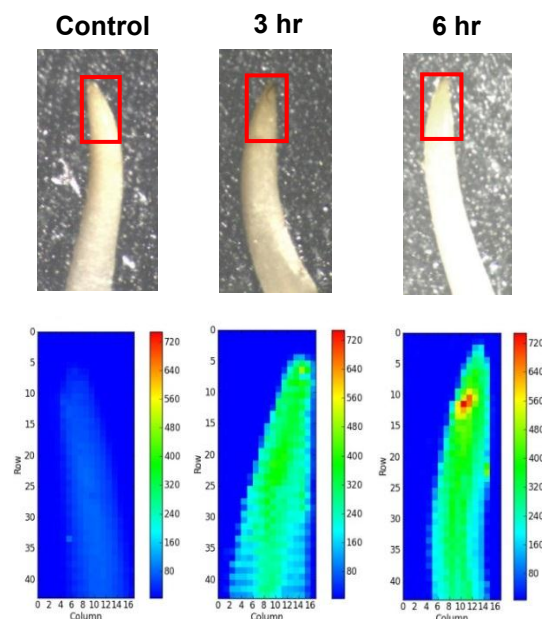
Figure 3: Roots of beansprouts grown in solutions containing 50 μM Zn for 0 min, 3he and 6hr (left to right) examined using μ-XRF technique.

Fig. 3 shows the results of the distribution of Zn in the tip of beansprout which are grown in deionized water (control) and in 50μM Zn solution for 3hr and 6hr. It is obvious that beansprouts which are grown in Zn solution gives significantly higher counts of Zn than that of the control one. 6hr-grown beansprout possess a bigger Zn-rich area when it is compared to that of 3hr-grown beansprout, that it makes sense of this examination of the nutrient uptake of the experiment of plant growth. However, there was a peculiarity in 6hr-grown beansprout; the highest Zn accumulated area is not located at the tip of root, but it is above the tip of root instead.

Conclusion

A μ-SXRF user end-station BL6a/b has been developed since 2012 to achieve a smaller micro X-ray beam. Using a new polycapillary half-lens to focus a few-millimeter-sized polychromatic X-ray beam yields a smaller micro X-ray beam of 30 μm at the sample position. The experiments of the nutrient uptake of the root of beansprout shows that the performance of new μ-XRF apparatus setup provides us a satisfactory result.

Future developments

A Si(111) crystal will be installed to obtain the monochromatic X-ray beam at BL6a/b end station. This will help users to perform quantitative analysis even more easily. In addition, it is planned to install a sample chamber, that the experiments will be conducted in vacuum or He-filled conditions. This will help us to probe light elements such as Mg, Al, P, etc. even better.

References

[1] S. Pongpiachan *et al*., Sedimentary Features of Tsunami Backwash Deposits as Assessed by Micro-Beam Synchrotron X-ray Fluorescence (μ-SXRF) at The Siam Photon Laboratory, *J. of Tsunami Society International*, 2013, 32(2), 96-115.

[2] E. Wieland *et al*., Micro-spectroscopic investigation of Al and S speciation in hardened cement paste, *Cement and Concrete Research*, 2010, 40, 885–891.

[3] C.H. Li *et al*., Synchrotron micro-XRF study of metal inclusions distribution and variation in fused silica induced by ultraviolet laser pulses, *Nuclear Instruments and Methods in Physics Research B*, 2010, 268, 1502–1507.

[4] A. Hokura *et al.*, Micro X-Ray Fluorescence Imaging and Micro X-Ray Absorption Spectroscopy of Cadmium Hyperaccumulating Plant, Arabidopsis halleri ssp. gemmifera, using High-Energy Synchrotron Radiation, *J. Anal.At.Spectrom*, 2008, 23, 1068-1075.

[5] T. Punshon *et al.*, Using synchrotron X-ray fluorescence microprobes in the study of metal homeostasis in plants, *Annals of Botany*, 2009, 103, 665–672.

[6] M. Nečemer *et al*., Application of X-ray fluorescence analytical techniques in phytoremediation and plant biology studies, *SpectrochimicaActa Part B*, 2008, 63, 1240–1247.

[7] L. Lu *et al.*, Speciation and localization of Zn in the hyperaccumulator Sedum alfredii by extended X-ray absorption fine structure and micro-X-ray fluorescence, *Plant Physiology and Biochemistry*, 2014, 84, 224-232.

[8] B. Pemmer *et al*., Spatial distribution of the trace elements zinc, strontium and lead in human bone tissue, *Bone*, 2013, 57, 184–193.

[9] W. Osterode *et al*., Iron, copper, zinc and bromine mapping in cirrhotic liver slices from patients with hemochromatosis studied by microscopic synchrotron radiation X-ray fluorescence analysis in continuous scanning mode, *SpectrochimicaActa Part B*, 2007, 62, 682–688.

[10] C. Lin *et al*., The study of chemical composition and elemental mappings of colored over-glaze porcelain fired in Qing Dynasty by micro-X-ray fluorescence, *Nuclear Instruments and Methods in Physics Research B*, 2011, 269, 239–243.

[11] B. Constantinescu *et al.*, Micro-SR-XRF studies for archaeological gold identification—the case of Carpathian gold and Romanian museal objects, *Appl Phys A*, 2010, 99, 383–389.

[12] S. Tancharakorn, *et al.*, The First microbeam synchrotron x-ray fluorescence beamline at the Siam Photon Laboratory, *J. Synchrotron Rad.*, 2012, 19**, 536.

[13] V. A.Sole *et al*., A multiplatform code for the analysis of energy-dispersive X-ray fluorescence spectra, Spectrochim. *Acta B*, 2007, 62, 63–68.

Contact

*J. Chaiprapa, tel: +66-44-217040; jitrin@slri.or.th

Commissioning of BL7.2W: macromolecular crystallography (MX) at Siam Photon Laboratory

C. Songsiriritthigul, M. Phanak, N. Mothong, J. Attarataya, N. Pramanpol,

N. Wongprachanukul, R. Supruangnet and Y. Poo-arporn

Synchrotron Light Research Institute Public Organization), 111 University Avenue, Muang District, Nakhon Ratchasima 30000, Thailand

Abstract

This work presents the commissioning results of BL7.2W: macromolecular crystallography (MX) at the 1.2 GeV Siam Photon Source of the Synchrotron Light Research Institute (SLRI), Thailand. The beamline is recently able to utilize hard X-rays at photon energy of 5 to 20 KeV from the 4.09 Tesla Superconducting Wavelength Shifter. The major beamline components include a cylindrical collimating mirror (CM), newly Kohzu's commercial double-crystal monochromator (DCM) and a toroidal focusing mirror (FM). Additionally, the experimental station of BL7.2W: MX fundamentally equipped with a MarDTB diffractometer and a MarCCD 165 mm detector. The measured photon flux of the monochromatic beam at 8.0 keV (1.55 Å) and 12.0 keV (1.03 Å) were 1.54×10^9 and 2.92×10^9 phs/s/100mA, respectively.

Introduction

The Siam Photon Source has operated at 1.2 GeV electron beam energy with the maximum electron current injected of 150 mA each operational cycle and its circumference of 81.26 m. Currently, there are three insertion devices (ID) installed in the storage ring which are a U60 permanent magnet planar undulator, 2.4 Tesla permanent magnet wiggler (PMW), and 4.09 Tesla superconducting wavelength shifter (SWLS). The 4.09 Tesla SWLS provided by National Synchrotron Radiation Research Center in Taiwan (NSRRC) has been inserted to produce higher energy X-rays for beamline 7.2W directly. The partial flux calculation for the 4.09 Tesla SWLS at photon energy of 8, 12 and 18 KeV with opening angle of 2.0 mrad (horizontal) x 0.42 mrad (vertical) is 5.75×10^{12}, 4.06×10^{12} and 2.05×10^{12} phs/s/100 mA respectively.
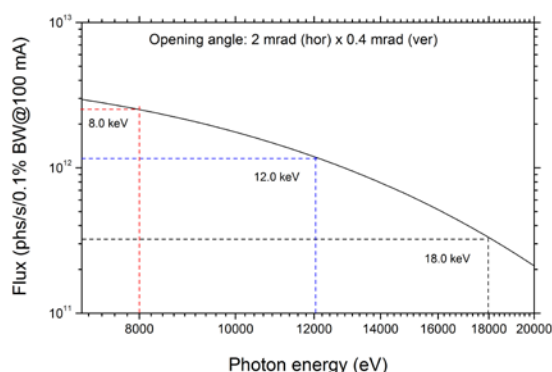

Figure 1: Calculated photon spectrum of synchrotron hard X-rays generated from a 4.09 Tesla superconducting wavelength shifter at 1.2 GeV.

The optical system for BL7.2W: MX

The schematic view of BL7.2W: MX is shown in Fig. 2 (a) and (b) as previously designed. The major optical elements to obtain a focused hard X-ray beam with a range of 5 to 20 KeV for diffraction experiments are a cylindrical collimating mirror (CM), double-crystal monochromator (DCM) and toroidal focusing mirror (FM) [1].

(a)
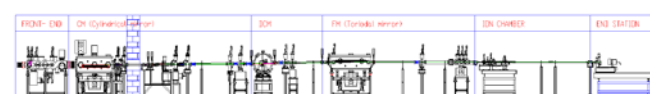
(b)
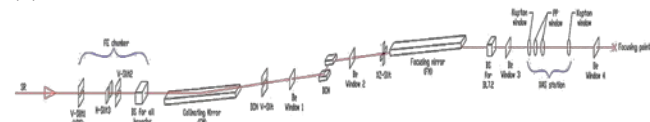
Figure 2: (a) Beamline layout of 7.2W: MX (b) Optical layout of 7.2W: MX

Mirrors

The mirrors have been inserted in the beamline which are a collimating mirror (CM) and focusing mirror (FM). The CM is a cylindrical mirror (R = 5,542,870 mm) coated with Rh/Pt and the grazing angle of 3.5 mrad to be used for collimating white beam. Next, the FM is a toroidal mirror (R = 5,714,297 mm) and ρ = 46.7 mm. From the meridional and sagittal focusing term, the angle of incidence falls into 89.799 degree or equivalent to the grazing angle of 3.5 mrad. The characterized specification of both of mirrors is as shown in the Table 1.

Table 1: Specification of CM and FM mirrors

Optical element	Shape	Optical coating	Radius of curvature (cm)		Surface roughness	Dimensions (L x W) cm²	Useful surface area (L x W) cm²
			Major	Minor			
CM	Cylindrical	Rh 50 Å/ Pt 250 Å	554287	-	< 3 Å	109 x 5.5	105 x 2.5
FM	Toroidal	Rh 50 Å/ Pt 250 Å	571430	4.67	< 3 Å	129 x 6.5	125 x 4.5

Double crystal monochromator (DCM)

The beamline had previously been located to utilize synchrotron light generated from a bending magnet, namely BL7.3. This allowed the in-house developed beamline component, double-crystal monochromator (DCM) which was fabricated based on the design from NSRRC facility [2]. We was earlier able to obtain good quality absorption spectra from this in-house DCM for transmission mode

X-ray absorption measurements; however, the noticeable problem on beam position from exit beam at horizontal position occurred. Thereafter, the beamline was relocated to BL7.2W which utilized hard X-rays directly from the 4.09 T SWLS instead for macromolecular crystallography technique that we first delivered focused monochromatic beam with fixed photon energy at 12.7 KeV in late 2014 from previous operation at 7 KeV photon energy.

With limitation of the in-house fabricated DCM in tunable photon energy for future improvement, the commercial DCM was purchased from Kohzu Co. Ltd.; model TSR-2DCM and the installation and commissioning of this DCM has recently performed in late October 2016. Study on X-ray absorption near edge structure (XANES) by the commercial DCM was as shown in XANES spectra at Co K-edge and Au L3-edge in Fig. 3(a) and (b) respectively.
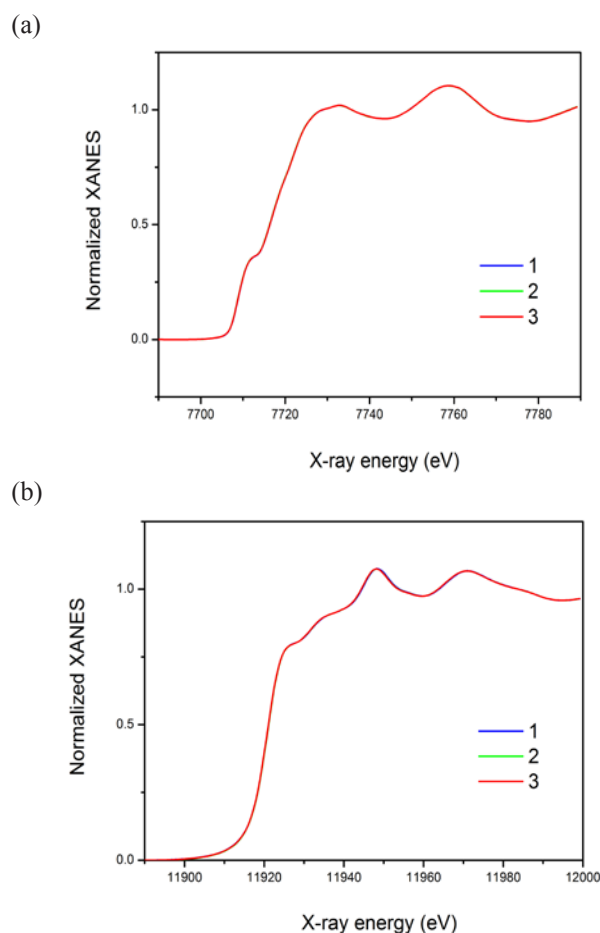
(a)

(b)

Figure 3: Reproducibility of XANES spectra from 3 successive scans at BL7.2W: MX (a) Co K-edge XANES spectra (b) Au L3-edge XANES spectra

Commissioning results and performance

In order to commissioning in beamline performance, the photon flux measurement was carried out at series of

different photon energy and the results are in the range of 109 phs/s/100 mA which the energy can be tunable within the range of 5 to 20 KeV

Table 2: Photon flux at beam size of 2 mm x 15 mm

Photon energy (eV)	Flux* (phs/s/100 mA)
7,000	1.18×10^9
8,000	1.54×10^9
12,000	2.92×10^9
18,000	4.17×10^9

Flux was calculated at sample position of XAS with Slit opening: 0.42 mrad (Vertical) and 2.0 mrad (Horizontal)

In the experimental station of BL7.2W: MX consists of a 165 mm-diameter MarDTB diffractometer with a 2θ offset up to 30 degree and an oxford cryostream 700 series with cooling temperature of 100K as well as a MarCCD program to collect diffraction data.

Table 3: Beamline and End station specification

Technique	Macromolecular crystallography
Source type	Superconducting wavelength shifter 4.09 Tesla
Ring Current	150 mA
Photon Energy	5-20 keV
Optic	Cylindrical Collimating Mirror (Rh/Pt coated) Fixed Exit Double Crystal Si(111) Monochromatoer Toroidal Focusing Mirror (Rh/Pt coated)
Beam divergence Beam size	2.0 mrad x 0.42 mrad at DCM 32.32 mm (h) x 4.09 mm (v) at DCM
Flux	2.92×10^9 phs/s/100 mA after FM @12 KeV
Goniometer	MarDTB Goniometer system
Xtal-detector Distance	45-390 mm
Detector	MarCCD® with 165mm in diameter
2θ Range	0-30º
Cryo-capability	Oxford cryostream 700 series (working temperature 100 K)
Softwares	iMOSFLM, CCP4

All raw diffraction frames and processed files are effectively stored in the institution's main server through user programs for X-ray data processing such as iMOSFLM and CCP4.

The standard proteins to be tested for full-dataset in the BL7.2W: MX are lysozyme and insulin crystals. The first protein structure to be successfully submitted in the Protein Data Bank is triosephosphate isomerase from *Leishmania siamensis* (PDB code 5CG7) [4]. Another protein crystal which also was collected here was C-terminal half of gelsolin with its reflection having I/σ(I) of 2.8 for highest resolution shell [5]. Crystallographic statistics of successful test crystals is shown in Table 4.

Table 4: Crystallographic data collection of test crystals

Test Sample	Lysozyme	Insulin	Triosephosphate isomerase from *Leishmania siamensis*	C-terminal half of Gelsolin
Space group	P4$_3$2$_1$2	I2$_1$3	C2	P2
Unit-cell parameters (Å)	a= b= 78.47, c= 37.22	a=b=c= 77.68	a= 81.44, b= 76.45, c= 94.94	a= 88.48, b= 84.95, c= 155.21
Unit-cell angles (°)	α = β = γ = 90	α = β = γ = 90	α = γ = 90, β = 101.14	α = γ = 90, β = 89.80
Exposure time (sec)	20	15	40	90
Resolution range (Å)	19.03–1.60 (1.69–1.60)	19.42–2.10 (2.21–2.10)	21.56–1.88 (1.98–1.88)	37.19–3.50 (3.69–3.50)
No. of unique reflections	15,634 (2,272)	4,686 (670)	46,171(6,233)	26,550 (3,498)
No. of observed reflections	110,922 (15,972)	50,864 (7,365)	130,363 (16,769)	86,573 (10,864)
Completeness (%)	98.8 (99.9)	99.9 (100)	98.6 (91.4)	90.4 (81.9)
Redundancy	7.1 (7.0)	10.9 (11.0)	2.8 (2.7)	3.3 (3.1)
< I/σ(I)>	20.8 (8.2)	18.8 (5.8)	9.8 (2.3)	6.0 (2.8)
R$_{merge}$†	5.8 (20.2)	10.5 (42.3)	7.7 (45.8)	18.8 (41.4)
Mosaicity (degree)	0.17	0.37	0.53	1.27

$$^{\dagger}R_{\mathrm{merge}} = \sum_{hkl}\sum_{i}\left|\mathrm{I}_i(hkl)-\langle\mathrm{I}(hkl)\rangle\right|\Big/\sum_{hkl}\sum_{i}\mathrm{I}_i(hkl)$$ where Ii is the intensity for the ith measurement of an equivalent reflection with indices *hkl*.
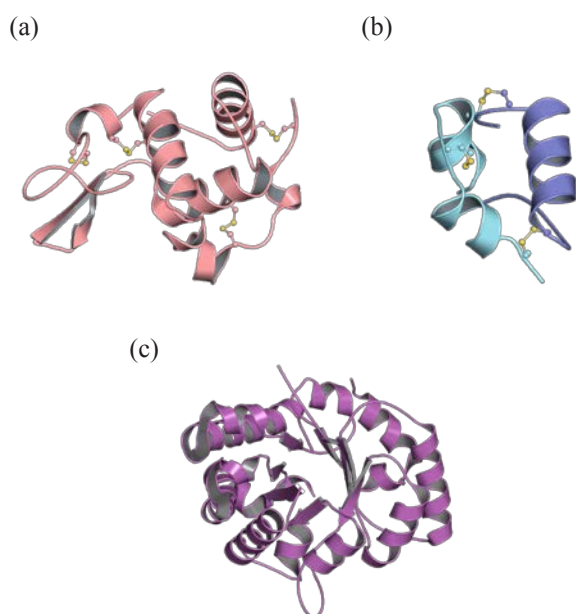
(a)   (b)

(c)

Figure 4: Crystal structures collected on the BL7.2W of the SLRI. (a) lysozyme (b) insulin and (c) triosephosphate isomerase from Leishmania siamensis (PDB code 5CG7).

Summary

The BL7.2W: MX delivers hard X-rays from a 4.09 T SWLS with selectable photon energy between 5 and 20 KeV under photon flux of 109 phs/s/100 mA and beam size of 32.32 mm (H) and 4.09 mm (V) right after Kohzu DCM. Test crystals of lysozyme and insulin were successfully collected at BL7.2W up to 1.6 and 2.1 Å respectively.

Future plan

According to advantages of the newly Kohzu DCM, there has recently been study on SAD experiment as well as improvement on the beamline components due to the change on wavelength shifter from recently 4.09 to 6.5 Tesla.

Acknowledgements

References

[1] W. Klysubun *et al.*, Development of a hard X-ray beamline for macromolecular crystallography at the Siam Photon Laboratory, *The Fifth Asia Oceania Forum for Synchrotron Radiation Research (AOFSRR2010)*, 2010.

[2] C. S. Hwang *et al.*, A low-cost and flexible double-crystal monochromator for an x-ray beamline, *Rev. Sci. Instrum.*, 1998, 69(3), 1230-1235.

[3] C. Songsiriritthigul *et al.*, Commissioning Results and Performance Test of an in-house-developed Double Crystal Monochromator at the Siam Photon Laboratory, *The 8th Annual Conference of the Thai Physics Society, Siam Physics Congress 2013*, 2013.

[4] B. Kuaprasert *et al.*, Preliminary crystallographic analysis of *Leishmania siamensis* triosephosphate isomerase complexed with its novel inhibitor, *J. Sci. Technol.*, 2015, 22(3), 285-293.

[5] S. Choknud *et al.*, The structural study of the C-terminal half of gelsolin, *The 10th international Symposium of the Protein Society of Thailand*, 2015, 167-172.

Contact

*C. Songsiriritthigul, tel: +66-44-217040 ext 1485; chomphunuch@slri.or.th

Improvment of beamline 8 performance in 2016

W. Klysubun, P. Tarawarakarn, P. Sombunchoo, S. Lapboonrueng,
W. Wongtepa, C. Cholsuk and P. Thamatkeng

Synchrotron Light Research Institute (Public Organization), 111 University Avenue, Muang District, Nakhon Ratchasima 30000, Thailand

Abstract

The paper reports improvement of beamline 8 at Synchrotron Light Research Institute (Thailand) completed in 2016. Installation and commissioning of an X-ray collimating mirror, during June to September 2016, has resulted in better experimental performance for X-ray absorption spectroscopy due to higher photon flux and higher cut-off energy. Experimental XANES and EXAFS spectra collected after this upgrade are presented.

Introduction

Since 2006, beamline 8 has been operated for X-ray absorption spectroscopy (XAS) to deliver an unfocused X-ray beam, from a bending magnet of the Siam Photon storage ring, to a XAS station. The photon energy of the beamline ranged from 1.25 keV to 10 keV [1]. The XAS station was capable of measuring XANES and EXAFS spectra in transmission mode and fluorescence-yield mode [2]. Photon energies were scanned by a double crystal monochromator (DCM) across an edge energy of interest. Entrance slits of DCM was used to cut off the X-ray beam that had vertical divergence larger than 125 µrad, thereby optimizing photon energy resolution for XAS experiments.

The average photon flux measured by an ionization chamber at the XAS station during users' experiments in 2015 is given in Table 1. Since the photon flux of 10^9 phs/s/100mA and higher normally provide good signal-to-noise ratio of a measured XAS spectrum, an increase of photon flux, especially for measurements at higher energies (> 8 keV) and/or on diluted samples, was proposed as a major development of beamline 8 in 2016.

Table 1: Average of photon flux of beamline 8 measured by an ionization chamber in 2015.

Element	Edge energy of native element (eV)	Photon flux (phs/s/100mA)
Aluminum	1559.6	8.4×10^9
Silicon	1839.0	4.6×10^{10}
Phosphorous	2145.5	5.6×10^{10}
Calcium	4038.5	1.4×10^{10}
Chromium	5989.0	6.7×10^9
Nickel	8333.0	2.2×10^9
Zinc	9659.0	7.8×10^8
Arsenic	11867.0	4.9×10^7

Installation and commissioning of an X-ray collimation mirror

An X-ray mirror, and two new X-ray beam diagnostic chambers were installed at beamline 8 during June-August 2016. The mirror is a bendable, flat, rhodium-coated silicon crystal. A radius of curvature of the mirror can be adjusted from 1.3 km to infinity by a motorized mechanical bender. Based on a ray tracing calculation by SHADOW [3], 1.8 km of the curvature radius is required, for the mirror installed at 4.5 m from the bending magnet source, to collimate the white X-ray beam at the glancing incident angle of 5 mrad.

Fig. 1 shows the mirror installed in the mechanic bender with water-cooled copper bars attached on each side of the mirror. The mirror-bender assembly is sited on standard cone, v, and flat kinematic mounts driven by 3 vertical motorized stages and 2 horizontal motorized stages in order to align the mirror to the synchrotron X-ray beam. Fig. 2 shows removal of front-end and downstream vacuum components of beamline 8, followed by the installation of the X-ray mirror chamber, and two new X-ray beam diagnostic chambers. The mirror and auxiliary components (horizontal slits, vertical slits, fluorescence screens, and scanning wires) were accurately installed on the optical axis of the beamline with ±50 micron alignment precision.
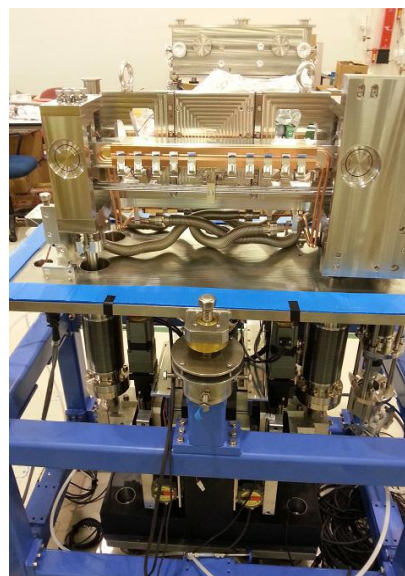
Figure 1: X-ray collimating mirror of beamline 8. The mirror and bender were manufactured by Crystal Scientific (UK), Ltd. and Toyama Co., Ltd., respectively. A vacuum chamber and kinematic mounts were fabricated by SLRI.

The mirror orientation and its curvature were carefully adjusted during commissioning with the synchrotron beam. Once the beam was collimated with vertical divergence smaller than 125 µrad, it is not necessary to use the entrance slits of the DCM. The DCM crystals and XAS station were optically aligned to obtain maximum photon intensity incident on a transmission sample or fluorescent sample. It

was observed that the photon energy resolution is dependent on slope error of the mirror curvature.

Figure 2: Removal of front-end and downstream components of Beamline 8 (upper panels); installation of a new front-end beam diagnostic chamber, collimating mirror chamber, and a downstream beam diagnostic chamber (lower panels).

Improved performance for XAS

Table 2 reports photon flux of a collimated X-ray beam, measured by the ionization chamber at the XAS station. It is increased by a factor of 2 to 6 compared to those of Table 1, in a photon energy range of 1560 eV to 11867 eV. In addition, it becomes possible to perform a XAS experiment at arsenic K-edge (11867.0 eV), which could not been done previously with lower photon flux.

Table 2: Increased photon flux of beamline 8 after the commissioning.

Element	Edge energy of native element (eV)	Photon flux (phs/s/100mA)
Aluminum	1559.6	4.1×10^{10}
Silicon	1839.0	2.7×10^{11}
Phosphorous	2145.5	2.4×10^{11}
Calcium	4038.5	6.5×10^{10}
Chromium	5989.0	1.6×10^{10}
Nickel	8333.0	7.3×10^{9}
Zinc	9659.0	2.5×10^{9}
Arsenic	11867.0	2.3×10^{8}

Fig. 3 and 4 show XANES and EXAFS spectra of As_2O_3 recently collected at Beamline 8. Arsenic (III) oxide is commonly used as a standard representing As^{3+} oxidation state, particularly for arsenic speciation in biological and environmental research [4, 5]. The XAS measurements were performed in transmission mode using As_2O_3 powder, homogeneously spread on polyimide tape with a unit edge step.

The data acquisition time for a single XANES and EXAFS scans was 3 and 9 minutes, respectively. All of characteristic peaks were clearly observed with high signal-to-noise ratios in the XANES region (11867-11940 eV) and EXAFS region (k = 3 to 13 Å).

The region of maximum photon flux (> 10^{11} phs/s/100mA) markedly enhances XAS performance at phosphorous, sulfur, and chlorine K-edges. This highly benefit user groups of environmental and soil sciences, whose data from BL8 have been published continuously since 2009 [6-11]. Jörg Prietzel has recently demonstrated sulfur K-edge XANES spectra of diluted soil samples and standards with high quality and repeatability for accurate sulfur speciation from the current performance of the beamline.

Fig. 5 shows phosphorous K-edge XANES spectra of a soil sample collected at BL8 in March 2012 and December 2016. The soil was obtained from a site of the Damma Glacier (Swiss Alps) as a part of glacier foreland chronosequence studies [6]. Phosphorous concentration in the soil is 0.58mg/g. The XANES sample was prepared for fluorescence-yield mode by spreading the soil powder thinly and homogenously on polyimide tape. Comparing the XANES spectra, they are well reproducible. The signal-to-noise ratio in the newer spectrum is much higher because of the increased photon flux. It should be noted that the width of while line (2155 eV) is not broaden by the collimating mirror.
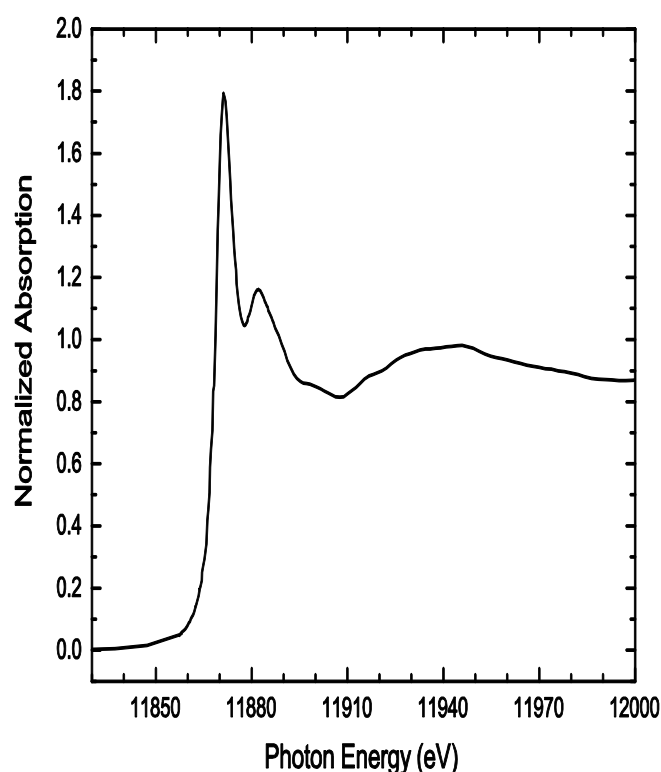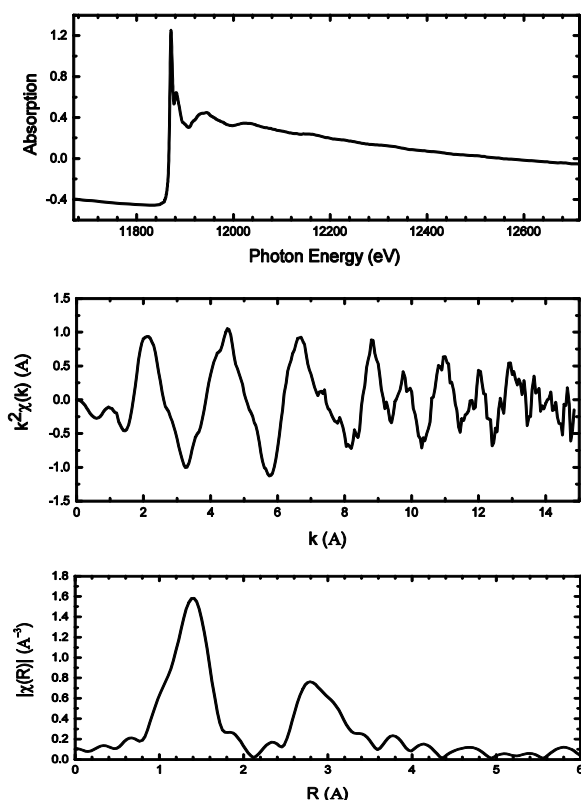

Figure 3: Arsenic K-edge XANES spectrum of As_2O_3.

Figure 4: Arsenic K-edge EXAFS spectra of As₂O₃ plotted in photon-energy space (upper panel), k space (middle panel) and R space (lower panel).
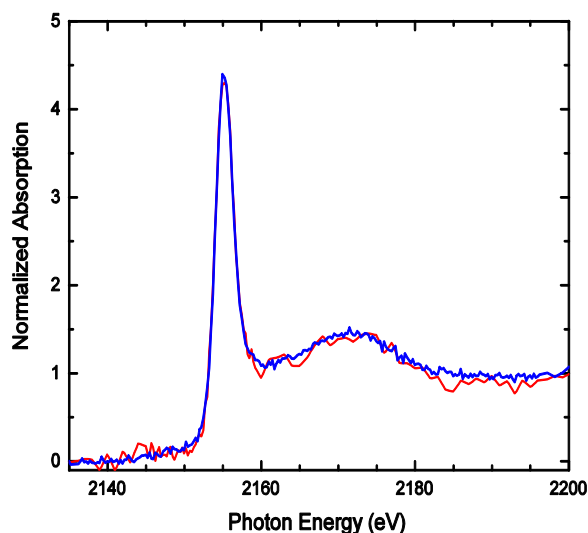

Figure 5: Phosphorous K-edge XANES spectrum of a soil sample collected in 2012 (red line) with incident photon flux of 5.6 × 10¹⁰ phs/s/100mA and 2016 (blue line) with incident photon flux of 2.4 × 10¹¹ phs/s/100mA.

Conclusion

Beamline 8 was successfully improved by addition of the X-ray collimating mirror at 4.5 meter from the bending magnet source, which can vertically collimated the synchrotron X-ray beam at the glancing incident angle of 5 mrad with the 1.8 km curvature radius. Photon flux has been increased by a factor of 2 to 6 in the photon nergy range of 1.6 keV to 11.87 keV. At low photon energy (< 5 keV), the effect of slope error on the photon energy resolution is negligible. On contrary, the slope error of the mirror increasingly affects XANES measurements in higher energy region. This requires further investigation to optimize the acceptance of the mirror for photon flux and photon energy resolution.

Acknowledgements

References

[1] W. Klysubun, *et al.,* Performance and status of Beamline BL8 at SLRI for x-ray absorption spectroscopy, *J. Synchrotron Rad.*, 2012, 19, 930-936

[2] S. Calvin, XAFS for everyone, *CRC Press*, 2013.

[3] M. Sanchez del Rio *et al.,* SHADOW3: a new version of the synchrotron X-ray optics modelling package, *J. Synchrotron Rad.*, 2011, 18, 708-716.

[4] J. G. Parsons *et al.,* Arsenic speciation in biological samples using XAS and mixed oxidation state calibration standards of Inorgamic arsenic, *Appl. Spectrosc.*, 2009, 63, 961-970.

[5] Y. Wang *et al.,* Arsenic K-edge X-ray absorption near-edge spectroscopy to determine oxidation states of arsenic of a coastal aquifer-aquitard system, *Environ. Pollut.*, 2013, 179, 160-166.

[6] J. Prietzel *et al.,* Synchrotron-based P K-edge XANES spectroscopy reveals rapid changes of phosphorous speciation in the topsoil of two glacier foreland chronosequences, *Geochim. Cosmochim. Acta*, 2013, 108, 154-171.

[7] J. Prietzel *et al.,* Soil sulphur speciation in two glacier forefield soil chronosequences assessed by S K-edge XANES Spectroscopy, *Eur. J. Soil Sci.*, 2013, 64, 260-272.

[8] K. O. Andersson *et al.,* XANES demonstrates the release of calcium phosphates from alkaline vertisols to moderately acidified solution, *Environ. Sci. Technol.*, 2016, 50, 4229-4237.

[9] M. Zuo *et al.,* Phosphorus removal performance and speciation in virgin and modified argon oxygen decarburisation slag designed for wastewater treatment, *Water Research*, 2015, 87, 271-281.

[10] J. Prietzel *et al.,* Speciation of phophorous in temperate zone forest soils as assessed by combined wet-chemical fractionation and XANES spectroscopy, *J. Plant Nutr. Soil Sci.*, 2016, 000, 1-18.

Contact

*W. Klysubun, tel: +66-44-217040; wantana@slri.or.th

Medical linear accelerator development project at Siam Photon Source

S. Klinkhieo, S. Chunjarean, N. Rusamee, R. Rujanakraikarn, K. Manasatitpong and N. Juntong

Synchrotron Light Research Institute (Public Organization), 111 University Avenue, Muang District, Nakhon Ratchasima 30000, Thailand

Abstract

A low cost medical linear accelerator (medical linac) for cancer treatment has been developed by the Synchrotron Light Research Institute (SLRI) in Thailand. Linear accelerator with the electron beam energy of 6 MeV is proposed for the first machine prototype. The key components: electron gun, accelerating cavity and X-ray target are evaluated together with the analysis of dynamic behaviour of the electrons. The accelerator control, interlocking, water cooling systems, and other sub-systems which related to the machine are re-designed to control a constant temperature, stability, and safety operation of the machine. The sub-systems installation and machine commissioning resultswill be also presented and discussed.

Introduction

Nowadays a rate of death from cancer worldwide is increasing annually. There are many types of the human cancer, each with different causes, symptoms and treatments. Each cancer differently originates. The most common cancer is originated from epithelial cells which are developing in the breast, prostate, lung, pancreas and colon. Some cancers generate from connective tissue such as bone and muscle. Symptoms of each type of cancer often appear when the cancers already spread within the patient's body. It is main reason that treatments either like surgery or combination with chemotherapy may not be effectively. Radiation therapy becomes a significantly role in cancer management. Tumors in eyes, brain and lung can get the treatment effectively with radiation. Due to the radiation can be delivered to the tumors with a high precise physical selectivity. Therefore, most of the cancer cell get kill with remaining normal cells. In addition tumor structure in brain or eyes would be preserved after the radiotherapy [1-4].

The common radiation use for the cancer radiotherapy is a high energy X-rays generated with the modern linear accelerator. Although there are several commercial linac accelerators for medical use, they generally all compose of a standard subset of components such as electron beam injector, RF power generation, waveguide, beam transport, beam collimation and monitoring and auxiliary system. In general the commercial medical linac will produce photon beam with energy of 6-20 MV for the radiotherapy. This energy range is a sufficient penetration in the tissues to cure the tumors with an effective physical selection.

Linear accelerators were introduced into Thailand almostforty years ago. They were installed at major hospitals around the country for cancer radiotherapy. The retrospective study demonstrated the gradual increase of new cancer patients during 30 years (from 1982-201), and the five most common cancers in Thailand are (1) liver, (2) lung, (3) breast, (4) gynecological (cervix uteri, corpus uteri

and ovary), and (5) head and neck (lip, oral cavity, pharynx, larynx and thyroid). It also founded that most of the cancer patients were very poor and had no resources available to pay for cancer radiation therapy services. Moreover, the lack of radiotherapy machines, basic instruments and personnel, especially radiation therapists, and medical physicists became a serious problem today [5, 6].

In 2013, The Siam Photon Source (SPS), a synchrotron light source operated by the Synchrotron Light Research Institute (SLRI) in Thailand proposed the idea of fabrication of cancer radiotherapy machine in-house. After the proposal was submitted and approved, the medical linear accelerator development project for cancer treatment started a later year. The main purpose of this project is to: (1) develop knowledge and expertise in accelerator and cancer treatment technology, focusing on medical linac, (2) build a low cost prototype of medical linac in the country, (3) reduce the machine import and preventive maintenance, as well as operating costs, (4) promote and establish the research cooperation in science and technology related to accelerator applications across the nation, and (5) increate opportunities for patients in rural areas in access to cancer treatment services [8,9]. In the first phase of the project, a prototype of medical linear accelerator is studied and designed based on VARIAN Clinac 600C machine [7-9]. The research and development will be mainly focused on the design of electron gun, accelerating structure, and X-ray target. The specifications of the machine prototype are given in Table 1.

Table 1: The specifications of medical linac prototype.

Parameters	Value
X-ray beam energy [MV]	6
X-ray dose rate [MU/min]	400-600
Field size (cm^2)	0x0 to 40x40
Type of accelerator	Standing Wave
Linac frequency [MHz]	2998

The paper will report the current status of medical linear accelerator development project at SLRI, and describe the overview and basic concepts of linear accelerator for cancer treatment. The details of in-house research and engineering development will be presented and discussed, together with machine prototype installation and commissioning results.

Medical linear accelerator

The linear accelerator (Linac), uses microwave power provided by magnetron to accelerate electrons, which is generated from electron gun, to through a linear tube (called accelerating structure) to high speeds, then these electrons collide to a heavy metal target in which the high speed

electrons are slowed down. As a result of these collisions, high energy X-rays are produced from this target (called X-ray target). These high energy X-rays will be directly transported to the patient's tumor and shaped as they exit the linac to conform to the shape of the tumor. X-ray treatments are designed in a way that destroy the cancer cells while sparing the surrounding normal tissue [1-4].

The final design of electron linac at SLRI is illustrated in Fig. 1. This includes the engineering detail drawing of electron gun, accelerating cavity, and X-ray target, respectively.
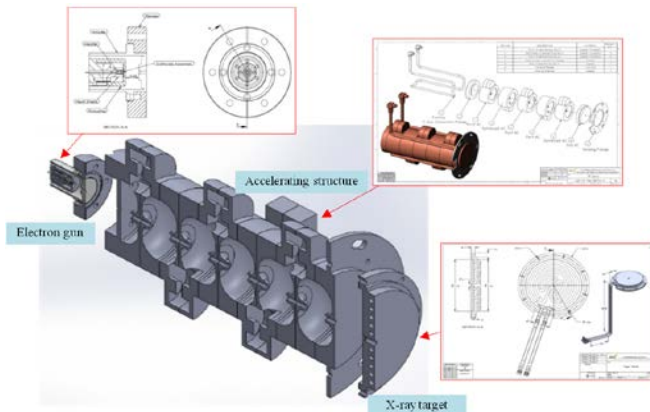

Figure 1: The diagram of medical linac prototype.

Electron gun

An electron gun is an electrical component in the vacuum tube and also is the basic part of the linear accelerator. There are several types of electron gun which is classified by electric field generation (DC or RF), emission mechanism (thermionic, photocathode or clod emission), focusing system or by the number of electrodes (diode or triode). A diode electron gun is suitable for the low energy linac for medical therapy with low beam current. In order to produce the beam current and energy of 400 mA and 30 KeV at the electron gun exit for the medical linac at the SLRI, the diode type is an appropriate solution to satisfy operational requirements.

The diode gun composes of cathode and anode. There are two separate electric potentials; cathode and focusing electrode which is set to be negative voltage of -30 kV and anode which is always grounded. After the cathode surface get heat, free electrons emitted and extracted have to be focused by the focusing electrode. Base on geometry, the design gun for the SLRI medical linac is a Pierce type configuration with focusing electrodes on the anode side.

Based on design and simulation resultsfrom the CST code, the electron beam emitted with thermionic emission can be focused and extract out of the anode with the beam current and small Perveance of 400 mA and 10^{-7}, respectively. All extracted electrons will be delivered to the cavity in order to accelerate the energy up to 6 MeV. The gun characteristics is listed in Table 2.

Table 2: The gun characteristics.

parameters	Value
gun inner radius [mm]	17.5
gun length [mm]	25
anode voltage [Volt]	0
cathode voltage [volt]	-30000
Perveance	10^{-7}
Electron beam parameters	**Value**
Peak beam current [mA]	399
r.m.s beam emittance [mm-mrad]	0.231

Accelerating structure

Linac or accelerating cavity is used for build energy of electron up to a desired energy on a linear path. The electrons travel only once through each of linac cells which are operated at radio frequencies (RF). The accelerating structures are driven by a sinusoidal voltage source with a frequency matched to the resonant frequency of the structure. Due to the change of the polarity of voltage with the time, the electrons are decelerated rather than accelerated. Therefore the electron flow would be bunched with arrival frequency at the accelerating gap matched with the frequency of the voltage waveform.

Table 3: The design linac parameters.

Parameters	Accelerating and Side coupling			
	Optimized cell [mm]	First cell [mm]	Port cell [mm]	End cell [mm]
Inner corner radius, β	5.5	5.5	5.5	5.5
Cavity radius, γ	37.554	37.554	37.375	37.554
Inner nose cone radius, δ	1	1	1	1
Nose cone length, ε	10.877	10.877	10.877	10.877
Beam tube radius, ζ	2.5	2.5	2.5	2.5
Post length, α	9.56	9.56	9.56	9.56
Parameters	Waveguide port			
Coupling port area [mm]^2	22.0×15.5			

Both standing wave and travelling wave linac structures are like a series of individual resonators that are electromagnetically coupled to provide energy to flow from one cell to the next. There are two types of coupling which depends on opening connects regions of high magnetic field

Table 4: Target accelerator characteristics.

Parameters	Temp @ 25 ºC	Temp @ 40 ºC
Q_0 (unloaded) factor	16050	16108
Q_{ext} factor	8161.65	8105.17
R/Q	1857.0	1863.5
Shunt Impedance [MΩ]	29.80	30.02
Resonance frequency [MHz]	2999.29	2998.50
Coupling Coefficient, β	1.97	1.99

(magnetic-coupling) or regions of high electric field (electric-coupling). In order to make the medical linac at the SLRI more compact, a side coupling with the electrical coupling structure is used. Based on the design, the 6 MeV S-band side coupling standing wave with microwave frequency of 2998 MHz is used. In operation we select $\pi/2$ mode because of a good stability over temperature variation and less geometrical tolerances. All design linac parameters are listed in the Tables 3 and 4.

X-ray target

The collision of the electrons with the high density transmission target creates the X-rays (photons), forming a forward peaking shape of photons beam in the direction of the patient's tumor. From the simulation with the CST code, electron beam current out of the linac exit will be delivered to the X-ray target which should be high atomic number (Z) materials like tungsten (W). With tungsten thickness of 2.7 mm, we can effectively produce the desired radiation dose rate at the isocenter. But there are some electrons leak out after hitting the tungsten. Therefore, to filter these electron the *Be* with the thickness of 3 mm will be used.

Machine instalation and commissioning

The prototype of medical linac have been installed and commissioned. The donated parts of electron gun, accelerating structure, and X-ray target are temporarily used and modified for this test. Other system components related to the machine both hardware and software, are designed and developed in-house. The box diagram of medical linac components, machine installation and commissioning works are shown in Fig. 2 and 3, respectively. The following sub-sections will briefly describe the function and operation of some sub-systems.

Treatment head

It consists of the X-ray target, primary collimator, beam flattening filter, ion chambers, and secondary collimators, which designed to shape and monitor the treatment beams for X-ray therapy.

Magnetron

It provides microwave power to accelerate the electrons, basically used for lower electron energies, 4 MeV to 6 MeV linacs.
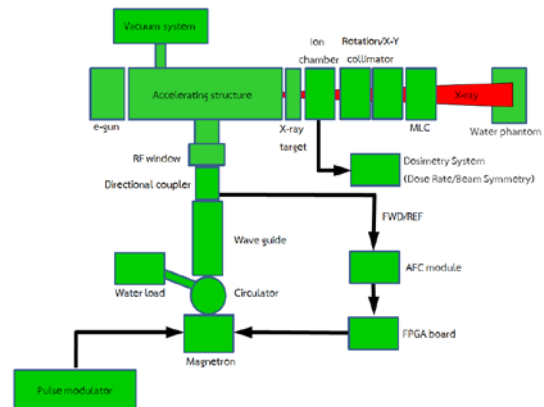

Figure 2: The diagram of medical linac prototype.

Figure 3: The system installation and commission.

The main cabinet

It is located inside the treatment room, contains 3 sub-components: (1) fan control, (2) cooling the power distribution system, and (3) the power distribution system with the interlocking safety system.

The Water Cooling System

The water cooling system provides thermal stability to the system components, allows all components to operate at a constant temperature.

Monitor Ionization Chambers

They monitor integrated dose, and dose rate, as well as field symmetry. The radiation from the X-ray target will passthrough these chambers, then they produce an ionization current, which is proportional to the X-ray of electron beam intensity.

Collimators

The radiation beams are collimated by adjusting the upper and lower collimator jaws. The jaws are made of high Z number (like W or Pb). These jaws can define a rectangular shaped beam up to 40x40cm for X-ray beams.

Multi Leaf Collimators (MLCs)

MLCs are a bank of large number of collimating blocks or leaves, can be moved automatically independent of each other to create block to spare normal tissue and direct the radiation dose to the tumor [7].

X-ray production

The main mechanism for X-ray production in medical linac is the process called Bremsstrahlung, or breaking radiation [1-3]. The electrons that have been accelerated are then shot at a X-ray target. These relativistic electrons then are slowed down or stopped very quickly. In the process of being stopped they emit high energy X-rays in the direction of their initial motion. The energy of the resultant X-rays is approximately the energy of the electron when they hit the target [1-3, 7]. The X-ray productionof SLRI medical linac prototype is set up using the donated medical linac from Srinagarind hospital, Khon Kaen. The reverse engineering approach has been employed together with design development of the new components and sub-systems to produce the X-rays [8, 9].
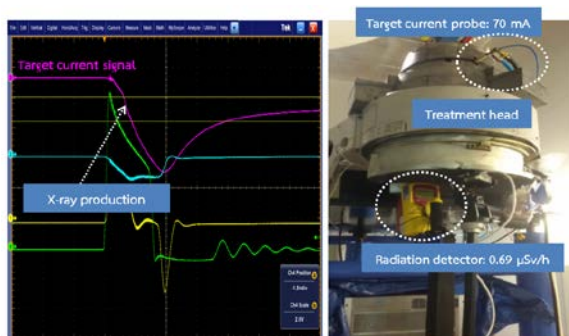

Figure 4: The X-rays commissioning and detection.

The testing shows an impressive results of X-ray production demonstrated by the target current of 70 mA at X-ray target and real-time radiation detector of 0.69 μSv/h (X-ray background: 0.04 μSv/h), respectively. The Fig. 4 shows the commissioning and X-ray monitoring system of medical linac prototype in Booster synchrotron (10 meters deep with radiation shielding wall protection) of SLRI.

Conclusions

The prototype of medical linac at SLRI has been successfully installed and commissioned. The donated

medical linac is implemented for X-ray production test. The incomplete or missing components, including hardware and software of a donated machine are re-designed and developed by the engineering team at SLRI. The in-house design of electron gun, accelerating structure, and X-ray target are under developed by the SLRI physicists together with manufacturing experts from Taiwan. These three components are currently in a fabrication progress, and expected to be ready for installation and testing by the end of 2017.

Acknowledgements

References

[1] H.D. Suit, Potential for improving survival rates for the cancer patient by increasing the efficacy of treatment of the primary lesion, *Cancer*,1982, 50, 1227-1234.

[2] European Commission, Europe against cancer, European Network of Cancer Registries, International Agency for Research on Cancer (IARC) and World Health Organization (WHO), Office for Official Publications of the European Communities, L-2985 Luxembourg, 1995.

[3] Faiz M. Khan, The Physics of Radiation Therapy (3rdedition), 1995.

[4] Charles M. Washington, Denis Leaver. Principles and Practice of Radiation Therapy, *Mosby-Year Book Inc*, 1996,.

[5] T. Thungrassami*et al*., 30 Year of Radiation Sevice in Southern Thailand: Workload vs Resource, *Asian Pacific Journal of Cancer Prevention*, 2003, 14.

[6] S. Grover *et al*., A systematic review of radiotherapy capacity in low- and middle-income countries, *frontiers in oncology*, 2015,4, Article 380.

[7] S. Aubin*et al*., Integrated 6 MV linear accelerator model from electron gun to dose in water tank, *Med. Phys.* 2010, 37(5), 2279-2288.

[8] N. Juntong *et al*., Design of Electron gun and S- band structure for Medical Electron Linear Accelerator, *IPAC' 16, Pusan, Korea*, 2016.

[9] N. Juntong *et al*., The Optimized X-ray Target of Electron Linear Accelerator for Radiotherapy, *IPAC' 16, Pusan, Korea*, 2016.

Contact

*S.Klinkhieo, tel: +66-44-217040 ext 1415; supat@slri.or.th

A design of combined function magnet prototype for Siam Photon Source

P. Sunwong, S. Chaichuay, A. Kwankasem, V. Suksrimuang, B. Boonwanna and P. Klysubun

Synchrotron Light Research Institute (Public Organization), 111 University Avenue, Muang District, Nakhon Ratchasima 30000, Thailand

Abstract

A prototype of combined dipole-quadrupole magnet has been developed for future upgrade of Siam Photon Source (SPS). The magnet is an offset quadrupole design with the dipole field of 0.6 T and quadrupole gradient of 30 $T \cdot m^{-1}$. The good field region of ± 10 mm, where the calculated gradient error is less than 10^{-2}, can be obtained by optimization of the pole profile. Iron yoke of the magnet and water-cooled coils will be fabricated and tested in-house. Magnetic field measurements will be performed using Hall probe technique and rotating coil method to determine the magnetic field quality for further improvement.

Introduction

Combined function magnets have been implemented in many accelerator systems and synchrotron radiation sources where the high-performance and compact machine is needed. Magnetic field with different functionalities such as dipole, quadrupole and sextupole are put together either by having multiple coils winding on the same yoke and/or by adjusting the pole profile. For combined dipole-quadrupole (DQ) magnet, modified dipole or tapered dipole design is widely used because of its simplicity and a large good filed region (GFR) can be achieved. However, quadrupole gradient of the tapered dipole is not high, generally less than 10 $T \cdot m^{-1}$ with the exception of DQ magnet designed for Diamond DDBA lattice upgrade where the gradient of 14.385 $T \cdot m^{-1}$ is obtained [1]. High gradient DQ magnet was successfully designed by ESRF based on offset quadrupole concept with single-sided design to reduce power consumption [2]. The quadrupole gradient is 36.8 $T \cdot m^{-1}$ with the dipole field of 0.56 T.

In this work, a prototype of DQ magnet is designed based on the offset quadrupole concept similar to ESRF's design. With the target fields of 30 $T \cdot m^{-1}$ and 0.6 T, the offset will be 20 mm. This becomes a challenge for the magnet design as it is quite far from the center of original good field and also constricts the space for vacuum chamber.

Magnet design

Specification and Requirements

Specification of DQ magnet is summarized in Table 1. The dipole field component is 0.6 T and the defocusing quadrupole gradient is 30 $T \cdot m^{-1}$. The required beam stay-clear (BSC) is ± 20 mm and ± 4.5 mm in horizontal and vertical directions, respectively. The BSC requirement limits the minimum magnet gap to 14 mm, taking into account the total thickness of chamber wall and clearance of 2.5 mm. The required GFR where the gradient error is less

than 10^{-2} is preliminarily ± 10 mm. Magnet aperture, or the bore radius, is not a limiting factor.

Table 1: Specification of DQ magnet prototype

Parameter	Value	Unit
Dipole field strength	0.6	T
Quadrupole gradient	30	$T \cdot m^{-1}$
Horizontal BSC	± 20	mm
Vertical BSC	± 4.5	mm
Minimum magnet gap	14	mm
GFR where $\Delta G/G < 10^{-2}$	± 10	mm

2D design and optimization

In order to achieve the quadrupole gradient of 30 $T \cdot m^{-1}$, the offset quadrupole design was chosen. One side of the magnet consists of two quadrupole-type poles (main poles), while another side consists of two poles with smaller pole radius and off-center hyperbolic profile (auxiliary poles). Cross section of the DQ magnet on x-y plane is illustrated in Fig. 1 which also shows the magnetic field distribution extracted from POISSON simulation. Several parameters such as yoke thickness, pole radius, applied current, number of turns for both pole types, quadrupole offset, center of auxiliary poles, vertical gap and shimming were adjusted for the desired magnetic field strength and quality while maintaining the engineering feasibility. Iron yoke material is S10C low-carbon steel. Magnet coils is water-cooled type made from 7.5 mm × 7.5 mm copper conductor with 4 mm-diameter hole. Number of turns is 30 for the main poles and 6 for the auxiliary poles. The coils electrical circuit is in series. Operating current is 215 A for the design values of dipole field and quadrupole gradient. The quadrupole magnet offset is 20 mm.
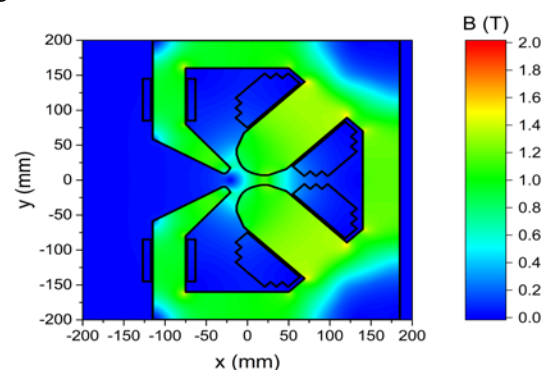

Figure 1: Magnetic field distribution of DQ magnet prototype extracted from POISSON simulation. The yoke material is S10C. The turn number is 30 for the main poles and 6 for the auxiliary poles. The applied current is 215 A.
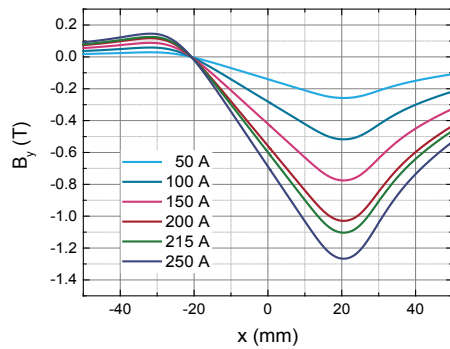
Figure 2: Vertical field component of DQ magnet prototypealong x coordinate obtained from POISSON simulation.

Fig. 2 shows the calculated vertical field component (B_y) along x coordinate for different applied currents. At the magnet center (x=0), magnetic field strength reaches 0.6 T requirement at the applied current of 215 A. The quadrupole gradient can be calculated from dB_y/dx in Fig. 2. Fig. 3 shows the plots of dipole field and quadrupole gradient as a function of applied current up to 300 A where the fields begin to saturate.
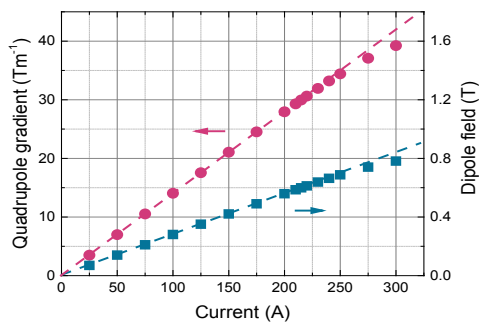

Figure 3: Dipole field and quadrupole gradient of DQ magnet prototype as a function of applied current obtained from POISSON simulation.

The field quality of DQ magnet is determined by the quadrupole gradient errors $\Delta G/G$. The normalized field gradient of DQ magnet prototype is plotted in Fig. 4 for applied current up to 250 A. The gradient errorat -10 mm < x < 10 mm is within 10^{-2} for all applied currents. Pole profile of the magnet was optimized by shimming at the operating current of 215 A, therefore $\Delta G/G$ is minimized at this current. For -8 mm < x < 8 mm, the gradient error is below 10^{-3}.

3D Simulation

A model of DQ magnet prototype with the optimized 2D pole profile is created in Radia for 3D simulation. The main purpose is to calculate magnetic field along the magnet
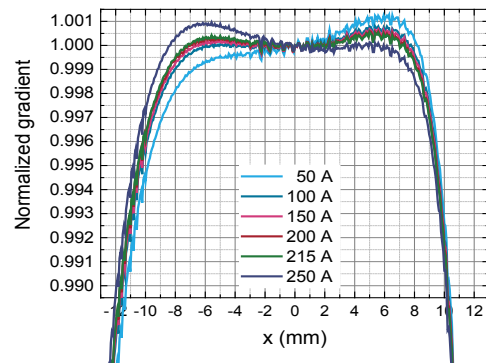

Figure 4: Normalized field gradient of DQ magnet prototype along x coordinate obtained from POISSON simulation.

length in z direction and to qualitatively check the simulation results from POISSON. Effective length of the magnet can be estimated from $\int B_y dz/B_0$. In this work, accurate value of magnetic field from Radia simulation cannot be obtained in a reasonable simulation time due to a large number of sub-volumes in subdivision process.

Ongoing and future works

The DQ magnet prototype for future SPS upgrade is currently being fabricated at the Siam Photon Laboratory (SPL). The magnet poles will also have a curvature along the magnet length to follow the beam orbit and ensure that electrons will be at the center of GFR. The hollow conductor will be insulated with fiberglass cloth tape before winding into coil. The coil is then impregnated in epoxy by vacuum pressure impregnation process. Magnetic field quality of the magnet will be investigated and cross-checked by Hall probe technique and rotating coil measurements. Some possible improvements of this project are accurate 3D design process, fabrication techniques for the magnet pole and better machining tolerance.

Acknowledgements

References
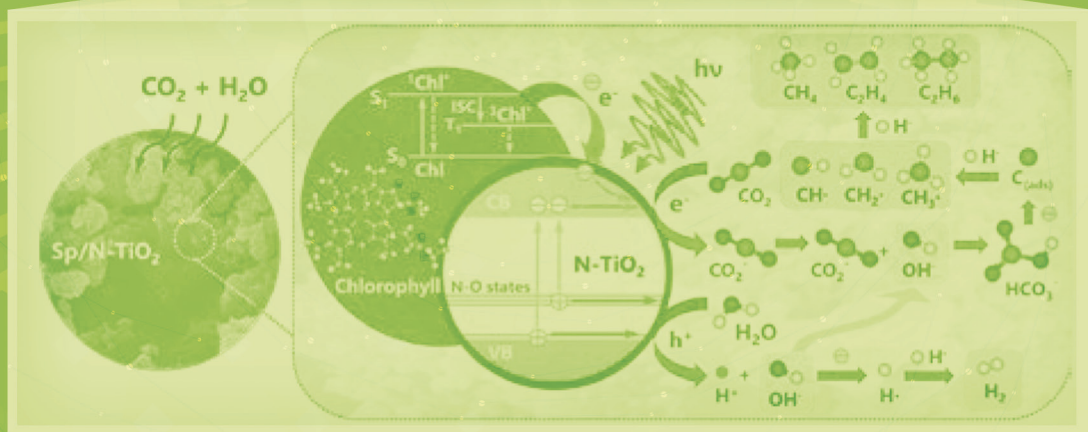
[1] C. Bailey *et al*., Magnet Design for the Diamond DDBA Lattice Upgrade, *Proc. IPAC'14*, 2014, 1319-1321.
[2] C. Benabderrahmane *et al*, Magnets for the ESRF-EBS Project, *Proc. IPAC'16*, 2016, 1096-1099.

Contact

*P. Sunwong, tel: +66-44-217040 ext 1528; prapaiwan@slri.or.th

RESEARCH
ACTIVITIES

SR-IR microspectroscopy to track biochemical differences of human bone and cartilage as relation with Osteoarthritisknee

K. Thumanu[1]*, P. Ngernsoungnern[2], A. Ngernsoungnern[2] and B. Sindhupakorn[3]*

[1]Synchrotron Light Research Institute (Public Organization), 111 University Avenue, Muang District, Nakhon Ratchasima 30000, Thailand
[2] School of Pre-clinic, Institute of Science, Suranaree University of Technology, Nakhon Ratchasima, 30000, Thailand
[3] Orthopedic department, School of medicine, Suranaree University of Technology, Nakhon Ratchasima, 30000, Thailand

Abstract

Osteoarthritis (OA) is characterized by degenerative cartilage and thickening of the subchondral bone under the cartilage. In OA, articular cartilage change in collagen and photeoglycan (PG) content play an important factor in disease progression. SR-IR technique has been used to determine the structural components of articular cartilage such as collagen and proteoglycan.The objective of this research is to use FTIR microspectroscopy for investigating structural changes in biocomponent of decalcified bone sample related to difference amount of material presents such as protein Amide I, protein Amdie II, protein Amdie III andmproteoglycanparbohydrate. Femoral condyle samples were collected from male and female between 21, 47, and 82 years old who underwent Total knee arthroplasty (TKA) and anterior cruciate ligament (ACL) reconstruction. We use Mayer's hematoxylin& eosin (Bio-Optica, Milano, Italy) for the conventional histological study, 2) alcian blues pH 2.5 (Sigma-Aldrich) for studying of the presence of proteoglycans, and 3) Masson's trichrome for identifying of collagen fibers and bone matrix. For SR-IR technique, Spectra data were collected at an infrared micro spectroscopy beamline (BL4.1 IR Spectroscopy and Imaging) at Synchrotron Light Research Institute (SLRI). The results show peak intensity of amide I and amide III collagen from the cartilage region were clearly observed decreased as corresponding with the increase of age at 82 year. This is corresponding with the histology staining results as revealed that the articular cartilage was observed the degradation at the 82 year of OA person. Amounts of proteoglycans in the femoral medial condyles of both OA people increased when compared to that of the normal person. It revealed that even in the late stage of OA, the amount of proteoglycans still more than that of the normal person. From the present study showed that the amounts of the collagen fibers decreased in OA person.

Introduction

Osteoarthritis (OA) is an aging disease in which mechanical factors lead the important role. This disease is characterized by degenerative cartilage and thickening of the subchondral bone under the cartilage [1, 2]. Our purpose of study will find biocomponent changes of calcified cartilage in the control and OA group. There were no extensive studies about biocomponent comparing the normal subchondral bone, calcified cartilage and the articular cartilage affected by the OA in femoral condyle of femur. Therefore, the aim of our study was to assess the biocomponent changes of the articular cartilage, calcified cartilage and underlying subchondral bone of the medial condyle of femur in different age by using Infrared microspectroscopy technique.

Material and methods

Sample isolation
Femoral Condyle Bone and Cartilage Sample Collection

Femoral condyle samples were collected from male and female between 21, 47, and 82 years old who underwent Total knee arthroplasty (TKA) and anterior cruciate ligament (ACL) reconstruction. Exclusion criteria are patients who have inflammatory joint disease, steroid injection prior surgery, high blood calcium and current drug history of bisphosphonate therapy. Samples were collected with under approval of medical ethics commission, consent of the medical institute of Suranaree University of technology and consent patient form. All the samples were collected from medial condyle of femur with cylindrical osteochondral explant. The size range from 3-4 cm. x 4-13 cm. Control sample is 21 year old who underwent ACL reconstruction and has no macroscopic evidence of articular cartilage degeneration or osteoarthritis. Study samples are 47 and 82 who underwent TKA. Study subjects are grading OA by Kellgren and Lawrence system in grade 3. Both control and study samples are collected from medial condyle of distal femur.

Sample preparation

Tissues of femoral medial condyle of normal (21 years old woman) and osteoarthritis (OA) samples (47 and 81 years old women) and were cut into small pieces and fixed with 10% neutral buffered formalin (Sigma-Aldrich, St. Louis, MO, USA) for one week at 4º C, followed by washing with 70% ethanol. Decalcification was performed by immerging the tissues in Decalcifying Solution-Lite (Sigma-Aldrich) for overnight at room temperature. The tissues were subsequently dehydrated through graded ethanol series, embedded with Surgipath Paraplast (Leica Microsystems, Buffalo Grove, IL , USA), and sectioned at 5 □m thick with Rotary Microtome HM 355S (MICROM International GmbH, Walldorf, Germany).

SR-IR microspectroscopy

For SR-IR technique, the bone were embedded with SurgipathParaplast (Leica Microsystems, Buffalo Grove, IL , USA), and sectioned at 5 mm thick with Rotary Microtome HM 355S (MICROM International GmbH, Walldorf, Germany) and put on infrared transparent BaF2 windows (13x2 mm) for infrared microspectroscopy. Spectra data

were collected at an infrared microspectroscopy beamline (BL4.1 IR Spectroscopy and Imaging) at Synchrotron Light Research Institute (SLRI). Spectra were acquired with a Vertex 70 FTIR spectrometer (Bruker Optics, Ettlingen, Germany) coupled with an IR microscope (Hyperion 2000, Bruker) with an MCT detector cooled with liquid nitrogen over the measurement range from 4000 to 800 cm-1. The microscope was connected to software-controlled microscope stage and placed in a specially designed box that was purged by dry air. The measurements were performed in the mapping mode, using an aperture size of 10 × 10 µm with a spectral resolution of 4 cm-1, with 64 scans co-added. Spectral acquisition and instrument control was performed using OPUS 7.2 (Bruker Optics Ltd, Ettlingen, Germany)

Results
Histology of the femoral medial condyle of normal and OA people

In the normal person, conventional histological staining revealed that articular cartilage of the medial femoral condyle consisted of three areas including superficial, transitional, and radial zones (Fig. 1A). The superficial zone consisted of chondrocytes housed in lacunae. Mostly, each lacuna contained one cell. The transitional zone consisted of higher numbers of chondrocytes. Some lacunae contained more than one cells. The radial zone contained chondrocytes that were arranged perpendicular to the articular surface. Cell density was lowest in the radial zone. Most of the lacunae contained numbers of cells. This zone located closely to calcified cartilage and was separated from the calcified cartilage by a tidemark (Fig. 1B). The calcified cartilage lied closely to the subchondral bone. The structures of the articular cartilage, calcified cartilage, and subchondral bone of the 47 year-old OA woman were seen similarly to that of the normal person (Fig. 1C). In contrast, erosion was observed in the articular cartilage and calcified cartilage of the 82 year-old OA person (Fig. 1D).
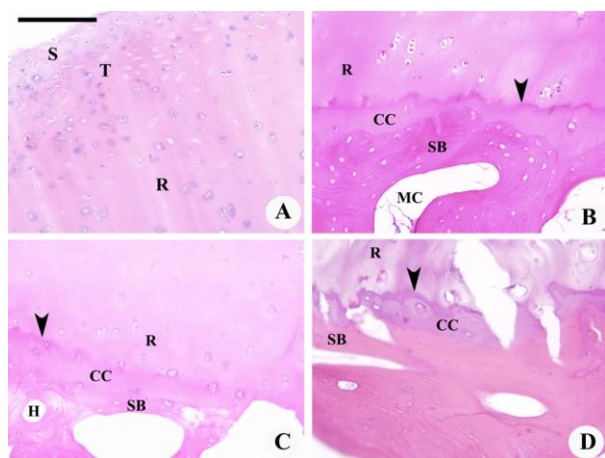

Figure 1: Histology of femoral medial condyles of the normal (A and B), 47 years old OA person (C), and 82 years old OA person (D). The articular cartilage of the condyle is

divided into the superficial zone (S), transitional zone (T), and radial zone (R). The radial zone is separated from the calcified cartilage (CC) by a tidemark (arrowhead). Deeper to the calcified cartilage is the subchondral bone (SB). MC, medullary cavity. Scale bar = 200 µm.

SR-IR microspectroscopy technique

Characteristic band assignment of bone sample can be classified to four regions as seen in Table 1. The most prominent band of bone sample are produced by the collagen protein (Amide I, Amide II and Amide III) (Table 1).

Table 1: The Infrared absorption of the bone sample

Functional group	Wavenumber (cm^{-1})	References
Protein Amide I collagen	1700-1600	Kobrina, Y. et.al. 2012, 2014
Amide I C=O		Kobrina, Y. et.al. 2012, 2014
Beta sheet	1638-1644	Kobrina, Y. et.al. 2012, 2014
Alpha helix/Beta turn	1660-1668	Kobrina, Y. et.al. 2012, 2014
Beta sheet	1692	Kobrina, Y. et.al. 2012, 2014 ;Figuiredo, M.M. et.al. 2012
Protein Amide II (C-N Stretching/NH bending/C-C Stretching of collagens)	1600-1500	
Protein Amide III collagen	1338	Boskey, A. et.al. 2007 ; Kobrina, Y. 2014
Proteoglycan Carbohydrate (C-O Stretching vibration of carbohydrate residue in collagen an proteoglycan)	1140-985	Kobrina, Y. 2014 : Potter, K. et.al. 2001

As mentioned from methodology sectioned, the sample were decalcified and then will be measured the IR spectra of Amide I collagen, Amide II collagen, Amide III collagen, Sulfate from glycoaminoglycansidechain of aggrecan, Proteoglycan Carbohydrate. Infrared spectra of the bone sample from decalcified sample collected at different parts of the sample were extracted and separated into three parts: cartilage, calcified cartilage, bone region. IR spectra compared between age-dependent from three regions: cartilage, calcified cartilage and bone was shown in Fig. 2.
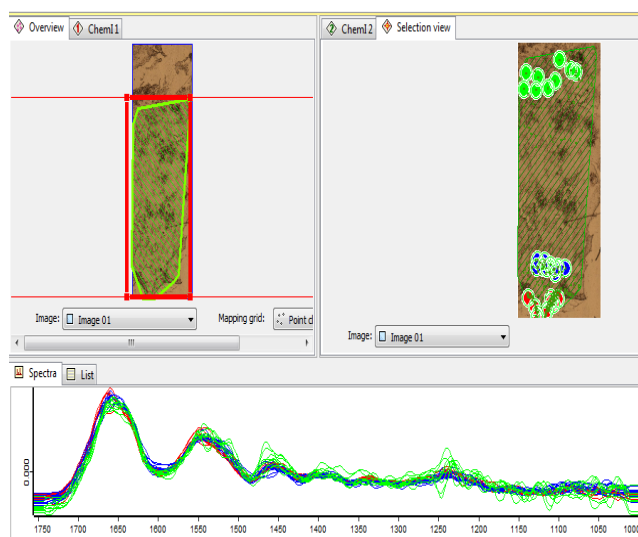
Figure 2: Functional group area maps obtained under the spectral region between 1750–1000 cm^{-1} of bone specimens at different area measurement: human bone (red color) , calcified cartilage (blue) and cartilage (green) at 82 year of age. The measurement were performed by point to point measurement with aperture setting at 10 × 10 µm square aperture, 4 cm^{-1} 64 scans using SR-IR microspectroscopy

The peak intensity of amide I and amide III collagen from the cartilage region were clearly observed decreased as corresponding with the increase of age at 82 year. This results is corresponding with the histology staining results as revealed that the articular cartilage was observed the degradation at the 82 year of OA person. This is confirmed by the straining results as showing the lower amount of collagen fibril in the cartilage region compared with normal control. At the age of 82 year, the degradation of the amide I and amide III collagen were observed in cartilage, calcified cartilage and bone region.

At the late stage of ages, the increase of amide II / amide I ratio was observed in the spectra from cartilage. Furthermore, the amide III/ amide II ratio were appeared the decrease in peak intensity at the spectra from cartilage and classified zone. The less amount of collagen was appeared to the process of collagen degradation as tissue becomes more osteoarthritis (Fig. 3). These results demonstrate that the spectral changes of these spectral signature biomarkers from the collagen molecule as indicator of type II collagen damage is found in the late stage of the OA. The ratio of amide II collagen/amide I collagen was utilized as a spectral marker of collagen orientation.

Discussion

Generally, the major component of the extracellular matrix of the articular cartilage is proteoglycans [3]. Histological staining of proteoglycans in the present study showed that amounts of proteoglycans in the femoral medial condyles of both OA people increased when compared to that of the normal person. A previous study reported that rate of proteoglycan synthesis increased in the early OA condition [4]. This could be related to a repairing process

of the cartilage. The rate proteoglycan synthesis decreased with the progression of OA [5] which caused an elevation in apoptotic rate of the chondrocytes. Thus, the amounts of the proteoglycans decreased in late stage of OA [6]. However, result of the present study revealed that even in the late stage of OA, the amount of proteoglycans still more than that of the normal person. Result of the present study showed that the amounts of the collagen fibers decreased in both OA people, especially that of the older OA person. This is similar to the results reported in previous studies. It was found that articular cartilages of OA people were degenerated in association with the denaturation of type II collagens [7]. Some also reported that OA people had an increasing in the percent denaturation of the type-II collagens. The collagens were found to be cleaved by collagenases [8].

In the present study, the collagen fibers were also identified around the lacunae of the chondrocytes located in the calcified cartilage of the normal person. There are a report that type-X collagens were localized in the calcified cartilage [9]. They suggested that this type of collagen fibers involved in the regulation of the mineralization and also plays a crucial role in bone remodeling. Moreover, in the present study, the collagen fibers were not identified in the calcified cartilage of the OA people. This could indicate that
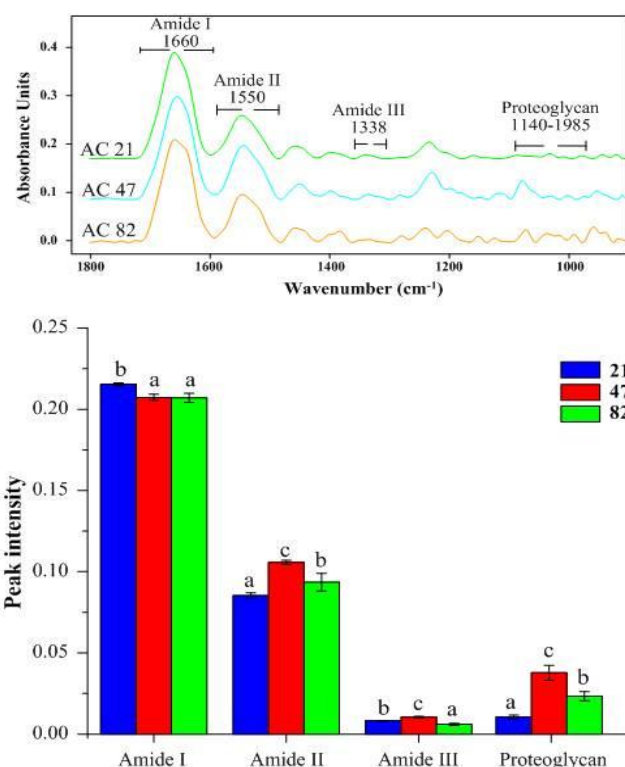

Figure 3: Average the original spectra of IR spectra extracted from the articular (AC) region at different age (21y, 47y, 82y) of patients. Note: Each group was collected spectra approximately 100 spectra. Average the spectra were preprocessed with 13 points of smoothing, baseline correction and vector normalization over the spectral range of 1800–900 cm^{-1}
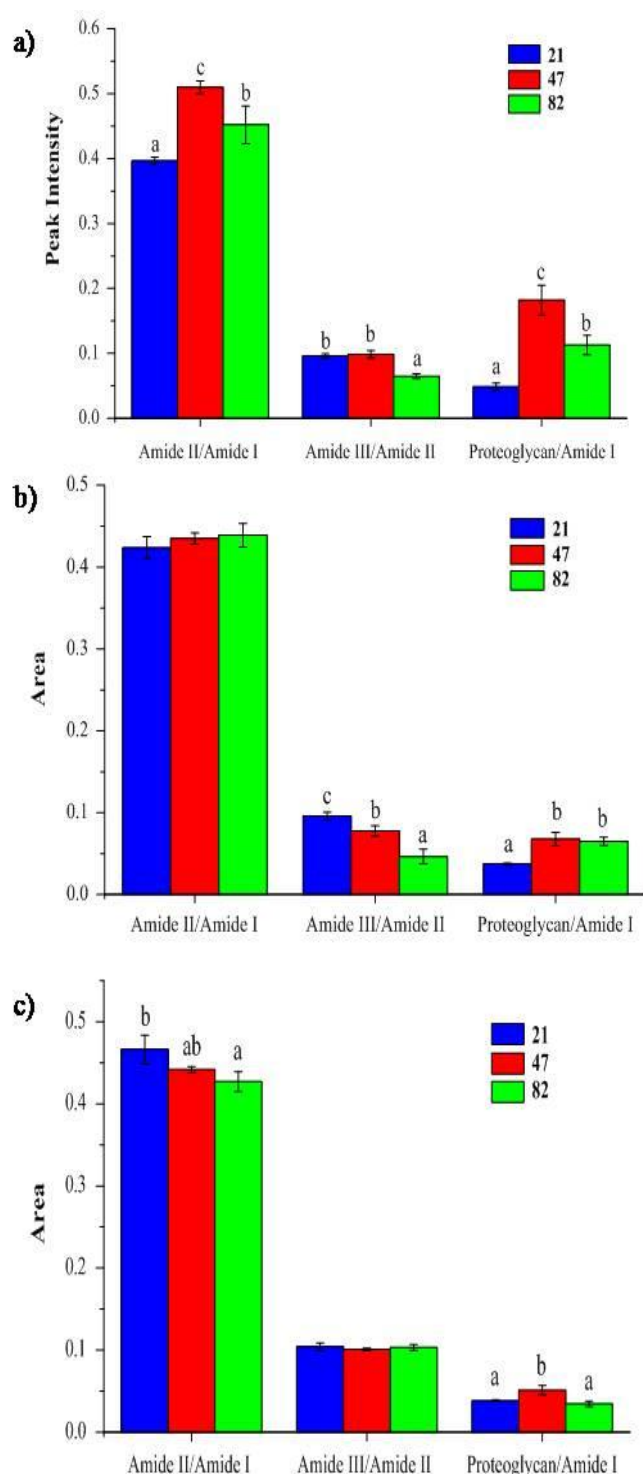
Figure 4 : The integrate ratio of the peak intensity of IR spectra extracted from the articular (AC) (a), calcified cartilage (CC) (b) and subchondral bone (SB) (c) at different age (21y, 47y, 82y) of patients. Note: Average the spectra were preprocessed with 13 points of smoothing, baseline correction and vector normalization over the spectral range of 1800–900 cm^{-1}

their calcified cartilages were completely mineralized resulting in an increasing of bone matrix in their calcified cartilages. In addition, the mineralization was also dispersed into their articular cartilages causing a decreasing of collagen fibers.

Spectra features of IR spectra from the bone specimens was mainly originated from absorbance of Amide I and Amide II collagen molecule. Collagen molecule is the mainly part of cartilage solid matrix which is strongly used for analysis of the collagen content. Amide II and Amide III is related to CH2 bending vibration, CH3 asymmetric bending, COO- stretching vibration. CH2 side chain vibration of collagen. Especially, the small CH2 side chain at 1340cm-1 of IR band is usually important for characterization feature of collagen. The carbohydrate region (1140-980 cm-1) is related to stretching vibration of C-O, C-OH, C-C ring vibration which is more specific to proteoglycan. [10-12]. The degradation of amide III and amide I was observed at the late stage of age as the same results compared with the spectra from cartilage region. The degeneration of the cartilage and calcified cartilage can be observed by these two bands. This biomarker band can be used to indicate orientation of collagen fibril network. The peak intensity of amide I and amide III collagen from the cartilage region were clearly observed decreased as corresponding with the increase of age at 82 year. This result is corresponding with the histology staining results as revealed that the articular cartilage was observed the degradation at the 82 year of OA person.

The ability of FTIR spectroscopy to characterize biochemical component of human bone at age dependent condition has been investigated by comparing between normal sample (age 21y) and sample from patient diagnosed with OA. The advance of SR-IR technique is its ability to measure the distribution of biochemical profile at the high spatial resolution by focusing at the measurement area of 10x10 μm. These results suggested that the change in chemical composition of articular cartilage caused by OA progression which can be investigated by using SR-IR technique. This study demonstrated that the role of SR-IR microspectroscopy can be rapidly applied to characterize the distribution and structure of cartilage components. It also enables to correlate between cartilage properties and function. In summary, SR-IR microspectroscopy can provide valuable information to reveal compositional and structural changes in cartilage which is an indicator to detect the early stage of osteoarthiritic degradation.

Acknowledgements

References

[1] Kamibayashi L. *et al*., Trabecular microstructure in the medial condyle of the proximal tibia of patients with knee osteoarthritis, *Bone*, 1995, 17, 27–35.

[2] Radin EL. *et al*., Subchondral bone changes in patients with early degenerative joint disease, *Arthritis Rheum,* 1970, 13, 400–5.

[3] West, P.A *et al.*, Fourier transform infrared imaging spectroscopy analysis of collagenase induced cartilage degradation, *J. Biomed.Opt*, 2015, 10, 14015.

[4] Knudson CB *et al.*, Cartilage proteoglycans. *seminars in Cell & Developmental Biology*, 2001, 12, 69–78.

[5] Nelson F *et al.*, Early post-traumatic osteoarthritis-like changes in human articular cartilage following rupture of the anterior cruciate ligament, *Osteoarthritis and Cartilage*, 2006, 14, 114-119.

[6] Rizkalla G. *et al.*, Studies of the Articular Cartilage Proteoglycan Aggrecan in Health and Osteoarthritis, *J. Clin. Invest*, 1992, 90, 2268-2277.

[7] Sabatini M *et al.*, Effects of Ceramide on Apoptosis, Proteoglycan Degradation, and Matrix Metalloproteinase Expression in Rabbit Articular Cartilage, Biochemical and Biophysical Research Communications, 2000, 267, 438–444.

[8] Stoop R *et al.*, Type II collagen degradation in articular cartilage fibrillation after anterior cruciate ligament transection in rats, *Osteoarthritis and Cartilage*, 2001, 9, 308–315.

[9] Price JS *et al.*, Comparison of collagenase-cleaved articular cartilage collagen in mice in the naturally occurring STR/ort model of osteoarthritis and in collagen-induced arthritis, *Osteoarthritis and Cartilage*, 2002, 10, 172–179.

[10] Bi, X. et al., Fourier transform infrared imaging and MR microscopy studies detect compositional and structural changes in cartilage in a rabbit model of osteoarthritis, *Analytical and Bioanalytical Chemistry*, 2007, 387(5), 1601–1612.

[11] Bi, X. et al., Fourier transform infrared imaging spectroscopy investigations in the pathogenesis and repair of cartilage, *BiochimicaetBiophysica Acta*. 2006, 1758, 934–941.

[12] Boskey, A. et al., FT-IR Imaging of Native and Tissue-Engineered Bone and Cartilage, Biomaterials, 2007, 28(15), 2465–2478.

Contact

*B.Sindhupakorn, tel: +66-805886686; bura@sut.ac.th

The electrostatic microwell-based microfluidic device (EµW) for cell trapping and culture: from fundamentals to applications

P. Kuntanawat[1] and R. Phatthanakun[2]

[1]King Mongkut's University of Technology Thonburi, 26 Pracha Uthit Rd., Bang Mod, Thung Khru, Bangkok 10140, Thailand

[2] Synchrotron Light Research Institute (Public Organization) 111 University Avenue, Muang District, Nakhon Ratchasima 30000, Thailand

Abstract

This paper discusses background and applications of the electrostatic microwell-based microfluidic device (EµW) for cell trapping fabricated using synchrotron based deep-X Ray lithography. The device was originally intended for fundamental single cell studies. However, its applications were also found in a large number of fields including medical studies and biotechnology. We also review our more recent progress about simplification of the technology for broader end users and commercialization of the device. The future prospect of the technology is concluded at the end.

The background

Traditional algal studies *vs* single cell studies

In the past decade, microalgae have become the central of attention in food and energy research and industry. It is well known that algal biomass is an excellent source of numerous valuable compounds such as amino acids, pigments, oligosaccharides, antioxidants and lipids [1-7] . Their high growth and production rate, diversity and hardiness [8] make microalgae an ideal food and energy crops.

The successful algal cultivation relies on fundamental knowledge about the algae. The basic biology of the algae, so far, has been primarily based on the studies on bulk scale culture (i.e. cell suspension in flasks or reactors). Investigation of the algal growth through the suspension turbidity and cell counts from collected cell suspension are usually performed. However, it is started to be realized that the traditional approaches could only reveal a part of the algal lives and, in certain cases, provide distorted information. Populations of the organisms usually exhibit an enormous range of diverse characteristics (i.e. growth pattern, rate and morphology), many of which are inhomogeneous. Using the single population growth values could falsely represent the actual algal characters [9-11].

Single cell studies have become a new trend in microbiology. The studies involve observations of each individual characters in the sample instead of the average characters of the sampled suspension. With this, not only the inhomogeneous characters of cells can be observed in detail, the dynamic biological aspects of each individual (i.e. cell life cycle, morphogenesis, reaction to chemicals) can also be studied in real time.

Microfluidic technology and single cell studies

The rise of the modern single cell studies has been accompanied by the development in microfluidic technology. This technology deals with the manipulation of small amount of fluids and particle insides, including cells [12]. This is made possible by a variety of micro- operating units such as microchannels, microvalves, micropumps and microsensors and actuators, precisely fabricated with microfabrication technology. With these key enablers, fundamental actions required in conducting chemical/biological experiments in small scale such as volume measurement, liquid droplets delivery and mixing can be accomplished. The utilization has extended towards single cell cultures. Key actions required in the microfluidic systems for single cell cultures are more specific. These include: 1) capture/confine single cells in observatory chamber and 2) perfuse the culture medium to sustain the culture. These steps have been executed through different microfluidic designed with different trapping mechanisms. The examples include electrical traps [13, 14], microcage [15], microchannel constrictions [16], suction [14], [17] and microdroplet encapsulation [9], [10], [18].

Technical problems of previous microfluidic devices for single cell studies

Although the previous studies have demonstrated different capabilities of these designs, certain technical difficulties persist. The problem is that neither of them works as a complete versatile trapping and culturing device. Most of listed mechanisms here could only capture cells of specific morphological features. The microdroplet encapsulation may be considered a versatile trap. Cells of variety of shapes and size can be captured. However the capturing versatility is traded off with users' inability to control the chemical perfusion to the culturing compartments.

With Deep X-ray Lithography using synchrotron radiation, we successfully fabricated a microfluidic device with an electrostatic microwell-based cell trapping mechanism (EµW) [19]. The device is much simpler but integrates the two necessary functionalities into one device enabling trapping of cells of diverse morphology while maintaining user flexibility to control chemical composition within the culture.

Fabrication and assembling of EµW

EµW is a transparent cell chamber of a microscope slide size with 200 microwells working as electrostatic single cell traps (Fig. 1). The detailed fabrication process and assembling can be found in our original paper [19]. In brief, EµW is assembled by bonding the following 3 layers (from bottom to top) together: a commercial positively charged microscopes slide (25x75 mm), 500 µm-thick polydimethylsiloxane (PDMS) film with 200 rectangular punched holes (width x length = 1x1 mm) and a PDMS fluidic layer. When the first 2 layer bonded together, the cell chamber's base with microwells with electrostatic bottoms are formed. The 3rd layer acts as side walls and a lid of the device. When bonded to the rest, the embedded diamond-shaped fluidic pattern at the reserve side of this layer becomes the device's flow channel enabling the cell culture media perfusion and cell loading. Injection of the liquid/suspension through the inlet located at the ends of the fluidic channel.
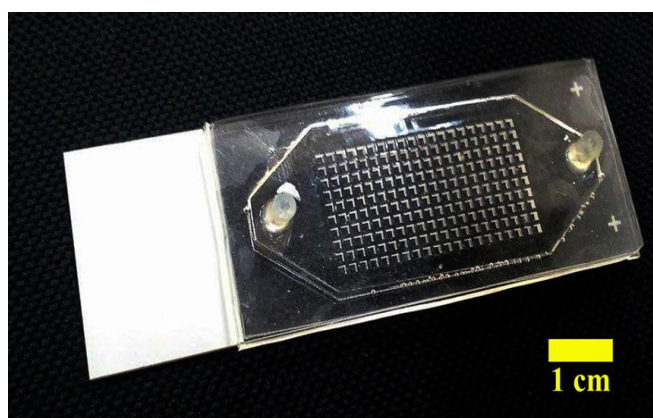
(negatively charged) are attracted by the microwells base (positively charged) through the electrostatic interaction. The suspended cells in the fluidic channel can be easily flushed away by introduction of an additional media through the inlet. The flushed liquid went through the outlet and into the waste bucket respectively. In addition, it was found that the eµW is capable of capturing cells of multiple species of different morphology and life style (i.e. adherent, non-adherent, planktonic and motile). Since addition of extra liquid to the media does replace the filled liquid and suspended particle but does not detach the trapped cells, multiple cycles of media/chemical perfusion and exchange is possible at any time during the experiment. This also means that multiple modes of cell culture (i.e. batch, continuous, semi-continuous) can be conducted in eµW without interrupting the cultured cells. These make eµW the technology that provides users with both cell trapping versatility and dynamic chemical controls, over a long period of time.

Figure 1: The fabricated electrostatic microwell-based microfluidic device (eµW). Image reprinted with permission from Suranaree J. Sci. Technol [20]

Fabrication of the PDMS layers are done with soft-lithography. The 3rd layer is obtained from molding and baking pre-hardened PDMS in a laser cut acrylic mold. However, micromold is required as a template for the fabrication of the 2nd layer. The original master mold was obtained from the deep X-ray lithographic technique using synchrotron radiation (Fig. 2). The pre-hardened PDMS was poured onto the flat area of the mold until the PDMS level reached the surface of the elevated area of the device. The baked PDMS film was peeled of the mold when hardened.

Efficiency of EµW
EµW is simple, flexible and user-friendly.

Our experiment [19, 20] has shown that by introducing cell suspension into a device filled with fresh media, cell can be automatically trapped into the microwells. The cells
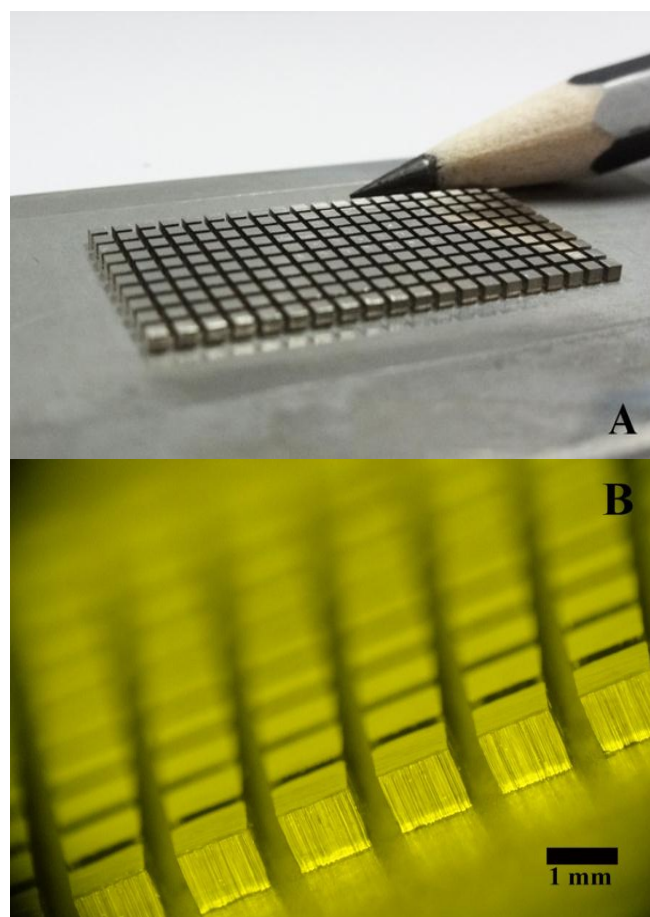

Figure 2: The original metal master mold used in fabrication of the PDMS layer with bottomless microwell pattern (A). The close of the mold reveals the rectangular blocks micropattern (B). Image reprinted with permission from Suranaree J. Sci. Technol [20].

EμW is cell compatible.

Our prolonged cell culture experiment in EμW has confirmed that the device is cell compatible [19]. Cells grown in the device have a similar growth pattern to those cultured in cell culture flask (bulk culture). This indicates that being in EμW does not interfere with natural growth of the cells. EμW is in general non-toxic to cells.

Applications and outlooks

In the past couple of years, there several attempts from our collaborators and ourselves to implement EμW in a variety of applications. The ultilizations of the device have given valuable insight into the area of studies. This includes fundamental cell studies, environmental studies, and medicals.

EμW as a cell isolation system

In addition to the use of EμW as a platform for single cell studies, we discovered that EμW can also be employed as a station for isolation and screening of microbial cells (i.e. algal cells). One of the special features of the device is that it is easy to be dissembled. The top layer of the device can be simply detached by peeling using tweezers. This exposes an array of open microwells with separated cells remained attached inside allowing users to make single cell selection. The selected cells can be transferred from the wells using micropipettes or capillary tubes to another location.

Cell isolation is the first step to the establishment of algal strain in the commercial algal cultivation. Our technology opens the door to simpler cell isolation and screening which are traditionally skill-demanding and time consuming. In other words, EμW removes the technological barrier in cell screening, which is usually exclusively performed in laboratories. It simplifies the tasks so that inexperienced and unskilled personals such as farmers, hobbyists and startup teams can accomplish the procedures themselves.

EμW in the medical study

The application of EμW has extended towards the field of medical studies. Recently, the device has been used as a platform to monitor toxicity of nanoparticles to osteoblasts [21]. Osteoblast cells were first seeded into the device filled with fresh medium. After cell attachment was established, the culture medium was replaced with a new medium with nanoparticles added. The growth and morphological changes of the cells could be monitored over time.

In this work, we have demonstrated that the use of EμW does not limit to microbial cells but also extend to mammalian cells. First, due to its small size, EμW requires much less number of cells and volume of medium to perform the experiments, in comparison to the conventional platform of microtiter plate. In addition, the microwells can be numbered and also fit the microscope field of view. This makes multiple number of cell imaging of the exact same

location possible. This is technically difficult to accomplish when the experiment is conducted using the conventional platforms such as microtiter plates and macroscopic pieces of implants. This feature is therefore of a great use in the studies where long term cell tracking is required.

Industrialization of EμW and the future prospects.

EμW is being implemented in broader applications and the number of users is getting larger as a result. Our lab scale production of the EμW could only produce 10 devices per week. To meet with the increasing demand for the devices, we are now developing the industrial prototype of the device and the production procedure. It is expected that the production rate of 1,000 devices per week will be accomplished. At the same time, the waste of the material, especially due to production failure, will be up to 3 times reduced. We are expecting that the stable and sufficient supply would not only satisfy the current usages of the device but also attract new users in different area of application such as cell isolation in large scale cell cultivation industry, biology teaching and single cell research in research institutes. Development of the industrial production of the EμW would be the starting point of introduction the innovation to the mainstream laboratory equipment market.

In addition, we had successfully developed another generation of EμW, the Do-It-Yourself (DIY) EμW. These patented ideas aim to simplify the fabrication procedures and replace the costly material (PDMS) with the cheaper unconventional material such as polymeric insect sieves and modelling clay in the fabrication. While the target users for the industrially made EμW is the laboratory scientists, the DIY EμW are designed for those who could afford less such as the new startups, farmers and armature algal cultivators. Although the structures of the devices produced are less accurate, our experiments have proven that it can be used in cell culture successfully. The material uses and procedures of the fabrication are highly simplified so that the device construction can be done at home. The technical and finical requirements are reduced for larger public in accessing the technology.

Conclusion

Our work is one of those demonstrating that fundamental studies drive technological development. Although the technology was designed to solve problems in basic studies, it uses were also found in multiple fields of applications. Commercialization and establishment of DIY EμW means that the technology could be distributed to large group of users in the future. This would not only reinforce the algal cultivation industry but also benefit the new microfarms as well as the algae-related startups. Within the global situation of foods, feeds and energy, the technology creates and distributes business opportunities, locally and globally to anyone. We hope that in the near future, our technology could help create jobs, innovation-based businesses and so the nation competitiveness at the global level.

References

[1] K. H. Ogbonda *et al.*, Influence of temperature and pH on biomass production and protein biosynthesis in a putative Spirulina sp, *Bioresour. Technol.*, 2007, 98(11), 2207-2211.

[2] L. M. Colla *et al.*, Production of biomass and nutraceutical compounds by Spirulina platensis under different temperature and nitrogen regimes, *Bioresour. Technol.*, 2007,98(7), 1489-1493.

[3] M. A. C. L. de Oliveira *et al.*, Growth and chemical composition of Spirulina maxima and Spirulina platensis biomass at different temperatures, *Aquac. Int.*, 1999, 5221, 261-275.

[4] S. T. Silveira *et al.*, Optimization of phycocyanin extraction from Spirulina platensis using factorial design., *Bioresour. Technol.*, 2007, 98(8), 1629-1634.

[5] C. D. O. Rangel-Yagui *et al.*,Chlorophyll production from Spirulina platensis: cultivation with urea addition by fed-batch process, *Bioresour. Technol.*, 2004, 92(2), 133-141. vol.

[6] H. Berberoglu *et al.*, Radiation characteristics of Botryococcus braunii, Chlorococcum littorale, and Chlorella sp. used for fixation and biofuel production, *J. Quant. Spectrosc. Radiat. Transf.*, 2009, 110(17), 1879-1893.

[7] A. Hongsthong *et al.*, Revealing differentially expressed proteins in two morphological forms of Spirulina platensis by proteomic analysis, *Mol. Biotechnol.*, 2007, 36(2), 123-130.

[8] Q. Hu *et al.*, Microalgal triacylglycerols as feedstocks for biofuel production: perspectives and advances., *Plant J.*, 2008, 54(4), 621-639.

[9] A. Dewan *et al.*, Growth kinetics of microalgae in microfluidic static droplet arrays., *Biotechnol. Bioeng.*, 2012, 109(12), 2987-2996.

[10] J. Pan *et al.*, Quantitative tracking of the growth of individual algal cells in microdroplet compartments, *Integr. Biol.*, 2011, 3(10), 1043-1051.

[11] D. B. Weibel *et al.*, Microfabrication meets microbiology, *Nat. Rev. Microbiol.*, 2007, 5(3), 209-218.

[12] C. Beck *et al.*, Microfluidics in Single Cell Analysis, in *Advances in Microfluidics*, R. T. Kelly, Ed. Rijeka, Croatia: InTech, 2012, 173–192.

[13] C. Suscillon *et al.*, Alternating current-dielectrophoresis driven on-chip collection and chaining of green microalgae in freshwaters, *Biomicrofluidics*, 2013, 7(2), 24109.

[14] Z. Zhu *et al.*, Microfluidic single-cell cultivation chip with controllable immobilization and selective release of yeast cells., *Lab Chip*, 2012, 12(5), 906-915.

[15] P. B. Lillehoj *et al.*, A microfluidic device for single and small population cell trapping and lysis of Pseudo-nitzschia, in *2010 IEEE 5th International Conference on Nano/Micro Engineered and Molecular Systems*, 2010, 975–978.

[16] A. C. Rowat *et al.*, Tracking lineages of single cells in lines using a microfluidic device., *Proc. Natl. Acad. Sci. U. S. A.*,Oct 2009, 106(43), 18149-18154.

[17] S. Cui *et al.*, A microfluidic chip for highly efficient cell capturing and pairing, *Biomicrofluidics*, 2011, 5(3), 32003-320038.

[18] J. Clausell-Tormos *et al.*, Droplet-based microfluidic platforms for the encapsulation and screening of Mammalian cells and multicellular organisms., *Chem. Biol.*, May 2008, 15(5), 427-437.

[19] P. Kuntanawat *et al.*, An electrostatic microwell–based biochip for phytoplanktonic cell trapping, *Biomicrofluidics*, 2014, 8(3), 34108.

[20] P. Kuntanawat *et al.*, Disposable vs reusable : practical aspects from end users and reusability test of the biochip for electrostatic microwell-based single cell trapping and culturing, 2015, 22(3), 243-252.

[21] A. Ramdongbang *et al.*, Increased Osteoblast Growth with Graphene Oxide in a Microwell-Based Biochip, in *2016 9th Biomedical Engineering International Conference (BMEiCON)*, 2016, 1–5.

Contact

*P. Kuntanawat; panwong.kun@mail.kmutt.ac.th

Synchrotron-based S K-edge XANES spectroscopy reveals increasing oxidation state of sulfur in soil organic matter with advanced decomposition status

J. Prietzel*

Chair of Soil Science, Technical University of Munich, Germany

Abstract

Sulfur K-edge XANES spectroscopy was performed at BL 8 of Synchrotron Light Research Institute, Thailand on samples of humus-rich topsoil horizons in forest soils of the German Alps showed a systematic increase of oxidized S forms at the expense of reduced organic S forms with increasing soil organic matter (SOM) age and decomposition status. This change provides insight into chemical as well as structural SOM changes with increasing decomposition status, which may help to explain changes in soil nutrient (S) and water availability; moreover, it can be used to assess the SOM balance of soils.

Introduction

Probably caused by climate change, forest soils in the German Alps are currently losing soil organic matter (SOM), resulting in significant depletion of their SOM stocks during recent decades [1]. This loss is associated with conversion of soil carbon into atmospheric CO_2, thus accelerating climate warming, but also with decreased water and nutrient availability for plants and mountain forests.

Thus, forest ecologists aim at developing adequate forest management strategies to counteract the ongoing SOM loss and – wherever possible – reverse SOM losses into gains. The basis for the development of such management approaches is a thorough understanding of the SOM chemistry in the respective soils. This includes detailed knowledge of the key binding patterns of the SOM core C atoms with those of other important elements like N or S. Synchrotron-based S K-edge XANES spectroscopy offers an excellent opportunity to study the S speciation of soils and SOM [2-6]. We therefore applied this technique on soils of German mountain forests with different SOM dynamics.

Materials and methods

We investigated soil samples obtained from surface layers (L, Of, Oh) and mineral topsoil (Ah) horizons ofdifferent forest soils in the German Alps which have experienced either recent SOM losses or gains (Fig. 1). For all samples, the S speciation was investigated by S K-edge XANES spectroscopy in the energy range between 2450 and 2600 eV at BL 8 of SLRI, using the method described in detail before [5,6]. In numerous earlier studies (e.g. [5,6], BL 8 has proven its ability to allow the acquisition of a large number of precise and accurate XANES spectra at the S K-edge within a short time. This makes BL8 particularly apt of soil S speciation study.

Figure 1: Adjacent forest stands (upper panels) and soils (lower panels) at study site Seinsberg (Karwendel Mts., Germany) with recently decreasing (left: "Seinsberg O") and increasing (right; "Seinsberg Z") SOM stocks.

Results and discussion

As indicated by the S K-edge XANES spectra (Fig. 2), allstudied soils showed a systematic change of S speciation with soil depth and concomitantly increased SOM age and decomposition status: In the sequence L, Of, Oh, Ah horizon, the contribution of oxidized S forms (sul-fones, sulfonates, organic and inorganic sulfate) to total S increased at the expense of reduced organic S forms (thiols, organic sulfides and disulfides) (Fig. 2). Moreover, the uppermost forest floor (L, Of) horizons, where the youngest and least humified SOM were located, always were characterized by considerably larger portions of sulfoxide S than the Oh and Ah horizons below, where the SOM was more decom-posed. Obviously progressive transformation of litter into well-humified SOM was associated with a systematic conver-sion of sulfoxide, and at later stages predominantly reduced organic S species (thiols, organic mono- and disulfides) into oxidized organic and inorganic S forms.
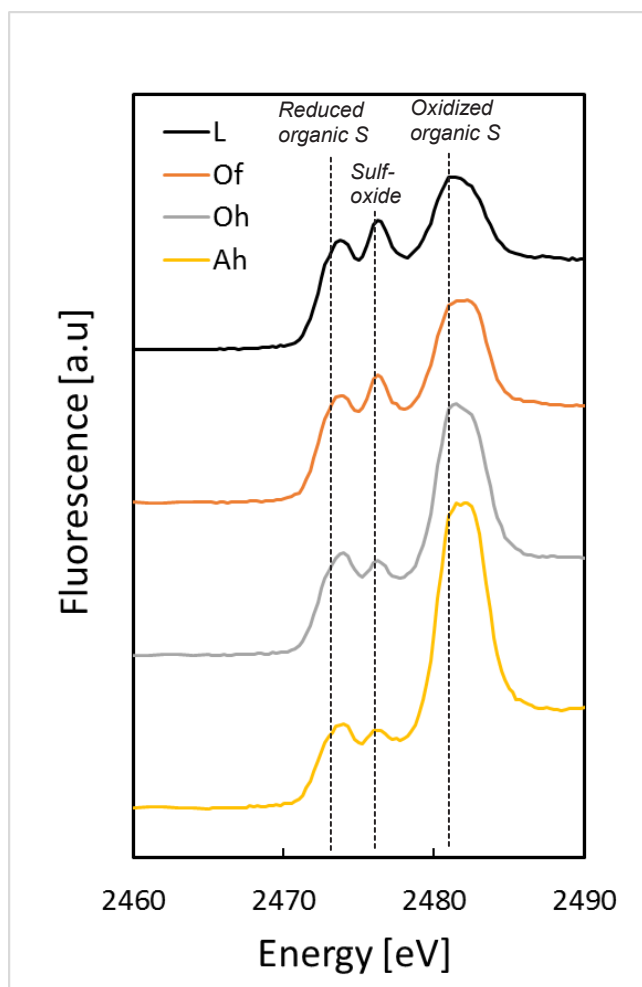
Figure 2: Sulfur K-edge XANES spectra of samples from different horizons in a soil profile at site Seinsberg Z.

When identical horizons of soils with recently and/or currently increasing *vs.* decreasing SOM stocks were compared with each other with respect to their S speciation, it became evident that soils with decreasing SOM stocks were generally characterized by a larger percentage of more oxidized S compounds, *i.e.* an increased mean oxidation state of soil S (MOS; [3]) than soils with a currently increasing SOM stock (Fig. 3). The S speciation thus mirrors an – on average – more advanced humification and SOM decomposition status in the soil with decreasing compared to increasing SOM stocks, in line with the results reported for the sequence of soil horizons with increasing soil age and humus degradation reported above.

References

[1] J. Prietzel *et al*.,Organic matter losses of German Alps forest soils since the 1970s most likely caused by warming, *Nature Geoscience,* 2016, 9, 543-548.

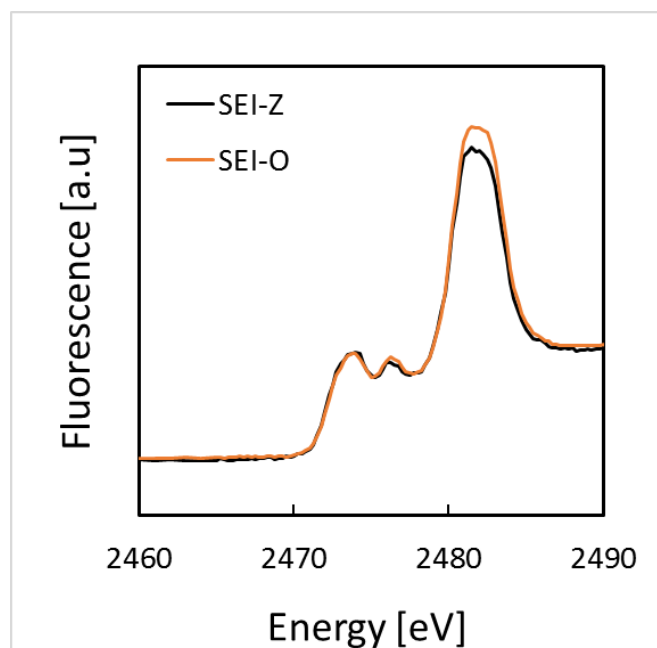[2] J. Prietzel *et al*., Speciation of sulphur in soils and soil

Figure 3: Sulfur K-edge XANES spectra of samples from the Ah horizon of soil profiles with decreasing (Seinsberg O) and increasing (Seinsberg Z) SOM stocks.

particles by X-ray spectromicroscopy,*Europ. J. Soil Sci.,* 2003, 54, 422-432.

[3] J. Prietzel *et al*., Sulfur K-edge X-ray absorption near edge fine structure spectroscopy reveals differences in sulfur speciation of bulk soils, humic acid, fulvic acid, and particle size separates, *Soil Biol. Biochem.,* 2007, 39, 877-890.

[4] J. Prietzel *et al*., Anoxic versus oxic sample pre-treatment: Effects on the speciation of sulfur and iron in well-aerated and wetland soils as assessed by X-ray absorption near-edge spectroscopy (XANES), *Geoderma,* 2009, 153, 318-330.

[5] J. Prietzel *et al*., Sulfur speciation in soil by S K-edge XANES spectroscopy: Comparison of spectral deconvolution and Linear combination fitting, *Environ. Sci. & Technol.,* 2011, 45, 2878-2886.

[6] J. Prietzel *et al*., Sulfur speciation in two glacier foreland soil chronosequences assessed by S K-edge XANES spectroscopy, *Eur. J. Soil Sci.,* 2013*, 64,* 260-272.

Contact

*J. Prietzel, tel: +49-8161714734; prietzel@wzw.tum.de

Role of chlorophyll in *Spirulina* on photocatalytic activity of CO_2 reduction under visible light over modified N-doped TiO_2 photocatalysts

T. Phongamwong, M. Chareonpanich and J. Limtrakul

Kasetsart University, 50 Ngam Wong Wan Rd., Ladyaow, Chatuchak, Bangkok 10900, Thailand

Introduction

The combination of TiO_2 nanoparticles and chlorophyllmolecules is promising to provide potential new composite materials for improving CO_2 photoreduction. In this research, chlorophyll in *Spirulina* modified on N-doped TiO_2 catalysts (Sp/N-TiO_2) were synthesized with an attempt to enhance the photocatalytic efficiency. The effects of nitrogen and chlorophyll in *Spirulina* on CO_2 photoreduction with water under visible light of Sp/N-TiO_2 were investigated by using the experimental system show in Fig. 1.
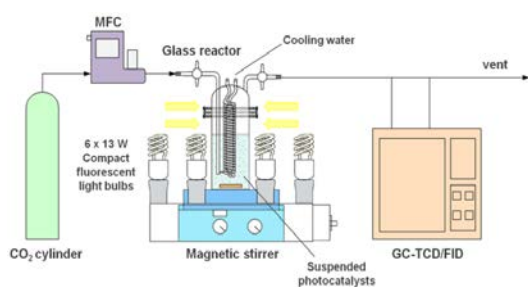

Figure 1: Schematic of experimental system for CO_2 photoreduction.

As shown in Fig. 2, the normalized Ti K-edge XANES spectra, carried out at BL8 of the SLRI, evidently confirmed the existence of anatase phase of all catalysts.N 1S XPS spectra in Fig. 3, carried out at BL3.2a of the SLRI, confirmed the present of nitrogen dopantsin the form of interstitial N in TiO_2 lattice which were responsible for the increase in visible light activity of the N-TiO_2 catalysts. It was found that approximately 2.91 at % of nitrogen was successfully doped onto the 10N-TiO_2 catalyst. In addition, Ti 2p XPS spectra exhibited an occurrence of Ti^{3+} oxidation state and oxygen vacancies (V_0) on the surface of TiO_2 catalysts acted as the active adsorption sites of reactants and intermediates. The survey spectrum of 0.5Sp/10N-TiO_2 also exhibited the expose of *Spirulina* on the catalysts to light irradiation.

Regarding the catalytic performances of CO_2 photoreduction, the activities of catalysts were in the order of undoped TiO_2 < N-TiO_2 < Sp/N-TiO_2. The outstanding photocatalytic activity of Sp/N-TiO_2 could be attributed to the enhancement in visible light harvesting, surface V_0, and the synergistic effect between N-TiO_2 and chlorophyll in *Spirulina*. Nevertheless, the addition of *Spirulina* was found to improve the catalytic stability and C^{2+} (C_2H_4 and C_2H_6) product selectivity. Accordingly, the possible reaction mechanism of CO_2 reduction for the formation of hydrogen and hydrocarbon products in this present work is illustrated in Fig. 4.
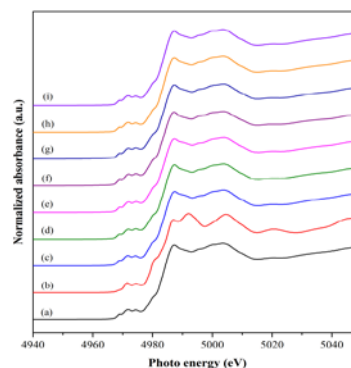

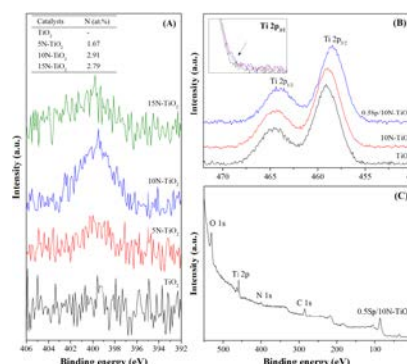*Figure 2: Normalized Ti K-edge XANES spectra of (a) anatase, (b) rutile, (c) TiO_2, and (d)-(i) modified TiO_2.*

Figure 3: High resolution XPS spectra of (A) N 1s, (B) Ti 2p of modified TiO_2 catalysts, and (c) survey spectrum of 0.5Sp/10N-TiO_2 catalyst.
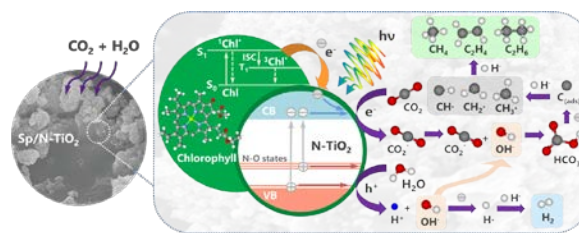

Figure 4: Proposed mechanism for photoreduction of CO_2 with water on Spirulina modified N-TiO_2 catalyst.

References

[1] T. Phongamwong *et al.*, *Applied Catalysis B: Environmental 168*, 2015, 114-124.

Contact

*M. Chareonpanich, tel: +66-2579-2083; fengmtc@ku.ac.th

Green and sustainable production of energy and chemical feedstock from CO_2 via innovative integrated magnetic field packed-bed catalytic reactors

W. Donphai[1], T. Witoon[1], S. Kiatphuengporn[2], Y. Poo-arporn[3], W. Limphirat[3], P. Jantaratana[4], J. Limtrakul[5] and M. Chareonpanich[1]

[1]KU-Green Catalysts Group, Department of Chemical Engineering, Faculty of Engineering, Kasetsart University, 50 Ngam Wong Wan Rd., Ladyaow, Chatuchak, Bangkok 10900, Thailand

[2]National Science and Technology Development Agency, 111 Thailand Science Park, Phaholyothin Rd., Khlong Luang, Pathum Thani 12120, Thailand

[3]Synchrotron Light Research Institute (Public Organization), 111 University Avenue, Muang District, Nakhon Ratchasima 30000, Thailand

[4]Department of Physics, Faculty of Science, Kasetsart University, 50 Ngam Wong Wan Rd., Ladyaow, Chatuchak, Bangkok 10900, Thailand

[5]Department of Materials Science and Engineering, Vidyasirimedhi Institute of Science and Technology, 555 Moo 1 Payupnai, Wangchan, Rayong 21210, Thailand

Abstract

Based on green and sustainable innovation with efficient utilization concepts for enhancement of catalyst performance and energy conservation, an external magnetic field was applied in CO_2 hydrogenation reaction over 3 series of catalysts (Cu-ZnO/ZrO2, xFe/MCM-41, and Cu-Fe/MCM-41). With the external magnetic field, the selective production of C^{2+} hydrocarbons and small alcohols were observed at significantly lower temperatures at the same reaction rate. The external magnetic field facilitated adsorption of CO_2 molecules over the surface of magnetized catalysts, leading to the decrease of apparent activation energy, operating temperature, and the simultaneous decrease of CO_2 emission by means of energy-efficient process modification.

Introduction

CO_2 hydrogenation reaction is considered as one of the most effective ways to approach the environmentally friendly synthesis of sustainable chemical feedstock and fuels. The previous works in CO_2 hydrogenation have been mainly focused on the key factors affecting the catalytic activity and product selectivity including – types of reactors [1, 2], metal catalysts and supports [3–5], promoters [3, 6], operating conditions [3, 4], and active sites [7, 8].
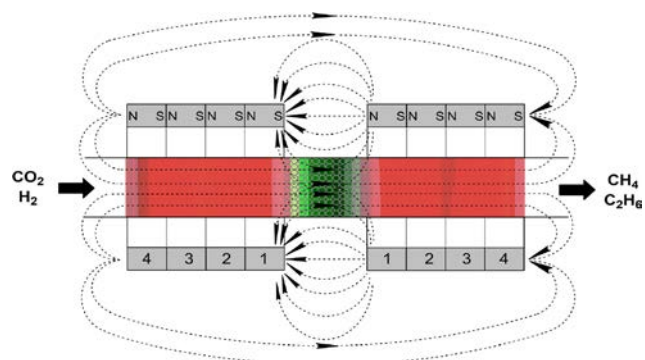

Figure 1: Magnetic lines of force and gradient of magnetic field intensity of four pairs of magnets positioned over a catalytic packed-bed reactor.

Magnetic files-assisted reaction

In this present work, an external magnetic field has been applied onto the catalytic packed-bed reactor (Fig. 1) with sustainable and efficient utilization concepts in catalytic CO_2 hydrogenation reaction for the enhancement of catalyst performance and energy conservation over 3 series of catalysts. Accordingly, in the 1st series of this study [10] – the performances of Cu-ZnO/ZrO2 catalyst under magnetic field with different magnetic flux intensities (0, 20.8, and 27.7 mT) and orientations (north-to-south (N-S) and south-to-north (S-N) directions) in CO_2 hydrogenation were investigated. The catalysts operated under magnetic field gave higher CO_2 conversions, compared none magnetic field at all reaction temperatures. The highest CO_2 conversions were obtained under the magnetic field condition at 20.8 mT in S-N direction (Table 1) which was 1.8-3.0 times higher than none magnetic field. In addition, it was found that the operating temperatures were significantly lower than samples without magnetic field at the same reaction rate.

Table 1: Apparent activation energy of Cu-ZnO/ZrO2catalysts in CO_2 hydrogenation reaction at different magnetic intensities and orientations.

Conditions	Apparent activation energy (kJ/mol)
No magnetic field	50.68
20.8 mT _N-S	49.23
20.8 mT _S-N	27.18
27.7 mT _N-S	40.53
27.7 mT _S-N	37.35

[a] Calculated from CO_2-TPD profile

In the 2nd series of this study [11], effects of magnetic field orientation and intensity on activity and selectivity of xFe/MCM-41 catalysts with ferrimagnetic property were investigated. With magnetic field, especially in north-to-south (N-S) direction, CO_2 conversions were significantly improved by 1.5-1.8 times; meanwhile the activation energy was decreased by 1.12-1.15 times, compared zero magnetic field.

Upon changing the intensity, CO_2 conversion increased with increasing the intensity followed the order of 27.7 mT > 25.1 mT > 20.8 mT. Furthermore, it was found that the higher selectivities to C_2-C_3 hydrocarbons (2.5–5.3 times), and CH_3OH (1.6 times) were observed at 180–200°C and 220°C, respectively. Among all the conditions with magnetic field, the highest CO_2 conversion and selectivity to CH_3OH and C_2-C_3 hydrocarbons were obtained at -27.7 mT in N-S direction. The reaction pathways for CO_2 hydrogenation over xFe/MCM-41 catalysts were proposed as shown in Fig. 2. Without magnetic field, methane and carbon monoxide were mainly produced. On contrary, C^{2+} hydrocarbons were selectively produced under magnetic field. These benefits might be due to the improvement of active metal with ferro/ferrimagnetic property, the increase of the reactants adsorbed on magnetized Fe surface, and the direction-specific chemisorption-surface reaction over magnetized Fe surfaces of the catalysts, especially in the case of the N—S magnetic flux direction.
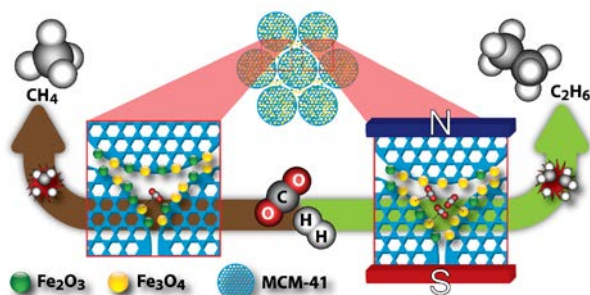

Figure 2: Proposed reaction pathways for CO_2 hydrogenation over xFe/MCM-41 catalysts.

In the 3rd series of this study [12], the external magnetic field was found to significantly improve the CO_2 conversion over Cu-Fe/MCM-41 catalysts at all reaction temperatures. The highest CO_2 conversion was obtained over 10(Cu)-10(Fe)/MCM-41 catalyst with magnetic flux density of – 27.7 mT in N–S direction which was 1.8 times higher than that of without magnetic field. The methanol space time yield was 1.5 times higher than that of without magnetic field.

The lowest apparent activation energies over 10(Cu)/MCM-41, 10(Fe)/MCM-41, and 10(Fe)-10(Cu)/MCM-41 catalysts were 37.6 kJ/mol, 41.6 kJ/mol, and 34.5 kJ/mol which were 16%, 13%, and 18% lower than those of without magnetic field at the same conditions with the highest CO_2 conversion, respectively.

In addition to the CO_2 conversion and methanol space time yield obtained under magnetic field, the local geometry changes of Fe species in catalysts during reduction stage with hydrogen gas at 25-480°C and holding stage at 480°C for 3 hours were investigated by time-resolved X-ray absorption spectroscopy (TRXAS) at beamline 2.2 of the SLRI, Thailand. XANES spectra of Fe K-edge were collected in the energy range of 6975-7525 eV in the

transmission detection mode using ionization chamber. The *in-situ* XANES measurements were reported as the normalized Fe K-edge absorption spectra to confirm the transformation of Fe oxide species in xFe/MCM-41 catalysts. The result indicated that the spectra of Fe oxide species in xFe/MCM-41 catalysts were changed due to the phase transformation during reduction process (Fig. 3).
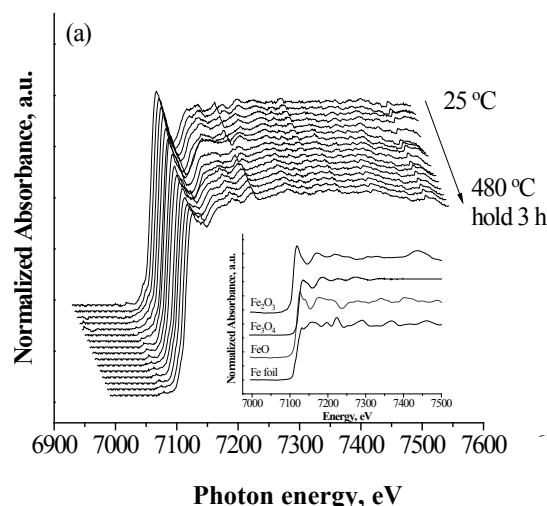

Figure 3: Normalized Fe K-edge XANES spectra of 10(Fe)/MCM-41 measured during reduction in H_2 at room temperature to 480 °C and holding for 3 hours.

As a result, this integrated magnetic field-packed bed reactor could significantly reduce the operating temperatures by approximately 33, 34, and 58 °C over 10(Cu)/MCM-41, 10(Fe)/MCM-41, and 10(Fe)-10(Cu)/MCM-41 catalysts, respectively compared none magnetic field at the reaction temperature of 260 °C. Based on CO_2 conversion of 100 kg/h, with 10(Fe)-10(Cu)/MCM-41 catalyst (the best catalyst in this series of study), magnetic field could save electric energy costs of approximately 48,000 \$/year with payback periods of 0.2 years at the reaction temperature of 260°C.

Summary

From these series of green and sustainable production of energy and chemical feedstock from CO_2 via integrated magnetic field packed-bed catalytic reactor, these outstanding catalytic performances could be attributed to fact that the external magnetic field facilitates and promotes the adsorption of CO_2 reactant gas molecules over the surface of magnetized catalysts, leading to the decrease of apparent activation energy and the operating temperature, and the simultaneous decrease of CO_2 emission by means of energy-efficient process modification. Interestingly, the increase of selectivities to hydrocarbon and small alcohol products were also observed. Thus, the challenge in application of magnetic field in CO_2 hydrogenation process helps reduce CO_2 emission into the atmosphere compared to

the convention reactor, and therefore leads to the carbon-neutral CO_2 conversion process. The magnetic field-assisted fixed bed reactor system is of great beneficial in the future chemical and petrochemical processes for green and sustainable production. The concept and potential use of this reactor, here begun with CO_2 conversion reaction, will be further expanded to other chemical productions in our future work.

Acknowledgements

References

[1] S.H. Kang *et al.*, Catalytic performance on iron-based Fischer-Tropsch catalyst in fixed-bed and bubbling fluidized-bed reactor, *Appl. Catal. B*, 2011, 103, 169–180.

[2] A. Montebelli *et al.*, Optimization of compact multitubular fixed-bed reactors for the methanol synthesis loaded with highly conductive structured catalysts, *Chem. Eng. J.*, 2014, 255, 257–265.

[3] K.A. Ali *et al.*, Recent development in catalytic technologies for methanol synthesis from renewable sources: a critical review, *Renew. Sustain. Energy Rev.*, 2015, 44,508–518.

[4] S. Saeidi *et al.*, Hydrogenation of CO_2 to value-added products—a review and potential future developments, *J. CO_2 Util.*, 2014, 5, 66–81.

[5] J. Fontana *et al.*, Support effect over bimetallic ruthenium–promoter catalysts in hydrogenation reactions, *Chem. Eng. J.*, 2010, 165, 336–346.

[6] A. Bansode *et al.*, Impact of K and Ba promoters on CO_2 hydrogenation over Cu/Al_2O_3 catalysts at high pressure, *Catal. Sci. Technol.*, 2013, 3, 767–778.

[7] D. Gao *et al.*, Coupling reaction between ethanol dehydrogenation and maleic anhydride hydrogenation catalyzed by Cu/Al_2O_3, Cu/ZrO_2, and Cu/ZnO catalysts, *Chem. Eng. J.*, 2013, 233, 349–359.

[8] P. Dumrongbunditkul *et al.*, Preparation and characterization of $Co–Cu–ZrO_2$ nanomaterials and their catalytic activity in CO_2 methanation, *Ceramics International*, 2016, 42, 10444–10451.

[9] T. Phongamwong *et al.*, CO_2 hydrogenation to methanol over $CuO–ZnO–ZrO_2–SiO_2$ catalysts: Effects of SiO_2 contents, *Chem. Eng. J.*, 2017, 316, 692–703.

[10] W. Donphai *et al.*, Effect of magnetic field on CO_2 conversion over $Cu-ZnO/ZrO_2$ catalyst in hydrogenation reaction, *J. CO_2 Util.*, 2016, 16, 204–211.

[11] S. Kiatphuengporn *et al.*, Magnetic field-enhanced catalytic CO_2 hydrogenation and selective conversion to light hydrocarbons over Fe/MCM-41 catalysts, *Chem. Eng. J.*, 2016, 306, 866–875.

[12] S. Kiatphuengporn *et al.*, Cleaner production of methanol from carbon dioxide over copper and iron supported MCM-41 catalysts using innovative integrated magnetic field-packed bed reactor, *J. Clean. Pro.*, 2017, 142, 1222-1233.

Contact

*M. Chareonpanich, tel: +66-2579-2083; fengmtc@ku.ac.th

Atomic structure of magnesium ferrite nanoparticles prepared by combustion method

N. Thanh[1]*, T. T. Loan [1], S. Soontaranon[2], H. M. Chung [3] and N. P. Duong[1]

[1]International Training Institute for Materials Science (ITIMS), Hanoi University of Science and Technology, Hanoi, Vienam
[2]Synchrotron Light Research Institute (Public Organization), 111 University Avenue, Muang District, Nakhon Ratchasima 30000, Thailand
[3]Thai Nguyen University of Technology, Thai Nguyen, Vienam

Abstract

The $MgFe_2O_4$ nanoparticles were synthesized by using combustion method and annealed at different temperature (T_a = 500 °C, 750 °C and 1000 °C). The structural information of the samples including lattice parameter, coordinates of atoms, crystallite size, lattice micro strain, and cation distribution have been determined from synchrotron X-ray diffraction data by using Rietveld refinement method. The refinement result revealed that all the samples have mixed spinel structure in which the concentration of Mg^{2+} ions in tetrahedral site increases with increasing of annealing temperature. The influence of the cation distribution on the lattice parameter has been indicated. The obtained results were discussed and compared with the reported data.

Introduction

Spinel ferrite nanoparticles are of great interest due to their potential applications and novel properties. Besides the conventional applications such as transformer cores in high frequency power supplies, microwave devices, high density magnetic recording etc., applications of these materials are diverging to new fields like medical diagnostics, site specific drug delivery, magnetic refrigeration, ferrofluids, and gas sensing [1-3]. Spinel ferrites are exemplified by the formula AB_2O_4 where A (tetrahedral site) and B (octahedral site) are cations [4]. The distribution of cations over tetrahedral and octahedral sites strongly effectson the magnetic properties of spinel ferrites [5].

Magnesium ferrite is one of the most important spinel ferrites with wide applications in many fields including microwave devices, electromagnets, hyperthermia, heterogeneous catalysis, sensor technology and photocatalyst [6-9]. $MgFe_2O_4$ is known to be a partially inverse spinel that can be written as $(Mg_xFe_{1-x})_A[Mg_{1-x}Fe_{1+x}]_BO_4$, where $(Mg_xFe_{1-x})_A$ and $[Mg_{1-x}Fe_{1+x}]_B$ represent, respectively, the tetrahedral (A) and octahedral [B] sites of the spinel-type structure. The fraction of Fe^{3+} cations occupied in tetrahedral site (1-x) is the so-called inversion parameter [10]. In the bulk $MgFe_2O_4$ material, the inversion parameter was observed to be close to 0.9 [11]. In nanostructured Mg-ferrite, it was reported that the inversion parameter can reach to a value of 0.64 [10] and the cation distribution has been indicated to strongly depend on preparation methods and heat-treatment conditions [12-14].

With desire to enhance the magnetic moment of the magnesium ferrite via varying its cation distribution, we have prepared the $MgFe_2O_4$ nanoparticles by using combustion method and annealed at different temperature (T_a = 500 °C, 750 °C and 1000 °C). However, a good understanding of the magnetic properties of the nanoparticles requires detailed knowledge of its atomic structure including crystal structure and cation distribution. Such detailed structural information can be obtained by diffraction technique.

In this paper, we present the results studied on atomic structure of the $MgFe_2O_4$ nanoparticles by using synchrotron X-ray diffraction (SXRD). The cation distribution and other structural parameters were obtained from SXRD data on applying the full pattern fitting of Rietveld refinement method.

Experimental

Synthesis

The $MgFe_2O_4$ nanoparticles were synthesized by using combustion method. The solution of NaOH 0.8 M was heated up to 70 °C with vigorously stirring. Stearic acid was added to the hot alkaline solution to make saponification reaction. The solution of prepared sodium stearate was kept in 70 °C with continuously stirring to avoid condensation. The mixed solution of $Mg(NO_3)_2$ 0.1 M and $Fe(NO_3)_3$ 0.2 M was prepared from the salts $Mg(NO_3)_2.6H_2O$ and $Fe(NO_3)_3.9H_2O$, then added to the sodium stearate solution. A reddish-brown precipitate in the colloidal form was obtained from this reaction. Precipitate was washed by deionized water until pH = 7. The precipitate was collected and dried at 100 °C for 24h. The as-synthesized powders were combusted of at 400 °C and annealed at various temperatures (500 °C, 750 °C and 1000 °C) during 5h. After then, the as-prepared samples were immediately quenched from that high temperature into ice-melting water. Nanoparticles were obtained by a permanent magnet and drying at 60 °C for 5h.

SXRD measurements

Synchrotron X-ray powder diffraction (SXRD) experiments were carried out at beamline BL1.3W Small/Wide Angle X-ray Scattering (SAXS/WAXS) of the Synchrotron Light Research Institute, Thailand (λ = 1.55 Å) at room temperature [15]. The data were processed to be analyze using the Rietveld method with the help of FullProf program [16]. The diffraction peaks were modeled by pseudo-Voight function. A standard of LaB_6 was used to determine instrument broadening. The refinement fitting quality was checked by goodness of fit (χ^2) and weighted profile R-factor (R_{wp}) [17].

Result and discussion

Fig. 1 shows the SXRD patterns of the $MgFe_2O_4$ samples annealed at different temperatures. All the diffraction peaks correspond to the cubic spinel structure confirming the formation of phase-pure spinel ferrite in the samples.

The structural parameters of the samples were well refined via Rietveld analysis using the standard model of spinel ferrite within the cubic symmetry (space group $Fd3m$) with atoms in positions A-site in $8a$(1/8, 1/8, 1/8), B-site in $16d$(1/2, 1/2, 1/2) and O in $32e$(x, x, x). One of the synchrotron diffraction patterns and its Rietveld refinement are shown in Fig. 2. The refined values of structural parameters including lattice constant (a), unit cell volume (V), oxygen positional parameter (x(O)), average size of coherent scattering region (D) and lattice microstrain ($\Delta a/a$) are given in Table 1. The average size of coherent scattering region D (usually called the crystallite size) and lattice microstrain $\Delta a/a$ (where a is lattice constant) were obtained by analysis of the peak broadening on applying Rietveld method using FullProf program with the instrumental resolution function identified by SXRD analysis of the LaB_6 standard.

As seen in Table 1, the crystallite size distributed in nano-scale from 11 to 41 nm and increased with increasing of annealing temperature. This increase could be explained by the improved crystallinity and promoted particles size of the samples at higher annealing temperatures due to better atomic diffusion as observed in other spinel ferrite nanoparticle systems [18, 19].

The lattice microstrain allows us to characterize the structure disorder of the samples. As known, the higher T_a, the better crystallinity, the structure must be more order [20], and hence, the $\Delta a/a$ value is expected to decrease with increasing of annealing temperature. But an increase of the lattice microstrain with T_a increasing was observed. This result reveals the influence of quenching process on the structure ordering since the sample quenched from higher annealing temperature corresponds to more disordered structure.

Table 1: Structural parameters of the $MgFe_2O_4$ samples estimated from SXRD analysis: Lattice parameter (a), unit cell volume (V), oxygen coordinate (x(O)), average crystallite size (D), average value of microstrain (Δa/a), and the refinement fitting quality. Statistical errors are indicated in the last significant digit.

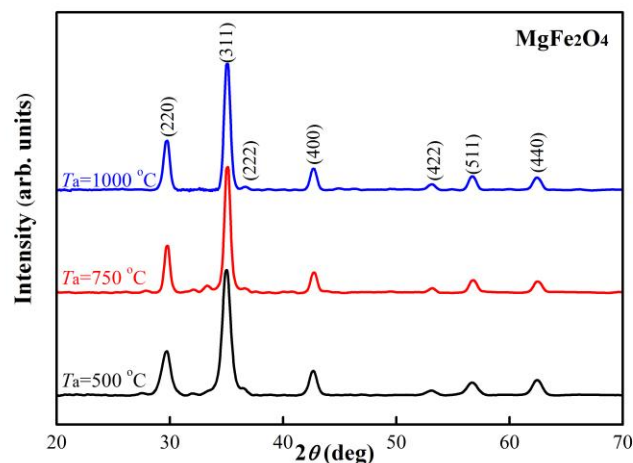| T_a	500°C	750°C	1000°C
a, Å	8.3953(9)	8.4044	8.4209(8)
V, Å^3	591.71(1)	593.64(2)	597.99(1)
x(O)	0.2522(9)	0.2558(8)	0.2538(7)
D, nm	11.2(1)	14.3(1)	40.9(1)
$\Delta a/a$	0.0015(1)	0.0036(2)	0.0039(1)
χ^2	1.28	1.31	1.57
R_{wp}, %	10.1	13.2	15.2

Figure 1: Synchrotron X-ray diffraction patterns of the $MgFe_2O_4$ samples annealed at different temperatures.
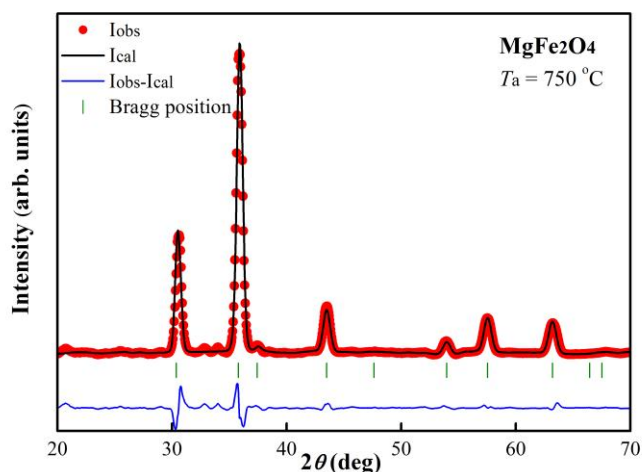

Figure 2: Synchrotron diffraction pattern of the $MgFe_2O_4$ sample annealed at 750 °C and processed by the Rietveld method. The experimental points as well as calculated and difference functions are indicated.

The obtained values of lattice parameter were higher than the value of bulk $MgFe_2O_4$ (a^{bulk} = 8.367 Å [21]) but comparable to those reported previously for $MgFe_2O_4$ nanoparticles [22, 23]. The lattice parameter was also found to increase with increasing of annealing temperature (see Fig. 3). This result was in good agreement with previous studies on quenched magnesium ferrite and could be explained by the distribution of Mg^{2+} and Fe^{3+} ions over tetrahedral and octahedral sites [20, 24].

The cation distribution of the samples was determined by analyzing the SXRD data using the Rietveld refinement method. Although only the Fe occupancy could be exactly determined by SXRD, since iron scatters X-rays much more strongly than magnesium [25], but due to the balance of the Fe ions fraction in [B] site with the fraction of Mg ions in (A) site, the distribution of Mg^{2+} and Fe^{3+} ions in (A) and [B] sites was reliably estimated and given in Table 2.

Table 2: Cation distribution of the MgFe$_2$O$_4$ samples.

T_a	500 °C	750 °C	1000 °C
A-site	Mg$_{0.159}$Fe$_{0.841}$	Mg$_{0.165}$Fe$_{0.835}$	Mg$_{0.234}$Fe$_{0.766}$
B-site	Mg$_{0.841}$Fe$_{1.159}$	Mg$_{0.835}$Fe$_{1.165}$	Mg$_{0.766}$Fe$_{1.234}$

As seen in Table 2, all the samples had mixed spinel structure in which Mg^{2+} and Fe^{3+} ions distribute in both tetrahedral and octahedral sites. The increase of the Mg^{2+} ions concentration in (A) site with increasing of annealing temperature led to the increase of lattice parameter (see Fig. 3) which could be explained due to larger ionic radii of Mg^{2+} ion compared to that of Fe^{3+} (r$_{Mg}^{2+}$ = 0.71 Å, r$_{Fe}^{3+}$ = 0.63 Å for tetrahedral site and r$_{Mg}^{2+}$ = 0.86 Å, r$_{Fe}^{3+}$ = 0.785 Å for octahedral site) [20, 26].
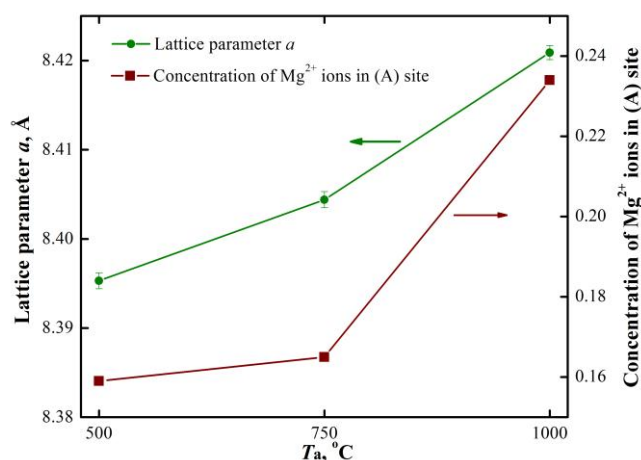

Figure 3: Lattice parameter and the concentration of Mg^{2+} ions in tetrahedral site of the samples as the functions of annealing temperature.

Conclusions

Atomic structure of the MgFe$_2$O$_4$ nanoparticles prepared by using combustion method has been investigated in detail via Rietveld refinement analysis of synchrotron X-ray diffraction data. The results indicated the formation of MgFe$_2$O$_4$ phase-pure with cubic structure in all the samples annealed at different temperature from 500 °C to 1000 °C. The crystallite size distributed in nano-scale from 11 nm to 41 nm. The concentration of Mg^{2+} ions in tetrahedral site was found to increase with increasing of annealing temperature and led to the change of the lattice parameter. The structural information and the cation distribution of the MgFe$_2$O$_4$ nanoparticles have allowed one to propose an explanation of their magnetic and electric properties.

Acknowledgements

References

[1] A. Goldman, Modern Ferrite Technology, *2 Ed., Springer, Pittsburg*, 2006.
[2] D. Vladikova *et al.*, Optimal prefiring conditions of substituted nickel ferrites for microwave applications, *Phys. status solidi*, 1990, 121(1), 249–255.
[3] H. Ji *et al.*, Microstructure and Temperature Dependence of Magnetic Properties of MnZnTiSn Ferrites for Power Applications, *IEEE Trans. Magn.*, 2010, 46(4), 974–978.
[4] M. A. Willard *et al.*, Magnetic Properties of Ordered and Disordered Spinel-Phase Ferrimagnets, *J. Am. Ceram. Soc.*, 1999, 82(12), 3342–3346.
[5] F. Li *et al.*, Site preference of Fe in nanoparticles of ZnFe$_2$O$_4$, *J. Magn. Magn. Mater.*, 2004, 268(3), 332–339.
[6] W. Tang *et al.*, Well-dispersed, ultrasmall, superparamagnetic magnesium ferrite nanocrystallites with controlled hydrophilicity/hydrophobicity and high saturation magnetization, *RSC Adv.*, 2013, 3(33), 13961.
[7] V. M. Khot *et al.*, Formation, microstructure and magnetic properties of nanocrystalline MgFe$_2$O$_4$, *Mater. Chem. Phys.*, 2012, 132(2-3), 782–787.
[8] V. Jeseentharani *et al.*, Synthesis of metal ferrite (MFe$_2$O$_4$, M = Co, Cu, Mg, Ni, Zn) nanoparticles as humidity sensor materials, *J. Exp. Nanosci.*, 2013, 8(3), 358–370.
[9] Z. Y. Kong *et al.*, The application of magnesium ferrite photocatalyst for photo treatment of methylene blue, *J. Eng. Sci. Technol.*, 2015, 10(4), 1-10.
[10] M. Gateshki *et al.*, Structure of nanocrystalline MgFe$_2$O$_4$ from X-ray diffraction, Rietveld and atomic pair distribution function analysis, *J. Appl. Crystallogr.*, 2005, 38(5), 772-779.
[11] B. D. *et al.*, Introduction to magnetic materials, *Mater. Today*, 2009, 12(3), 45.
[12] P. Holec, *et al.*, Preparation of MgFe$_2$O$_4$ nanoparticles by microemulsion method and their characterization, *J. Sol-Gel Sci. Technol.*, 2009, 51(3), 301-305
[13] V. Šepelák *et al.*, Nonequilibrium cation distribution, canted spin arrangement, and enhanced magnetization in nanosized MgFe$_2$O$_4$ prepared by a one-step mechanochemical route, *Chem. Mater.*, 2006, 18(13), 3057-3067.
[14] V. Šepelák *et al.*, Magnetization enhancement in nanosized MgFe$_2$O$_4$ prepared by mechanosynthesis, *J. Magn. Magn. Mater.*, 2007, 316(2), 4-5.
[15] S. Soontaranon *et al.*, Small Angle X-ray Scattering at Siam Photon Laboratory, *Chinese J. Phys.*, 2012, 50(2), 204-210.
[16] J. Rodríguez-Carvajal, Recent advances in magnetic structure determination by neutron powder diffraction, *Phys. B*, 1993, 192, 55-69.
[17] L. B. McCusker *et al.*, Rietveld refinement guidelines, *J. Appl. Crystallogr.*, 1999, 32(1), 36-50.
[18] N. K. Thanh *et al.*, Structural and Magnetic

Characterization of Copper Ferrites Prepared by Using Spray Co-Precipitation Method, *J. Nanosci. Nanotechnol.*, 2016, 16(8), 7949-7954.

[19] P. Hu *et al.*, Heat treatment effects on microstructure and magnetic properties of Mn–Zn ferrite powders, *J. Magn. Magn. Mater.*, 2010, 322(1), 173-177.

[20] S. M. Antao *et al.*, Cation ordering in magnesioferrite, $MgFe_2O_4$, to 982 °C using in situ synchrotron X-ray powder diffraction, *Am. Mineral.*, 2005, 90(1), 219-228.

[21] R. G. Kulkarni *et al.*, Comparison of Magnetic Properties of $MgFe_2O_4$ Prepared by Wet-Chemical and Ceramic Methods, *J. Solid State Chem.*, 1986, 64, 141-147.

[22] Y. Ichiyanagi, *et al.*, Magnetic properties of Mg-ferrite nanoparticles, *J. Magn. Magn. Mater.*, 2007, 310(2), 2378-2380.

[23] C. Liu *et al.*, Chemical control of superparamagnetic properties of magnesium and cobalt spinel ferrite nanoparticles through atomic level magnetic couplings, *J. Am. Chem. Soc.*, 2000, 122(26), 6263-6267.

[24] H. S. C. O'Neill *et al.*, The temperature dependence of the cation distribution in magnesioferrite ($MgFe_2O_4$) from powder XRD structural refinements and Mossbauer spectroscopy, *Am. Mineral.*, 1992, 77, 725-740.

[25] N. Marinoni *et al.*, In situ high-temperature X-ray and neutron powder diffraction study of cation partitioning in synthetic $Mg(Fe_{0.5}Al_{0.5})_2O_4$ spinel, *Phys. Chem. Miner.*, 2010, 38(1), 11-19.

[26] J. P. Singh *et al.*, Electronic structure studies of chemically synthesized $MgFe_2O_4$ nanoparticles, *J. Mol. Struct.*, 2016, 1108, 444-450.

Contact

*To Thanh Loan, tel: +84-4-8680787; totloan@itims.edu.vn

Toward enhancement of visible light photocatalytic activity of metal oxides throughnitrogen doping strategy

H. Sudrajat

Chulalongkorn University, 254 Pathumwan, Bangkok 10330, Thailand

Introduction

Photocatalysis with metal oxides, a clean, solar-driven process, is promising for environmental applications such as wastewater treatment. However, most metal oxides show poor visible light activity, although some of them are able to absorb visible light. Therefore, their practical applications are limited. For overcoming such limitation, a group of scientists from Thammasat University recently develops a series of nitrogen-doped metal oxides such as N-ZnO, N-ZrO$_2$, and N-WO$_3$ with visible light activity. Nitrogen doping is quite encouraging because of its comparable atomic size to that of oxygen, small ionization energy and stability. The catalysts are synthesized via simple routes based on the mechanochemically assisted thermal decomposition method. Their properties are characterized using various techniques including soft-XAS, which was performed at BL3.2Ua of Synchrotron Light Research Institute (Public Organization). Through XAS in complement to XPS, the incorporation of nitrogen into metal oxide lattice and the high photostability of nitrogen dopants are confirmed. Nitrogen doping occurs in both interstitial and substitutional sites. Moreover, N doping is found to significantly enhance the spectral response up to near-infrared (NIR) region. The N-doped catalysts show higher surface area and lower crystalline size compared to the pristine counter parts, and are stable upon irradiation. No signification reduction of the photocatalytic activity in repeated runs is observed. The light source and the catalyst determine the reactive species produced during the photocatalytic degradation. Less oxidative species such as superoxide radical and singlet oxygen play a critical role in the rhodamine 6G degradation by N-ZnO and N-ZrO$_2$ under visible light, while hydroxyl radicals are predominant under UV light. On the contrary, hydroxyl radicals and holes play a role in the degradation of amaranth by N-WO$_3$ under both visible and UV light. The photocatalytically treated solution of amaranth and that of methylene blue are nontoxic against *Bacillus cereus*, an important microorganism in agricultural soil.

Furthermore, to deal with the issue of difficult separation of catalyst particles and to improve their applicability in a real setting, two selected catalysts namely N-WO$_3$ and N-ZnO are immobilized on polyester fabric (PF), forming photoactive systems N-WO$_3$@PF and N-ZnO@PF, respectively. It is shown that the catalyst particles are evenly coated on the PF surface. Both N-WO$_3$@PF and N-ZnO@PF possess remarkable absorbance in the UV, visible, and NIR regions. The photoactive systems can be sucessfully used for the degradation of amaranth in a thin-film fixed-bed reactor (TFFBR) under solar, visible, and UV light. Unfortunately, after repeated runs, decreased photocatalytic activity is observed, likely due to decreased stability of the catalyst particles on the PF surface. On the basis of figures-of-merit recommended by IUPAC, N-WO$_3$@PF with a TFFBR shows a better performance compared to some existing solar photoactive systems, while N-ZnO@PF exhibits a comparable performance.
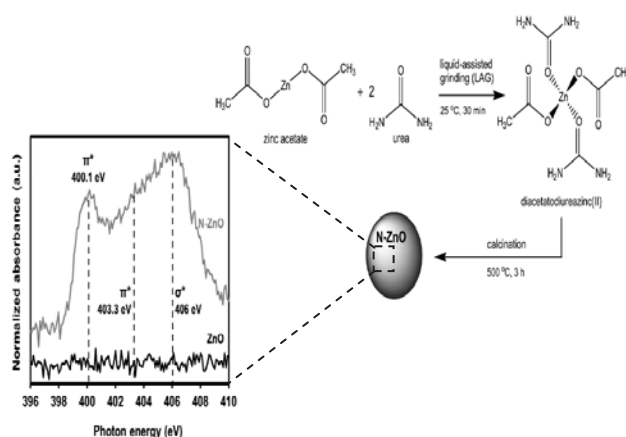

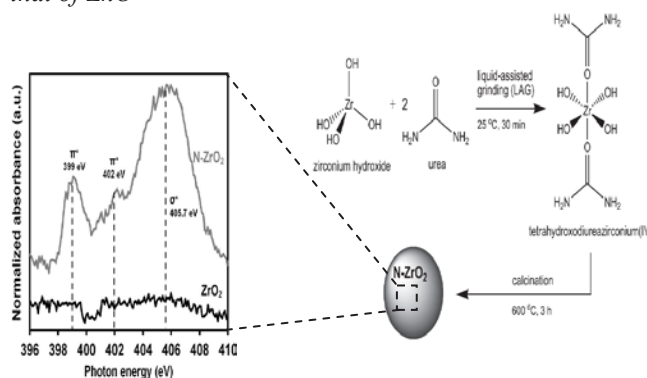*Figure 1: N K-edge XANES spectra of N-ZnO compared to that of ZnO*

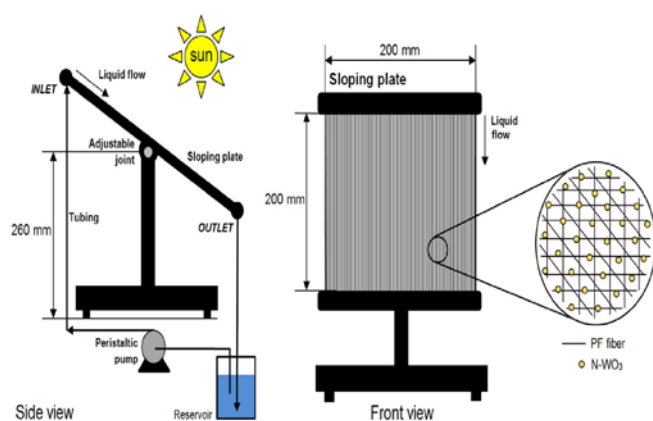*Figure 2: N K-edge XANES spectra of N-ZrO$_2$ compared to that of ZrO$_2$*

Figure 3: Experimental set-up for photocatalytic degradation of amaranth using N-WO₃@PF in a TFFBR with recirculation.

References

[1] H. Sudrajat *et al.*, *J. of Environmental Management.*, 2016, 165, 224-234.

[2] H. Sudrajat *et al.*, *J. of Water Process Engineering.*, In press. http://dx.doi.org/10.1016/j.jwpe.2016.11.006., 2016.

[3] H. Sudrajat *et al.*, *Environmental Chemistry Letters.*, 2016, 14, 243-249.

[4] H. Sudrajat *et al.*, *Environmental Science and Pollution Research.*, 2016, 23, 10177-10188.

[5] H. Sudrajat *et al.*, *Bulletin of Materials Science.*, Submitted.

[6] H. Sudrajat *et al.*, *Solar Energy Materials and Solar Cells.*, 2016, 149, 294-303.

[7] H. Sudrajat *et al.*, *Materials Research Bulletin.*, 2016, 83, 369-378.

Contact

*H. Sudrajat; hanggara.s@chula.ac.th

Research highlight of beamline 8 2016:
Synchrotron XAS of vanadium in HSLA steel

P. Suwanpinij*

The Sirindhorn International Thai-German, Graduate School of Engineering (TGGS),
King Mongkut's University of Technology North Bangkok (KMUTNB), 1518 Pracharat 1 Road, wongsawang, Bangsue,
Bangkok 10800, Thailand

Abstract

This study demonstrates how the synchrotron X-ray absorption spectroscopy can be applied for the quantification of precipitation in high strength low alloyed steel. The fraction of vanadium in different forms of compounds, as well as in the solid solution was measured using a linear combination fit of the spectral weights.

Introductions

High strength low alloyed (HSLA) steels are well-known to inherit their high strength from precipitation hardening and grain refinement mechanisms. Both are the results of the precipitation of their microalloying elements. Optimization of the precipitation along a processing route is therefore important to obtain the best steel quality out of the costly microalloying elements. This work selects a vanadium containing HSLA steel for the analysis of the precipitation under different cooling rates after the hot rolling process by synchrotron X-ray absorption spectroscopy (XAS). According to the reported solubility data, vanadium precipitates as V(C, N), VN and VC at relatively low temperature compared with other microalloying elements, and hence is significantly influenced by different cooling rates in ferrite temperature region.

Experimental XAS

The experiment was setup to measure the vanadium precipitates in the samples with different cooling rates. Two samples processed with identical thermomechanical parameters were closely mounted together with epoxy resin in order to cover the whole sample with the whole X-ray beam with a cross section of 1 mm × 16 mm. The XAS experimental setup in both fluorescent and transmission mode. The detector used in the fluorescent mode was a highly sensitive 13-elements germanium detector with an energy resolution ($\Delta E/E$) of 3×10^{-4}. The surface of the sample was set at an angle of 45° to both the incoming beam and the detector. On the other hand, the detector in the transmission mode was a 40 cm long chamber containing a mixture of argon and helium gas with a pressure of 104 mbar. A solution-annealed sample, employed as a standard for vanadium solute atoms in the solid solution, and the steel samples with three different cooling rates, i. e., 60, 5 and 0.1 K × s-1, were selected to measure vanadium K-edge absorption spectra in a fluorescent mode. According to the vanadium K-shell electron binding energy, E0, of 5465 eV, the X-ray photon energy was selected and scanned by a Ge (220) double crystal monochromator (with a 2d-spacing of 4.001 Å from 5445 eV to 5870 eV with an energy step of 0.2 – 0.3 eV. It took around 50 minutes to complete a scan

XAS Results

The spectra of the absorption coefficient μ as a function of energy in EXAFS mode were recorded from XAS. The results of the samples with the cooling rates of 60, 5, 0.1 K × s-1 are shown in normalized form in Fig. 1. In a similar manner, the spectra measured from the high purity compounds of all possible kinds to form with vanadium in the steel as well as the solution-annealed steel sample were shown in Fig. 2. The latter had vanadium as solute atom in the solid solution and included V-Fe bonds. The absorption edge was in the range of 5467-5484 eV, compared with the theoretical E0 value of the K-edge energy of vanadium of 5465 eV. This corresponds to the absorption of the vanadium central atoms.
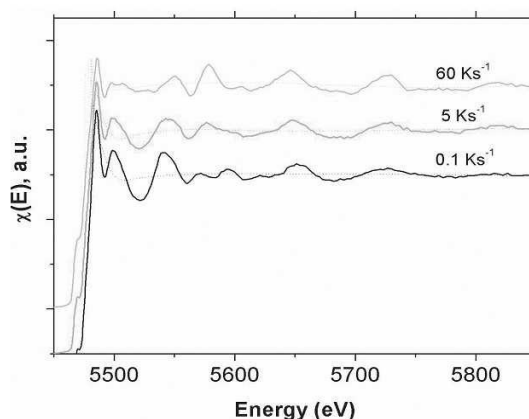

Figure 1: The normalized spectra of the measured samples with the cooling rates of 60 K × s-1, 5 K × s-1 and 0.1 K × s-1, shifted from another on arbitrary y-axis
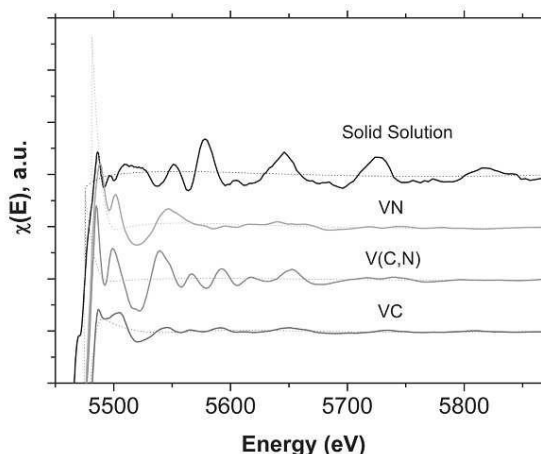

Figure 2: The normalized spectra of the standard samples, i. e., solution annealed sample (V in solid solution), VN, V(C, N), VC, shifted from one another on arbitrary y-axis

Conclusions

XAS could quantify vanadium in different forms in HSLA steel influenced by different thermomechanical processing parameters, although its nominal concentration was as dilute as 0.1 wt.-%. The main intention of this study was to demonstrate how XAS could be a very powerful and effective material characterization tool for the quantitative investigation of precipitation in bulk metal samples even at dilute concentration without any extra sample preparation. This was a significant advanced progress in material characterization and metallurgy.

Acknowledgements

Author would like to express thanks to Dr. Wantana Klysubun, Dr. Nirawat Thammajak, and BL8 staff at the Synchrotron Light Research Institute (Public Oraganization), for XAS measurement.

Reference

[1] P. Suwanpinij *et al*., Quantification of vanadium precipitates in HSLA steel by synchrotron X-ray absorption spectroscopy (XAS), *Materials Testing, München*, 2016, 58(1), 5-11.

Contact

*P. Suwanpinij ; piyada.s@tggs.kmutnb.ac.th

76   SLRI Annual Review 2016 - 2017

The study of titanium dioxide phase transformation using time-resolved X-ray absorption spectroscopy and linear combination analysis

Y. Poo-arporn*[1] and R. Palangsuntikul[2]

[1]Synchrotron Light Research Institute (Public Organization), 111 University Avenue, Muang District, Nakhon Ratchasima 30000, Thailand
[2]Biological Engineering Program, Faculty of Engineering, King Mongkut's University of Technology Thonburi,126 Pracha Uthit Rd., Bang Mod, Thung Khru, Bangkok 10140, Thailand

Abstract

The *in-situ* X-ray absorption near edge structure (XANES) measurement and linear combination fitting were applied to monitor phase transformation of titanium dioxide. In this study, TiO_2 (TiSG) was prepared by a sol-gel method using titanium isopropoxide as a precursor. At low preparation temperature, the results revealed the formation of an amorphous structure. To obtain the anatase phase, the calcination at 843 K was necessary. Using phase fraction plot, TiO_2 phase-transition can be observed at temperatures between 748 and 778 K and remain unchanged at 873 K.

Introduction

Several studies on the application of photocatalysis using TiO_2 have been reported. Many applications have used TiO_2 in both amorphous and crystalline forms as the photocatalyst such as environmental decontamination, solar cell, paint pigment, and cosmetic. For TiO_2 photocatalyst, the amorphous phase exhibits high surface area whereas crystalline anatase form prolongs the recombination reaction. It has been reported that the mixture of amorphous and crystalline TiO_2 also showed photocatalytic properties. Hence, the precise control of phase fraction between amorphous and anatase TiO_2 would be beneficial to optimize its photocatalytic activity. In this study, the TiO_2 was prepared by the sol-gel method using titanium (IV) isopropoxide (TTIP) as an alkoxide precursor. *In-situ* X-ray absorption near edge structure (XANES) measurements were performed to monitor a phase transition of the prepared sample caused by the calcination.

Experimental

TiO_2 (TiSG) was prepared by the sol-gel method. TTIP was added to the mixture of 2-propanol and ethylene glycol under magnetic stirring in a glove box. The gel was dried at 383 K (D-TiSG) before the *in-situ* XANES measurement. To produce crystalline TiO_2, the D-TiSG was calcined in air at 873 K for 1 hour.

XANES measurements were performed at the time-resolved XAS (Bonn-SUT-SLRI) beamline of Synchrotron Light Research Institute (SLRI), Thailand. The beamline employs an energy dispersive monochromator equipped with Si(111) single crystal and the position sensitive detector (PSD) to obtain the XANES spectra.

Results and discussion

Growing of the anatase in D-TiSG as a function of temperature was monitored using linear combination fitting (LCF) in the Athena software. LCF was performed with the combinations of two model spectra in the energy range between 4963-5063 eV. The Ti K-edge XANES spectra of D-TiSG calcined at 713 K and 873 K were used as predictors of amorphous TiO_2 and anatase TiO_2, respectively. During the LCF, the threshold energy, E_0, was fixed. Fig. 1 showed the normalized Ti K-edge XANES spectra of the D-TiSG at temperature between 718 K and 868 K. The calculated results showed well fittings at all temperatures.

The relative ratio between amorphous and anatase phases was shown in Fig. 2. At 718-738 K, the anatase was gradually developed with the phase fraction around 0.1. The highest slope was observed at temperature between 748 and 778 K suggesting the transition temperature of the amorphous TiO_2. The crystallization process of D-TiSG to anatase was completed at 843 K. For the formation of rutile, the typical temperature required for anatase to rutile phase transformation is 873 K [1].
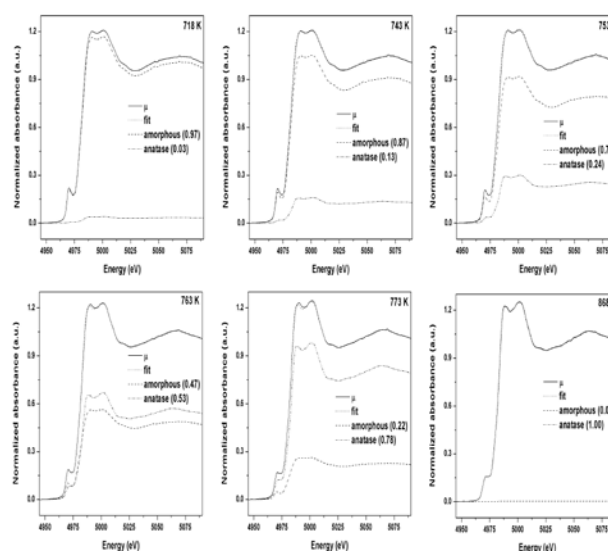

Figure 1: The fitting results of Ti K-edge XANES of D-TiSG at temperature between 718 and 868 K.
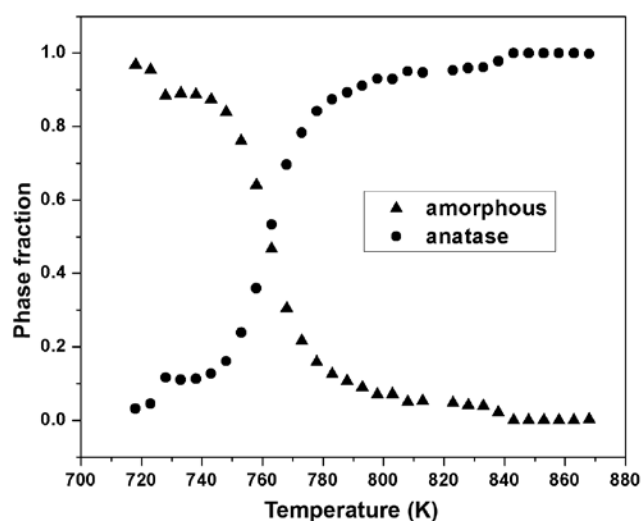
Figure 2: Phase fraction of amorphous and anatase at the selected temperature 718-868 K.

The conversion temperature and the rate of transformation depend on how fast the primary particles in the anatase phase sinter together to reach the critical size. It is expected that the critical nucleus size of rutile crystallites is at least three times larger than that of anatase [2]. This means that if sintering of anatase particles is retarded by a suitable technique the probability of reaching the critical nucleus size is lowered, delaying the transformation, and stabilizing anatase up to 1273 K [3]. Once the critical particle size is achieved using nanosized anatase as starting material, the transformation reaches a measurable speed at lower temperatures [4]. By applying pressure, both surface free energy and surface stress may be tuned with sufficient accuracy. An increase of pressure from 1 to 23 kbar lowered the transformation temperature with 773 K opening the way for pressure-assisted low temperature synthesis [5]. Further investigations on the anatase to rutile phase transition would provide valuable information for the preparation of mixed phase TiO_2.

Conclusion

TiO$_2$ phase transformation was successfully monitored by *in-situ* XANES measurement. At low temperature, the amorphous phase could be synthesized. For crystalline phase, high temperature treatment was necessary. The amorphous structure of TiO_2 could be transformed to anatase by calcinations at 843 K and remained stable at 873 K. LCF was successfully applied to monitor the transition mechanism. It was clearly observed that the transition of amorphous to anatase could be performed at 748-778 K. There was no indication of rutile structure by calcination at 823 K.

References

[1] J.T. Bastow *et al.*, *State. Chem. Mater.*, 1999, 11, 3518.
[2] K.-N.P. Kuma, *ApplCatal. A.*, 1994, 119, 163.
[3] G. Colón *et al., Appl. Catal. A: Gen.*, 2002, 231, 185.
[4] R.D. Shannon *et al., J. Am. Ceram. Soc.*, 1965, 48, 391.
[5] M. Stir *et al., Nucl. Instrum.Meth.Phys. Res. B.*, 2003, 199, 59.

Contact

*Y. Poo-arporn, tel: +66-44-217040 ext 1478; yingyot@slri.or.th

Identification of freshwater-cultured pearls (*Chamberlainia hainesiana*) by XAS technique

S. Satitkune*, N. Monarumit, and N, Noirawee

Department of Earth Sciences, Faculty of Science, Kasetsart University, 50 Ngam Wong Wan Rd, Ladyaow Chatuchak, Bangkok, 10900, Thailand

Abstract

The freshwater-cultured pearl (*Chamberlainia hainesiana*) is an organic gemstone mainly composed of calcium carbonate mineral including calcite, aragonite and vaterite phases. The season to collect the pearl samples is believable affected to the quality of luster. The aim of the research is to identify the quality of freshwater-cultured pearls from different seasons and different lusters. These data could be proved by the X-ray absorption spectroscopy (XAS) focused on X-ray absorption near edge structure (XANES). As the results, the samples in both winter and rainy seasons similarly showed the Ca K-edge XANES spectra. This research concluded that the collecting season did not affect the quality of freshwater-cultured pearls. However, the quality of pearls had been related with their lusters. According to Ca K-edge XANES spectra, high luster pearls consisted only of the aragonite phase. Low luster pearls composed of the mixture between aragonite and vaterite phases.Inaddition, the XAS technique was proved to bea non-destructive method to be apply for gemological research.

Introduction

The freshwater-cultured pearl (*Chamberlainia Hainesiana*) is an organic gemstone mainly composed of calcium carbonate minerals including calcite, aragonite and vaterite phases. However, the major composition is aragonite formation. The crystal structure of aragonite mineral forming is an orthorhombic system [1]. According to the quality of freshwater, the collecting period of freshwater-cultured pearl is the winter season. The aim of this research is to analyze the quality of freshwater-cultured pearl samples from the winter and rainy seasons with the different lusters. The X-ray absorption spectroscopy (XAS) is a powerful technique to study the local atomic environment of interested atoms. XAS technique is suitable to apply in gemstone research [2]. In this study, we focused on the atomic environment of Ca atoms in freshwater-cultured pearl samples collected in different seasons. The Ca K-edge XAS spectra of the samples will be compared with those of $CaCO_3$ minerals based on another research [3].

Experiments

Materials

The freshwater-cultured pearl samples were collected from Kanchanaburi Inland Fisheries Development Center in winter and rainy seasons as shown in Fig. 1. The gemological properties of the samples were measured by basic gem instrument obtained at Department of Earth Sciences, Kasetsart University.
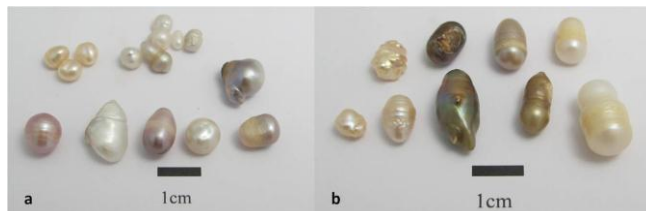

Figure 1: Freshwater-cultured pearls collected in winter (a) and rainy seasons (b).

Methods

XAS technique focused on XANES of the samples was experimented on Ca K-edge. The XANES spectra were carried out at the beamline 8, Synchrotron Light Research Institute (Public Organization) by using the Ge(220) double crystal monochromator and 13-channel array Ge detector in fluorescence mode. The photon energy was calibrated at 4038.5 eV and scanning range of 4018.5 eV to 4033.5 eV with five scans per sample to obtain the precise spectrum. The specific procedures of the XAS fundamental were referred to that research [4].

Results and discussion

Pearl samples with different seasons

The Ca K-edge XANES spectra of freshwater-cultured pearl samples were evaluated by Athena software [5] as shown in Fig. 2. The XANES spectra consisted of a pre-edge region (a), rising edge (b), white-line position (c), and post-edge region (d, e). The samples from winter and rainy seasons similarly showed the XANES patterns referred to the mixture component among aragonite and vaterite phases considering the photon energy position in Table 1. It could be indicated that the quality of the freshwater-cultured pearls does not relate to the collecting seasons.

Table 1: The photon energy (eV) of freshwater-cultured pearls compared with $CaCO_3$ standard.

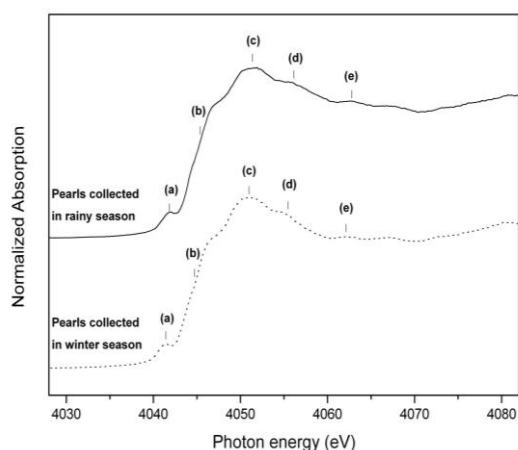| Sample	Photon Energy (eV)				
	a	b	c	d	e
Pearls from winter season	4041	4045	4050 (broad)	4054	4061
Pearls from rainy season	4041	4045	4050 (broad)	4054	4061
Aragonite	4040	4045	4050 (one peak)	4054	4061
Vaterite	4040	4045	4050 (broad)	None	None

Figure 2: Ca K-edge XANES spectra of freshwater-cultured pearl samples collected in different seasons.

Pearl samples with different lusters

However, the quality of freshwater-cultured pearl samples was due to their luster including high-, moderate- and low-luster (or lusterless). For our other works, the Ca K-edge XANES spectra of various luster pearls showed the different pattern as shown in Fig. 3 based on their composition [6] High luster pearls consisted only of the aragonite phase. On the other hand, low luster pearls composed of aragonite mixing vaterite phases. The photon energy positions were summarized in Table 2.

Table 2: The photon energy (eV) of different lusters freshwater-cultured pearls compared with $CaCO_3$ standard.

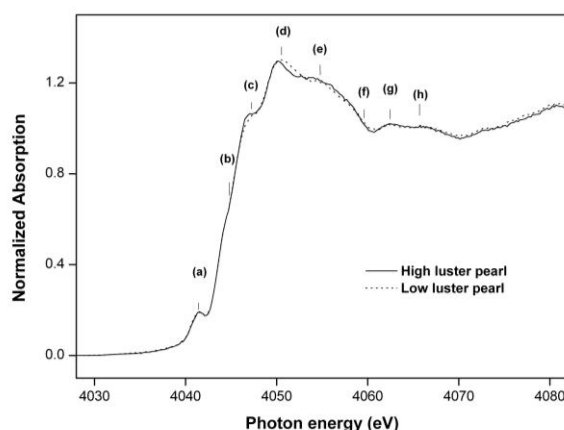| Sample	Photon Energy (eV)							
	a	b	c	d	e	f	g	h
High luster pearls	4041	4045	4047	4050 (one peak)	4054	None	4061	4065
Low luster pearls	4041	4045	4047	4050 (broad)	4054	4058	4061	4065
Aragonite	4040	4045	4047	4050 (one peak)	4054	None	4061	4065
Vaterite	4040	4045	4047	4050 (split)	None	4058	None	None

Figure 3: Ca K-edge XANES spectra of freshwater-cultured pearl samples with different lusters.

Conclusion

This research could be concluded that the collecting season did not affect the quality of freshwater-cultured pearls considered by Ca K-edge XANES spectra. These spectra indicated that the aragonite and vaterite phases were detected in freshwater-cultured pearl structure based on their lusters. The XAS technique is suitably applied for gemology because of a non-destructive method.

Acknowledgements

References

[1] J.P.R. De Villiers, Crystal structures of aragonite, strontianite, and witherite , *Am. Mineral.*, 1971, 56, 758-767.

[2] P. Wathanakul *et al.*, XAS study on Cr^{3+} local environment in ruby samples, in *19th annual V. M. Goldschmidt conference*, Davos, Switzerland, June 21-26, 2009, A1421.

[3] L. Brinza *et al.*, Combining μXANES and μXRD mapping to analyse the heterogeneity in calcium carbonate granules excreted by the earthworm *Lumbricus terrestris*, *J. Synchrotron. Radiat.*, 2014, 21, 235-241.

[4] W. Klysubun *et al.*, Performance and status of beamline BL8 at SLRI for X-ray absorption spectroscopy, *J. Synchrotron. Radiat.*, 2012, 19, 930-936.

[5] B. Ravel *et al.*, *ATHENA, ARTEMIS, HEPHAESTUS*: data analysis for X-ray absorption spectroscopy using IFEFFIT, *J. Synchrotron. Radiat.*, 2005, 537-541.

[6] N. Monarumit *et al.*, Identification of high-luster and lusterless freshwater-cultured pearls by X-ray absorption spectroscopy, *J. Appl. Spectrosc.*, 2015, 82, 677-680.

Contact

*S. Satitkune, tel: +66-2940-6966; fscisrd@ku.ac.th

SLRI user program and statistics

P. Janphuang*, S. Tonghom, A. Saesong, S. Rodthai, W. Chanthawat and Ch. Neti
Synchrotron Light Research Institute (Public Organization), 111 University Avenue, Muang District, Nakhon Ratchasima 30000, Thailand

Abstract

SLRI calls for the public use beam time proposals twice a year. The submitted proposals for experiment are reviewed by the SLRI proposal review committees (PRC) for the benefits and applications of proposed research before allocating beam time. Since 2003, a variety of proposals have been accepted by SLRI for the promotion of academic research as well as industrial applications. Limit number of grants to cover travel and living expenses of individuals and small groups using beam time at SLRI are offered to in the country and ASEAN users. In addition, workshops and trainings on a special topic are annually arranged for the users and to the public who are interested in to improve their experimental and analytical skill securing high quality data and publishable results.

SLRI user program

Synchrotron Light Research Institute (SLRI) is a national user facility providing synchrotron radiation to researchers in many fields of science and technology, including material science, chemistry, biology and medicine, environmental science, physics, and engineering. The institute welcomes researchers from academia, government laboratories, industry and research facilities within Thailand and aboard. SLRI operation is typically divided into two cycles per year, starting from January to May (1st cycle) and September to December (2nd cycle). Access to SLRI is approved through the beam time proposals that are technically reviewed by SLRI PRC. All beam time is requested each cycle through the web based, *beamapp.slri.or.th*. In the system, scientific experiments to be conducted at SLRI must be described in a beam time proposal with details about the amount of beam time desired on a specific beamline, instrumentation, safety hazard, preferred date of experiment. After submitted proposals have been reviewed and rated, the beamline managers of each beamline are responsible for scheduling the beam time. Once it is completed, the user office with direct all users of the outcome of their proposals. For further information, SLRI are now providing the financial support (local transportation and accommodation) for in the country and ASEAN users during experiment at SLRI. Anyone who is interested in applying for the grants can register during online proposal submission process. Due to the limit number of grants, the beam time with grants proposals must be reviewed by SLRI PRC and the beamline manager for the scientific merit and to ensure the research quality contributing to scientific advancement.

Typically, two types of proposals can be submitted to conduct experiment at SLRI; non-proprietary and proprietary proposals. The prior should be submitted by principal investigator (PI) or project leader through the beam time applications described previously. The latter need to be submitted via the Business Development Division throughout the year at *www.slri.or.th/bds/*. In such case, additional beam time fee and/or service can be charged. Thus, users are recommended to contact beamline manager or user office for technical advice.

For all current and prospective users, the user office is the first point of contact at SLRI to facilitates and support the user with the beam time application process, user agreements, logistical and accommodation arrangement, and more. Once the users arrive at SLRI, check-in at the user office along with register to the safety training at safety section in order to receive SLRI access card and dosimeter. The summary of SLRI beam time application procedure is illustrated in Fig. 1.
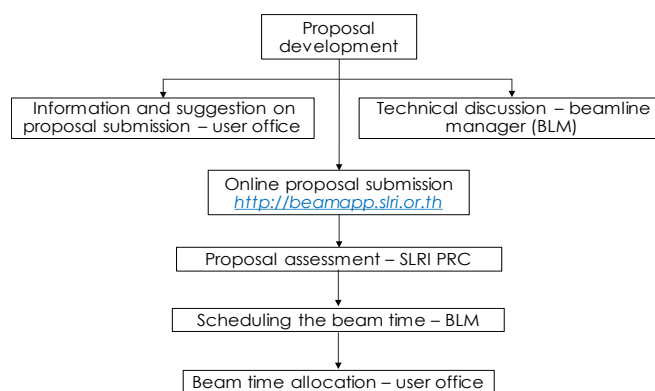

Figure 1: An overview of the beam time application procedure at SLRI.

User statistics & outcomes

The number of user visits separated by fiscal year starting from 2003 to 2017 is shown in Fig. 2.
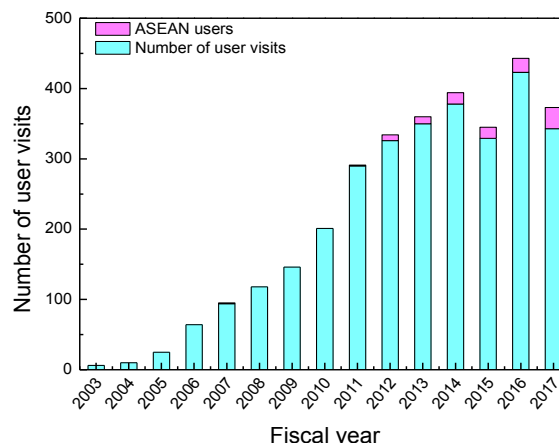

Figure 2: Number of user visits separated by fiscal year.

As of August 2017, the total number of user visits, since the first beamline was opened to public in 2003, was 3103.

Due to an increasing number of the beamline opened to the public from 1 beamline in 2003 to 10 beamlines in 2017, it is obvious that the number of users gradually increases every year. Experiments and facilities at SLRI were also opened for the researchers from ASEAN. The total number of ASEAN users was 102 accumulated from 2010 to 2017.
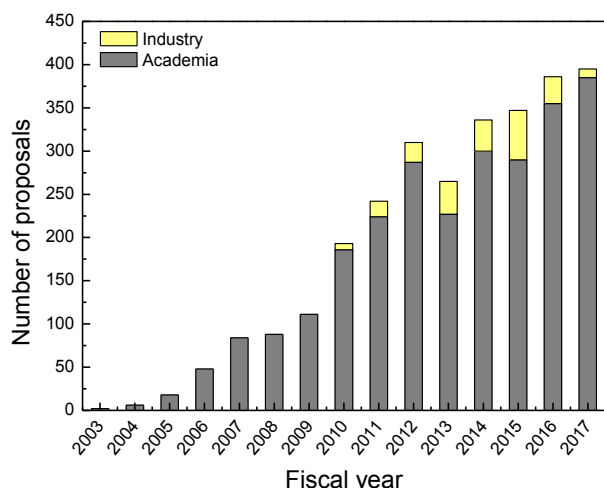

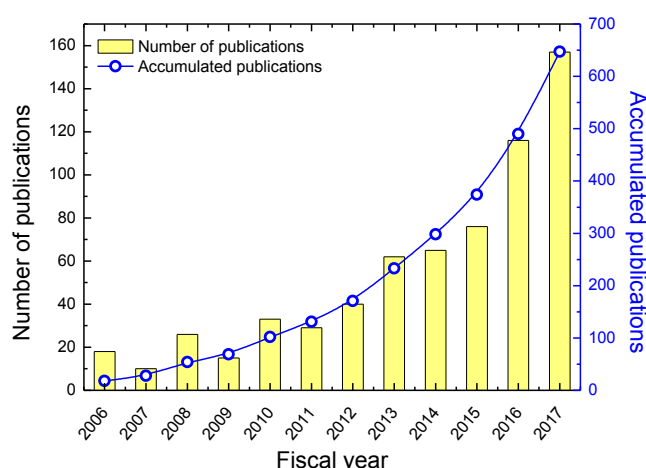*Figure 3: Number of user visits separated by fiscal year.*

Figure 4: Number of peer-reviewed journal articles.

The number of accepted proposals from 2003 to 2017 is given in Fig. 3. It is clear that the number of proposals increase every year. There was totally 2831 accepted proposals collected from 2003. Most of the proposals are proprietary use from academia and governmental laboratories. However, the proposal from industries tend to be increased annually since 2010. This demonstrates the potential of developing country infrastructure using synchrotron radiation.

One of the principle measurable output parameters of SLRI is the number and quality of publications accepted in peer-reviewed journals. The number of publications raised continuously from 2006, eventually reaching 157 publications per year in 2017 as illustrated in Fig. 4. Since SLRI has begun operation back in 2003, a total of 647

publications have been accepted in peer-reviewed journals. These are promising figures indicating both the quality of facilities (beamlines and experimental stations) and scientific advancement at SLRI.

ASEAN synchrotron schools

SLRI has annually hosted several workshops and training courses for the users to strengthen their experimental and analytical skills and learning how to secure high quality data and get publishable results. ASEAN workshops organized by SLRI are detailed as follows;

The ASEAN workshop on photoemission electron spectroscopy and microscopy (AWPESM) – every 2 years

The aim of this workshop is to promote the uses of techniques available at Photoemission Spectroscopy (PES) and PEEM end-stations to scientists, university lecturers and graduated students in Thailand and ASEAN countries. Details of the workshop will be designed to cover in both sessions of lectures and practical exercises for experiments using techniques. Participants will gain basic knowledge on the analytical techniques available at the end stations and will be able to include these techniques into their on-going research works. Ultimately, this will promote the uses of both beamlines and end-stations to its full capacity.

ASEAN Workshop on X-ray fluorescence: quantitative analysis of plants (AWXRF) – every 2 years

This workshop aims to promote the uses of X-ray fluorescence technique available at the end stations of beamline 6b: Micro-X-ray fluorescence (μ-XRF). Details of the workshop will cover in both sessions of lectures and practical exercises including experiments and data analysis. Participants will gain knowledge on the principle of X-ray fluorescence corresponding quantitative analysis of plant materials. In addition, there will be a group discussion among the participants, invited speakers and SLRI beamline scientists opened for raising problems relating to their on-going research works and finding the solutions to complete their works.

ASEAN workshop on small angle X-ray scattering (AWSAXS) – every 2 years

Small Angle X-ray Scattering (SAXS) is dedicated for nano-scale structural investigation of material such as polymer, fiber and colloid. The goal of the AWSAXS workshop is to provide basic and essential knowledge to well understand SAXS techniques and able to fully apply this technique in research problems.

ASEAN workshop on XANES simulation and in-situ XAS experiment (AWXIXE) – every 2 years

X-ray absorption spectroscopy (XAS) is a technique widely used for determining oxidation states, coordination geometry, and local atomic structure of materials.

Synchrotron Light Research Institute (SLRI) provides intense and energy tunable X-ray beam for XAS experiments and welcomes scientists from around the world; providing them beamtime and technical assistance in both experimental and analytical aspects. The workshop aims to focus on the in-situ XAS experiment and theoretical calculation using FEFF program.

ASEAN workshop on X-ray absorption spectroscopy (AWX) – every 2 years

X-ray absorption spectroscopy (XAS) has become a powerful technique for structural determination of materials, being employed in various research areas (for example chemistry, catalysis, material science, biology, environmental science, geology, and archeology). The aim of the AWX workshop is to provide basic and essential knowledge to well understand XAS techniques. Furthermore, AWX will bring together national and international experienced synchrotron users with different scientific backgrounds, particularly new users from the neighboring countries of Thailand to promote XAS research in ASEAN scientific community.

The ASEAN synchrotron science camp - annually

The ASEAN Synchrotron Science Camp aims to provide students with hands-on science learning and a fun introductory to the world of synchrotrons. The Camp helps promote cooperating and networking among ASEAN countries. Participants will gain knowledge and clear understanding on accelerator, production and application of synchrotron radiation. In addition, Participants will have chance to visiting beamlines and experimental stations to discuss their research topics of interest with our scientists for future collaborations; some beam time could be arranged accordingly.

All these aspects remain key to continuing success of SLRI.

References
[1] Beam time application system www.slri.or.th, beamapp.slri.or.th

Contact
User Office Division, tel: +66-44-217040 ext. 1602-1605; useroffice@slri.or.th

Editorial Board :

Somchai Tancharakorn
Pattanaphong Janphuang
Chatree Saiyasombat
Nuttawan Pramanpol
Chonthicha Kaewhan
Surangrat Tonlublao
Sidaphat Rodthai

Design & Layout :

Tewarit Panpian

Synchrotron Light Research Institute (Public Organization)
Sirindhornwitchothai Building
111 University Avenue, Muang, Nakhon Ratchasima, 30000
Post Address: PO. Box 93 Nakhon Ratchasima 30000 THAILAND
Phone: +66-44-217-040 ext. 1602-1603
Fax: +66-44-217-047
E-mail: useroffice@slri.or.th